Review

Recent Advancements in Chalcogenides for Electrochemical Energy Storage Applications

Kwadwo Mensah-Darkwa [1,*] ⓘ**, Daniel Nframah Ampong** [1] ⓘ**, Emmanuel Agyekum** [2] ⓘ**, Felipe M. de Souza** [3] **and Ram K. Gupta** [3,4,*]

1 Department of Materials Engineering, College of Engineering, Kwame Nkrumah University of Science and Technology, Kumasi AK-448-6434, Ghana; ndampong2015@gmail.com
2 Department of Material Science and Engineering, College of Mechanics and Materials, Hohai University, Nanjing 210098, China; kwagyek@gmail.com
3 Kansas Polymer Research Center, Pittsburg State University, Pittsburg, KS 66762, USA; fdesouza@pittstate.edu
4 Department of Chemistry, Pittsburg State University, Pittsburg, KS 66762, USA
* Correspondence: kmensahd@aggies.ncat.edu (K.M.-D.); rgupta@pittstate.edu (R.K.G.)

Abstract: Energy storage has become increasingly important as a study area in recent decades. A growing number of academics are focusing their attention on developing and researching innovative materials for use in energy storage systems to promote sustainable development goals. This is due to the finite supply of traditional energy sources, such as oil, coal, and natural gas, and escalating regional tensions. Because of these issues, sustainable renewable energy sources have been touted as an alternative to nonrenewable fuels. Deployment of renewable energy sources requires efficient and reliable energy storage devices due to their intermittent nature. High-performance electrochemical energy storage technologies with high power and energy densities are heralded to be the next-generation storage devices. Transition metal chalcogenides (TMCs) have sparked interest among electrode materials because of their intriguing electrochemical properties. Researchers have revealed a variety of modifications to improve their electrochemical performance in energy storage. However, a stronger link between the type of change and the resulting electrochemical performance is still desired. This review examines the synthesis of chalcogenides for electrochemical energy storage devices, their limitations, and the importance of the modification method, followed by a detailed discussion of several modification procedures and how they have helped to improve their electrochemical performance. We also discussed chalcogenides and their composites in batteries and supercapacitors applications. Furthermore, this review discusses the subject's current challenges as well as potential future opportunities.

Keywords: chalcogenides; electrochemical; energy storage; batteries; supercapacitors

1. Introduction

Energy storage has become an increasingly important research field. More and more researchers are focusing their attention on creating and researching novel materials for use in energy storage systems due to the promotion of sustainable development goals since traditional energy sources such as oil, coal, and natural gas have finite supplies. The extraction and processing of these conventional nonrenewable energy sources have disastrous consequences for the environment. It is well established that coal gasification contributes significantly to global warming through CO_2 emissions into the atmosphere. Furthermore, these conventional nonrenewable energy sources are further constrained by the depletion of reservoirs, geopolitical conflicts, and volatile oil prices. Provided the challenges mentioned above, sustainable renewable energy sources have been hailed as a model for reducing our dependency on nonrenewable energy sources. However, renewable energy generation is intermittent; hence, the deployment of renewable energy sources necessitates the use of efficient and reliable energy storage devices. We can reduce our

dependency on oil and coal while also reducing environmental degradation by deploying clean and renewable energy technologies.

　　Material science and engineering have the potential to revolutionize energy supply and storage through the development of novel materials. Modern energy storage systems require the creation of new materials with improved power and energy storage capabilities and higher efficiency and safety levels. One of the most significant advances in material science and engineering has been the application of electrochemical energy storage devices to store energy electrochemically [1,2]. Electrochemical energy storage (EES) technologies include capacitors, supercapacitors, batteries, and fuel cells; these have found widespread utilization in hybrid/all-electric vehicles, modern portable electronic gadgets, and commercial/residential applications. Each of these electrochemical storage technologies has its unique charge storage mechanism. Figure 1 depicts a typical device configuration of the (a) fuel cell, (b) battery, and (c) supercapacitor, showing the anodes, cathode, electrolyte, and separator, which form the main parts.
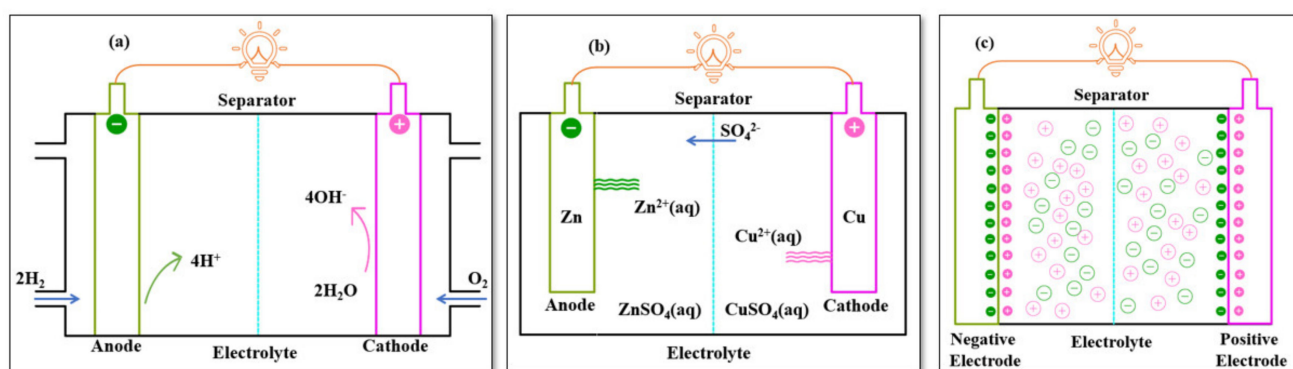

Figure 1. A typical device configuration of (**a**) fuel cell, (**b**) battery, and (**c**) supercapacitor.

　　The Ragone plot (Figure 2) compares the various electrochemical storage devices in terms of specific power density and specific energy. Capacitors stores electrical energy in an electric field; they exhibit higher specific power at lower specific energy. Supercapacitors are electrochemical storage devices that store energy at the electrolyte–electrolyte interface. Energy storage mechanisms involve electrochemical double-layer activity and/or redox activity on the electrode surface. They exhibit higher specific energy compared to capacitors with overlapping performance for the specific power. Battery stores energy via electrochemical reactions, exhibiting high energy density but suffers from low power densities. A fuel cell is an electrochemical device that harvests electricity directly from chemical energy, using hydrogen and oxygen as fuel. When compared to other electrochemical energy storage systems, they have the highest energy densities. For electrochemical storage systems to be effective, the electrode material and electrolyte medium must have exceptional ionic and electronic transport characteristics. Metal chalcogenides are widely used as electrode material in electrochemical energy storage applications such as lithium-ion batteries, sodium-ion batteries, and supercapacitors. This is due to its extraordinary features, which include high reversible capacity, a significant number of electroactive sites, thermal stability, and a stable structure enabling cyclability [3–6]. Furthermore, the deeper faradic reaction of chalcogenides allows for greater capacity; it is inexpensive and can even be considered a green material.
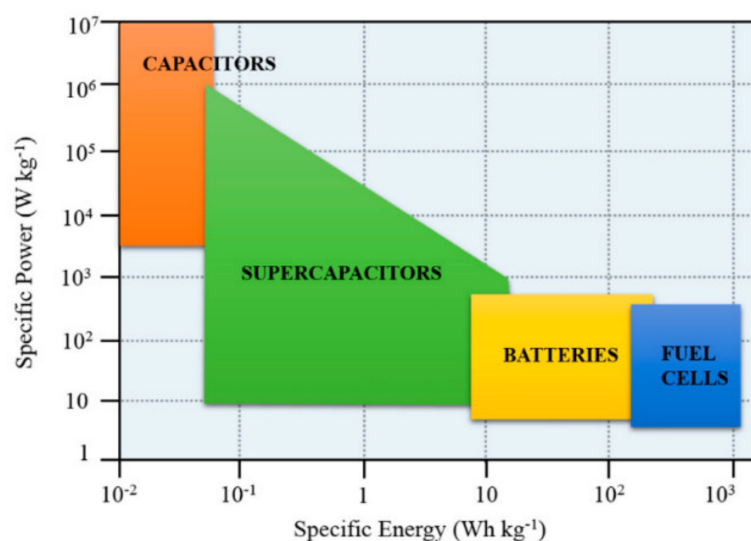
Figure 2. Ragone plots for different types of electrochemical energy storage devices. Adapted from [7]. Copyright (2019) MDPI. This article is an open access article distributed under the terms and conditions of the Creative Commons Attribution (CC BY) license.

The term chalcogenides refer to materials that contain one or more chalcogen elements, such as sulfides, selenides, or tellurides. Chalcogenides are binary compounds containing at least one chalcogen anion and another electropositive element; dichalcogenides contain two chalcogens. The unique properties of transition metal chalcogenides have been explored in all areas of material sciences and engineering. Transition metal chalcogenides (MX or MX2) have been attracting an increasing amount of research attention as electrode materials for electrochemical energy storage devices because of their high power density and stability, especially for supercapacitors. M denotes transition metals such as Ni, Co, Mn, Cu, Zn, Mo, or W, while X denotes chalcogens (such as S, Se, and Te). Metal sulfides, metal selenides, and metal tellurides, for example, have proven remarkable high-power density and cyclic stability and, as a result, have been used in supercapacitor applications. The crystalline structure, morphology, synthesis approach, and chemical composition all influence the electrochemical performance of the electrode of an electrochemical energy storage system. Layer and spinel structures are the most reported crystal structures in electrochemical energy storage applications.

Several published works have suggested advances in the use of metal chalcogenides as a viable material for enhanced electrochemical storage systems in terms of energy storage mechanisms, structure optimization, and stabilization. Others have argued that to better understand and facilitate the creation of innovative materials for electrochemical applications, it is necessary to combine both computational and experimental studies [8]. Different synthesis methods were employed in a report on cobalt sulfide to achieve different morphologies and chemical phases that have been used in electrochemical energy storage applications such as supercapacitors and lithium-ion batteries [5]. Furthermore, cobalt sulfide films have demonstrated amazing potential in electrochemical energy storage applications [9], suggesting that various nanostructured materials may be developed depending on the synthesis approach. As a result, Section 3 discusses a few different synthesis techniques desirable for electrode materials for electrochemical energy application. Despite the progress, a lot of issues remain to be resolved. Renewable electrochemical energy storage technologies necessitate investigating and improving high-efficiency and ecologically friendly electrode materials.

In this review, the latest advances in synthesis methods, design concepts, and electrochemical and mechanical performance of energy storage devices are covered with a specific focus on batteries and supercapacitors. We begin by discussing electrochemical energy storage systems based on chalcogenides, followed by a detailed description of

various selected metal chalcogenide synthesis processes. We will pay particular attention to the role of chalcogenides in various battery and supercapacitor technologies. Finally, future research objectives and perspectives on chalcogenides for flexible electronics are highlighted and reviewed.

2. Types of Electrochemical Energy Storage Devices

2.1. Batteries

An electrochemical battery energy storage solution is required for our sustainable future. For decades, rechargeable batteries have been transforming the battery industry. These rechargeable batteries, including Li-ion, Pb–acid, Ni metal-hydride, and Ni–Cd batteries, dominate the global market. Lithium-ion batteries are currently in the industry. Li-ion batteries are made up of four major components: a cathode, an anode, an electrolyte, and a separator. This is depicted in Figure 3.
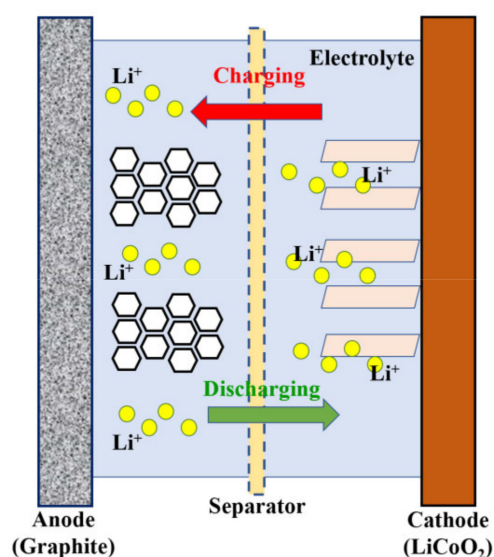

Figure 3. Schematic of the structure and working mechanism of Li-ion batteries.

While graphite is often used for the anode electrode, lithium metal oxides or phosphates, such as $LiCoO_2$ and $LiFePO_4$, are commonly used for the cathode electrode. In order to maintain charge balance, electrons migrate from the anode to the cathode during discharge, which implies Li-ions flow through the electrolyte and cross over the separator. On the other hand, the charging process is triggered by a charging power source, which causes the Li ions to migrate in the opposite direction [10]. As previously mentioned, one of the most important components of electrochemical Li-ion batteries is the electrode materials, which significantly impact battery performance. Therefore, it is important to review the role of chalcogenides in the synthesis and design of appropriate electrode material for high-performance Li-ion batteries. A closely related lithium element is sodium (group 1 element). Hence sodium-ion batteries have been investigated as an alternative sustainable energy storage solution. Because Na-ion has a larger atomic radius compared to Li-ion, they are expected to migrate at a slower rate [11]. However, reports demonstrated that the migration barrier could be shortened for a layered structured system [12–14].

Figure 4 illustrates the structure of Na-ion batteries showing the materials for the four major components: a cathode, an anode, an electrolyte, and binders. Investigating the potential of Na-ion batteries as an alternative electrochemical energy storage device is critical in the development of sustainable, innovative storage systems.

Figure 4. Schematic of the structure and illustration of a Na-ion battery system. Adapted with permission [15]. Copyright (2017) Royal Society of Chemistry. This article is an open access article distributed under the terms and conditions of the Creative Commons Attribution (CC BY) license.

While investigating the electrochemical performance and environmental friendliness of several new electrode materials, most Na-ion batteries and, to a large extent, Li-ion batteries focused on transition metal sulfides-based materials such as cobalt sulfides, iron sulfides, nickel sulfides, and tin sulfides. The storage of Na-ions in metal sulfide materials depends on the transition metal elements that are present in the metal sulfide materials. Developing new electrode materials with specific structures necessitates a thorough understanding of Na-ion transport properties in various electrode materials. The importance of understanding the role of chalcogenides in the synthesis and design of acceptable electrode materials for high-performance Na-ion batteries cannot be overstated.

As with so many other battery energy storage solutions for our sustainable future, there is a continuing desire for new technologies with higher storage capacities and fewer demands on critical minerals. Metal–Sulfur batteries have recently received significant attention [16]. In theory, lithium–sulfur batteries, for example, could store five times as much energy as lithium-ion batteries. Similar to other electrochemical batteries, lithium–sulfur batteries are made of two electrodes (lithium anode and sulfur cathode), a separator, and an electrolyte (either solid or liquid). The fundamental charging and discharging process is depicted in Figure 5, and it is governed by the equation $S + 2Li \rightarrow Li_2S$. From Figure 5, lithium metal is oxidized to Li^+ at the anode, and sulfur is reduced to lithium sulfide (Li_2S) at the cathode during the discharge process. Lithium–sulfur batteries have several drawbacks, the most significant of which are their short cycle life, low utilization of active materials, early failure due to electrical shorting, and anode rechargeability. Another considerable drawback that has received more attention is the suppression of the polysulfide shuttle in lithium–sulfur batteries. According to a study, the effects of polysulfide shuttle can be mediated by including polysulfide absorbant and mediators as part of the cathode material [17]. Several strategies have been used to suppress polysulfide shuttle effects, including the use of electrolyte additives at the anode, the use of porous layers to impede diffusion, the use of a selective electrolyte separator, and the encapsulation of polysulfides at the cathode [18,19].
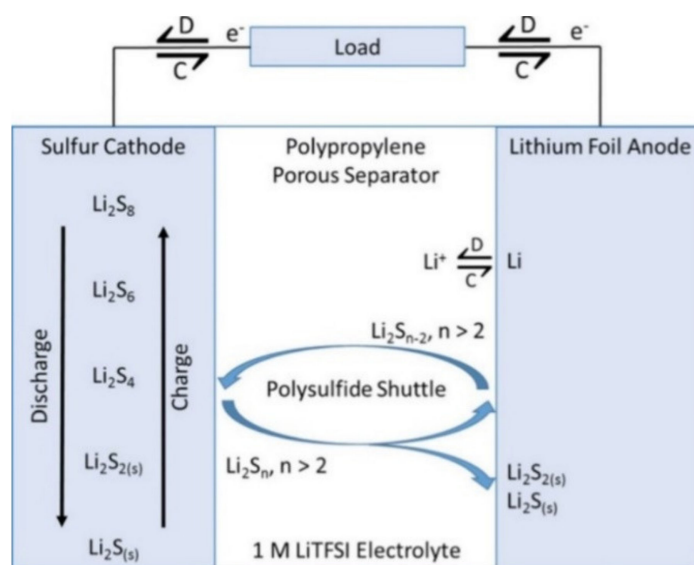
Figure 5. Schematic diagram of a Li–S cell structure with charge/discharge operations. Adapted with permission [18]. Copyright (2017) The Electrochemical Society. This article is an open access article distributed under the terms and conditions of the Creative Commons Attribution (CC BY) license.

The ideal material for electrochemical energy storage must exhibit superior electrochemical properties. The electrochemical performance of electrode materials is mostly determined by the composition and structure/morphology of the materials. There has been a lot of interest in electrocatalysts of chalcogenides because of their intrinsic electrochemical activities [20,21]. Transition metal dichalcogenide (molybdenum disulfide) was utilized as a catalyst in a study to convert polysulfides into a sulfur cathode because of its inherent sulfur deficiencies. Nanocomposites of MoS_{2-x} nanoflakes were created on thin films of reduced graphene oxide utilizing co-dispersion and filtration processes. The steps in the preparation of MoS_{2-x}/rGO are depicted in Figure 6. Surface sulfur deficiency at the cathode had a favorable effect on the kinetics of polysulfide shuttling. As a result, the nanocomposite sulfur cathode with only a small amount of MoS_{2-x}/rGO (4%) exhibited a high-rate capability and a long cycle life. This emphasizes the importance of designing cathode material composition and structure/morphology to improve the electrochemical performance of emerging technologies [22].

Metal–Air batteries have also demonstrated enormous potential in the field of electrochemical energy storage systems. A conventional metal–air battery consists of a metal electrode, an air-breathing cathode, and a lithium salt-containing electrolyte. The anode of metal–air batteries can be made using low-cost, environmentally friendly elements, such as Fe, Na, Al, and Zn. Metal–Air batteries are both safer and offer comparable energy density. Figure 7 shows the theoretical energy density and specific energy of commonly published metal–air batteries.

In a conventional metal–air battery structure (Figure 8), metal is converted to ions at the anode, while oxygen is transformed into hydroxide ions at the cathode. The utilization of air (ambient oxygen) has the extra benefit of lowering costs and simplifying cell construction. Metal–Air batteries such as Li–air battery [24,25], Na–air battery [26,27], Al–air battery [28,29], Mg–air battery [30,31], Zn–air battery [32,33], Fe–air battery [34–36]. Sn–air battery has widely been published, and the electrochemical performance and prospects of improved specific power and specific energy are well established. Indeed, the prospects of using metal chalcogenides as a possible anodic material offer a green and sustainable solution. In this vain, Lyu et al. [37] used a hybrid CoS_2/rGO cathode catalyst to fabricate Li–O_2 batteries. The electrodes exhibited high-rate performance. Furthermore, cobalt sulfide nanoparticles coated on graphene nanosheets have been shown to produce Zn–air batteries with outstanding cycling stability and high rechargeability [38].
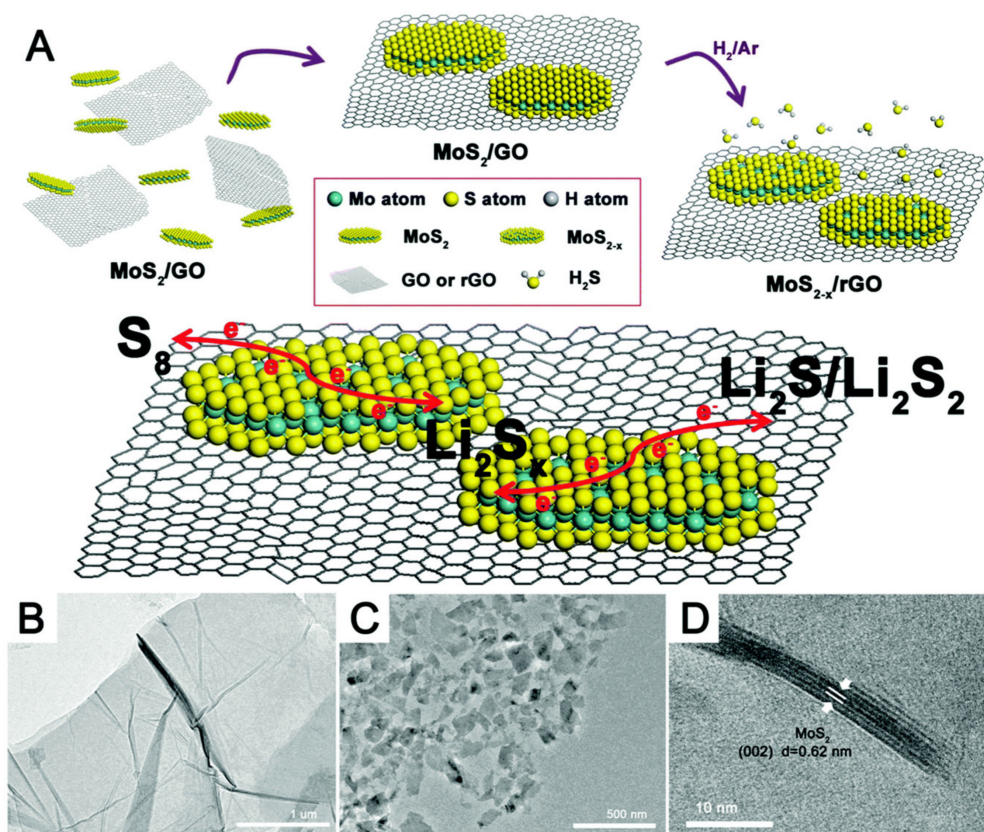
Figure 6. (**A**) Schematic of the synthesis of the MoS_2-x/rGO composite and the conversion of Li_2S_x on the MoS_2-x/rGO surface. TEM images of (**B**) a thin GO film and (**C**) MoS_2 nanoflakes. (**D**) HRTEM image of MoS_2 nanoflakes. Adapted with permission [22]. Copyright (2017) The Royal Society of chemistry. This article is an open access article distributed under the terms and conditions of the Creative Commons Attribution (CC BY) license.
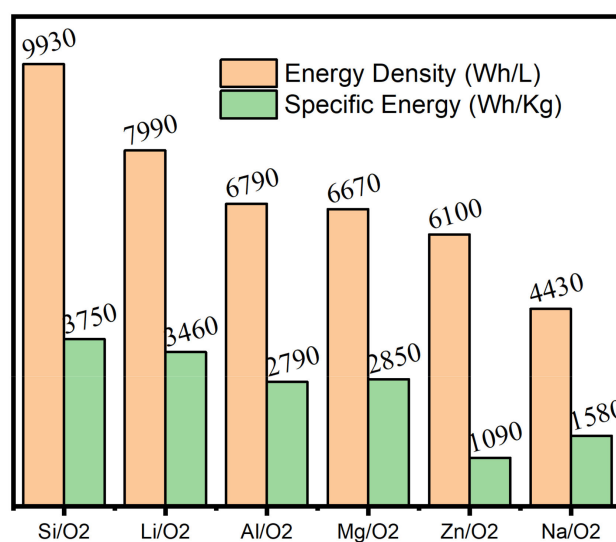
Figure 7. Theoretical energy density and specific energy (including oxygen) of commonly researched metal–air batteries. Adapted from [23]. Copyright (2021) MDPI. This article is an open access article distributed under the terms and conditions of the Creative Commons Attribution (CC BY) license.

Figure 8. Schematic representation of metal–air batteries with aqueous (upper, blue) and nonaqueous (below, green) electrolytes. Adapted from [39]. Copyright (2021) MDPI. This article is an open access article distributed under the terms and conditions of the Creative Commons Attribution (CC BY) license.

2.2. Supercapacitors

Electrochemical energy storage systems such as supercapacitors offer tremendous opportunities for clean energy storage. They comparatively offer high power dens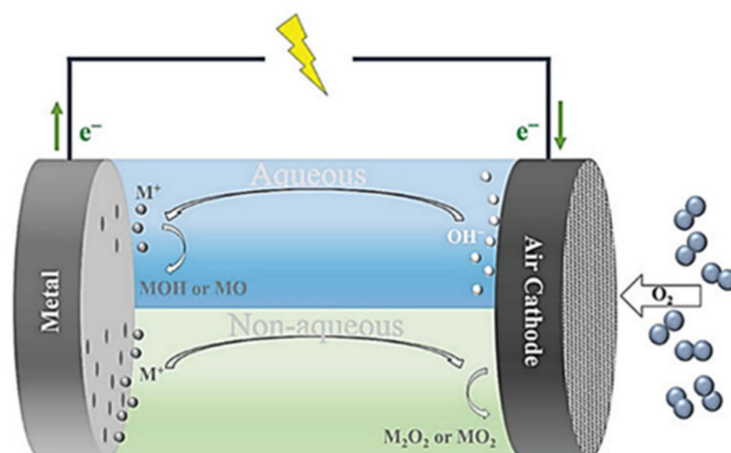ity, long cycle life, and fast charging. It is expected that next-generation storage devices will be dominated by electrochemical storage systems. The development of electrochemical energy storage systems with superior energy requires novel electrode materials, and these electrode materials are critical to the electrochemical performance of the storage device. In this section, we will explore supercapacitors that are based on chalcogenides electrodes. A manufactured supercapacitor can be classified as symmetric or asymmetric based on the configuration of the electrodes. The anodic and cathodic electrode materials in symmetric supercapacitors are identical, whereas the anodic and cathodic electrode materials in asymmetric supercapacitors are distinct. Asymmetric supercapacitors have a significantly greater potential range. This has made it more appealing. When it comes to supercapacitors, the electrode is the most critical component. For a supercapacitor to have improved electrochemical performance, the materials that are utilized to construct the electrodes must be of high performance. Scientists are attempting to develop low-cost electrode materials that have a high specific surface area, good electronic conductivity, and are stable.

The electrochemical activity of TMCs significantly influences the effectiveness of electrodes used for supercapacitor electrodes. The electrochemical activity of the electrode material regulates electrochemical performance, such as energy density and power density. Many factors influence supercapacitor electrochemical performance, including nanostructure orientation and bond mechanisms. Even though several innovative materials (for example, metal oxides) have demonstrated considerable potential as supercapacitor electrodes, several of them have also demonstrated significant limitations [40,41].

Therefore, it is essential to investigate novel electrode materials that exhibit superior electrochemical performance. A possible approach in this regard is the employment of chalcogenides, which operate based on a pseudocapacitive (fast reversible redox mechanism) or hybrid (combination of charge accumulation and fast reversible redox mechanism) charge storage mechanism to store and release electrochemical energy. Chalcogenides, especially metal sulfides, metal selenides, metal tellurides, etc., have been widely applied in supercapacitor applications due to their excellent electrochemical activity. Despite this, there are a few drawbacks to using chalcogenides as an electrode material, including low conductivity, poor cyclability, a low surface area, and aggregation problems [42–44]. Several synthesis approaches have been used to create electrodes with high surface area by utilizing nanostructured features such as nanowires, nanorods, and nanobelts. However, to attain

improved electronic conductivity and stability, the use of different active materials must be investigated.

In a reported attempt to improve the electrochemical activity by improving the surface area, chalcogenides based supercapacitors, ternary metal chalcogenides hybrid super-capacitors (MX; M = Zn–Co–Ni; X = S, Se, Te) were fabricated [45]. On nickel-based substrates, a well-organized nanostructured needlelike feature that looks similar to sea urchins was fabricated. The sample had a lot of voids and exhibited improved specific capacitance and stability. By using selenization, tellurization, and sulfurization of pre-cursors, the morphology of the sample could be altered to affect the specific capacitance. Some chalcogenides-based electrode material exhibits inherently high electronic conduc-tivity [46,47]. For example, MoS_2 has a lower electronic conductivity compared to WS_2; to tackle this, researchers have employed different synthesis methods to fabricate various nanostructured electrodes for supercapacitor applications.

Furthermore, other nanocomposites have been investigated to improve electronic conductivity [48–51]. Teli et al. produced an interconnected crumpled-nanoflake structured MoS_2 on Ni foam using a one-step electrodeposition method [46]. The fabricated electrodes exhibited diffusion-controlled or capacitive-controlled charge storage kinetics and excellent coulombic efficiency. When employed as an electrode material for supercapacitor appli-cations, WS_2/α-$NiMoO_4$ composite electrodes with nano/micro cavity-like hierarchical architecture exhibited high specific areas with increased pore size, superior electrical con-ductivity, and improved stability [52]. Cobalt sulfide (CoS) has generated much research attention because they are low-cost and possess a weak Co–S bond that exhibits theoretically high capacitance. As a result, transition metal sulfides for use in superca-pacitor applications have been developed. For example, Zhang's research group fabricated CoS nanowires on layered $Ti_3C_2T_x$ using the solvothermal method [52]. With the $Ti_3C_2T_x$ layer providing large interlayer spacing, improved conductivity, and chemical diversity on the surface, the samples exhibited remarkably improved electrochemical performance. In another research, 2D hierarchical MoS_2 lamella inserted in the CoS_2 flake was fabricated. The 2D MoS_2 multilayers provided support preventing interlayer expansion and structural collapse. The electrochemical performance and cyclic stability of these chalcogenides can be improved with secondary support [53]. Other typical chalcogenides [54–62] also demon-strated great potential for supercapacitor applications. However, before delving into their performance in-depth, a brief overview of their synthesis methodologies is required, which is covered in the next section.

3. Chalcogenides for Electrochemical Energy Storage Devices

3.1. Synthesis of Chalcogenides

The synthesis of chalcogenide-based compounds to attain desirable characteristics for electrochemical applications is covered in this section. Chalcogenide-based compounds come in a wide range of structural orientation and bond mechanisms, ranging from binary to multinary compound systems. The synthesis techniques used in preparing chalcogenide-based nanostructures dictate structural orientation, stoichiometry tuning, surface modifi-cation, and bond mechanisms. As a result, novel cutting-edge fabrication and processing methods and a fundamental understanding of the relationship between the structure and properties of chalcogenide-based compounds have been the focus of scientists over the past decades. Scientists have developed numerous strategies for preparing nanostructured chalcogenide compounds. The methodologies for creating modified chalcogenide-based nanostructures can be broadly classified into three types: one-pot synthesis, in situ synthe-sis, and ex situ synthesis (Figure 9).
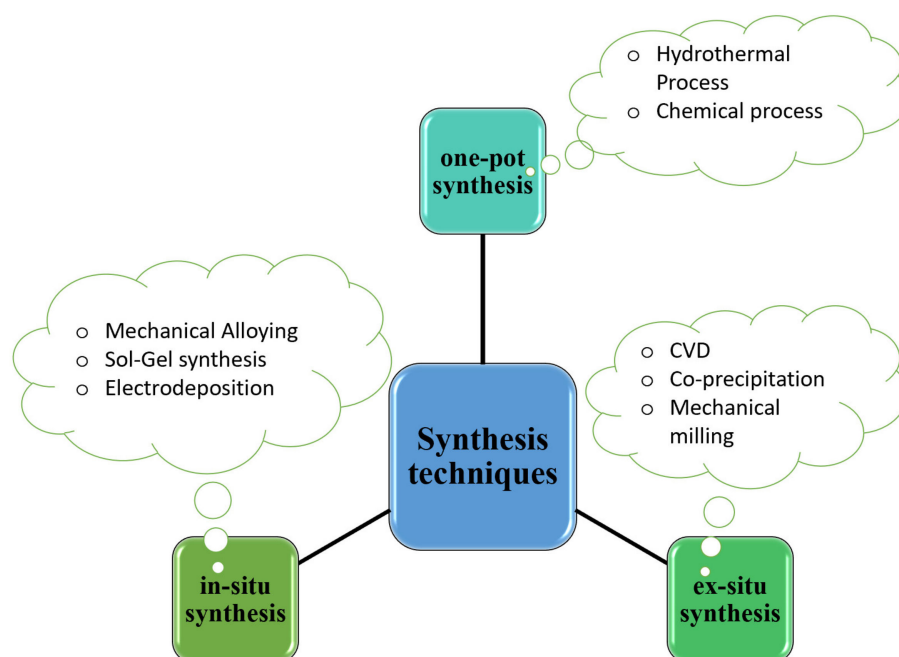
Figure 9. Synthesis techniques of chalcogenide-based nanostructures.

The one-pot synthesis systems are exceptionally easy to set up and manage, it involves sequential chemical reactions in a single reactor. It is quite efficient and less time-consuming, and it may entail the synthesis of complex structures in a single reaction step. It is also suitable for industrial processing. It is always necessary to use a substrate during in situ synthesis because it supports the growth or nucleation of reactants. This approach allows for the creation of nanostructures in a variety of shapes, including planar and non-planar ones. The term "ex-situ synthesis approach" refers to the technique of synthesizing the reacting components separately and then combining them through an intermediary procedure after they have been created. It takes longer and consumes more energy to do ex situ synthesis than it would otherwise. This is due to the additional intermediary step. Nonetheless, the uniqueness of each of these synthesis techniques requires specialized equipment and expertise in manipulating the procedure to attain the desired structures.

In order to make nanostructured materials, one or a combination of these synthesis methods can be used alone or in conjunction with the others. In a representative approach, a novel route for the preparation of a two-phase film of $4Ni(OH)_2 \cdot NiOOH@Co_9S_8$ on Ni foam was developed through a chemical bath followed by hydrothermal electrodeposition. This was carried out by a one-step synthesis process in an autoclave. The reported improved electrochemical performance was explained based on the synergistic effect of NiCo–OH and CoS providing fast ion and electron conductions [63]. In a similar report, Cu_2MoS_4 nanostructures were prepared using a one-pot hydrothermal route. The I-phase Cu_2MoS_4 electrode exhibited exceptional pseudocapacitive charge-storage via ion intercalation/de-intercalation [64].

MoS_2 NPs rolled r-Graphene/mesoporous MnOx nanofibers composite were prepared by a two-step template-free method [65]. By applying a two-stage approach, the morphology of the electrodes was tuned to a flaky pasty and nanofiber morphology. The electrodes exhibited improved thermal charge/discharge cycle stability [65]. The synthesis procedure has a direct impact on the electrode's electrochemical performance, as demonstrated in the described work. A one-pot hydrothermal method approach for making cobalt–magnesium selenates electrode was employed as an advanced electrode for electrochemical energy storage [66]. By changing growth time and temperature, nanosheet arrays and nanowire morphology were observed. Figure 10 illustrates the synthesis procedure used and the observed morphology.
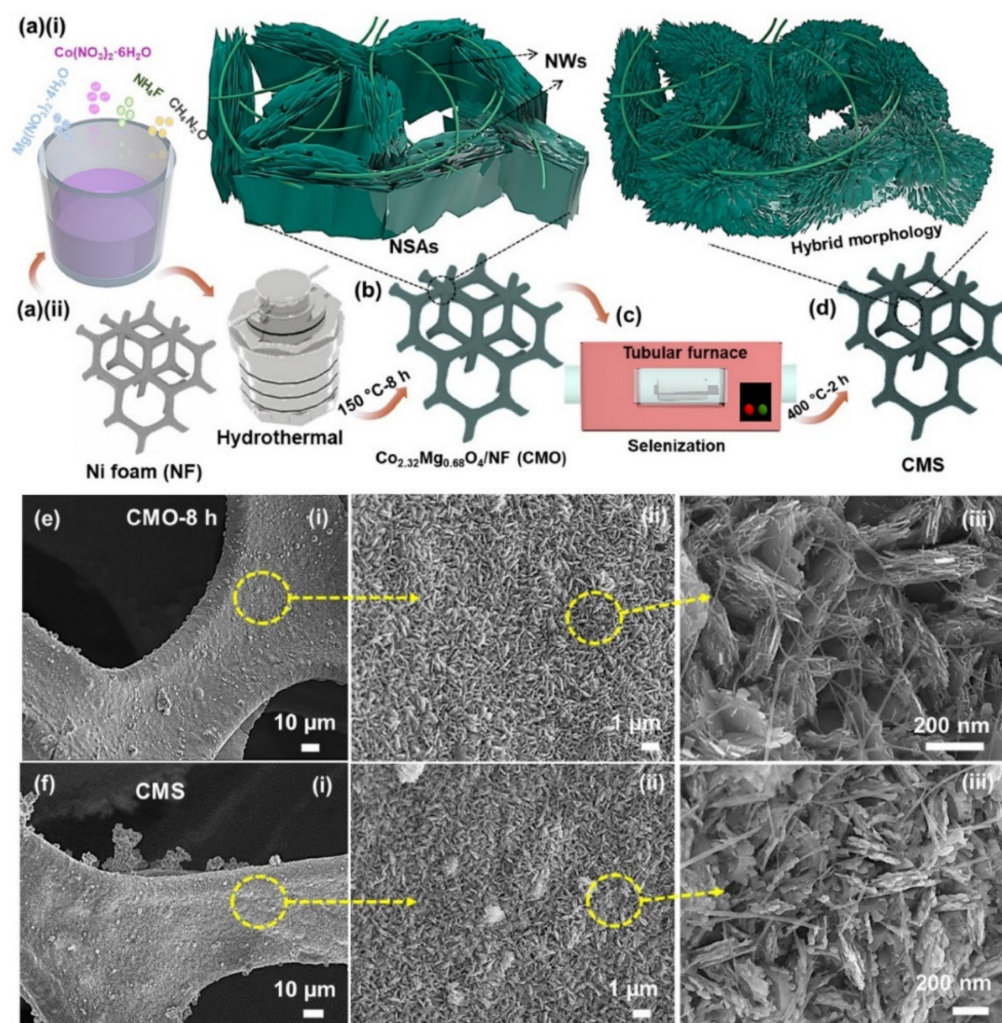
Figure 10. Schematic diagram for the preparation of the (**a,b**) cobalt–magnesium oxide −8 h material with hybrid morphology and (**c,d**) cobalt–magnesium selenates material. FE-SEM images of the (**e**) cobalt–magnesium oxide −8 h and (**f**) cobalt–magnesium selenates materials. Adapted with permission [66]. Copyright (2022) Elsevier B.V. This article is an open access article distributed under the terms and conditions of the Creative Commons Attribution (CC BY) license.

Various nanostructures of NiCoSe$_2$, NiCo$_2$S$_4$, and NiCo$_2$O$_4$ were obtained using the hydrothermal synthesis method. Electrode fabricated using these materials can be used for both electrochemical sensor and supercapacitor applications. They reported improved electrochemical kinetics and excellent specific capacitance [67]. Many other authors have reported the synthesis of various chalcogenides nanostructures via numerous methods for electrochemical energy storage applications. Table 1 (chalcogenides for supercapacitors), Table 2 (chalcogenides for batteries), and Table 3 (chalcogenides for fuel cells) show a summary of various chalcogenide materials synthesis route and electrochemical performance parameters.

Table 1. Chalcogenides for supercapacitors.

Material	Synthesis	Potential Window (V)	Electrolyte (M)	Scan Rate (mV/s)	Specific Capacitance (F/g/C/cm²/mF cm⁻²/Cg⁻¹)	Current Density (A/g/mA/cm²/mAcm⁻²)	% Retention Capacity/Cycles	Energy Density (Wh/kg mWh/cm³/μWhcm⁻²)	Power Density (W/kg/mW/cm³/mWcm⁻²)	Ref.
NiS/rGO hybrid	Microwave-assisted hydrothermal	0.46	2 M KOH	5–50	1188.9	5	68.1	7.1	1836	[68]
NiS nanostructures	Microwave-hydrothermal	0.46	2 M KOH	100	119	1	100/2000	16.5	250	[69]
CuFeS₂ nanomaterial	Solvothermal	0.55	6 M KOH	1–50	589	4	82/2000	-	-	[70]
NiSe₂@rGO nanocomposite	Hydrothermal	1.7	2 M KOH	2-50	467		93/6500	34.3	-	[71]
MoSSe/rGO composite	Solvothermal	0.35	3 M KOH	5–50	373	1	89.5/4600	-	-	[72]
MoS2/Ni3S2	Hydrothermal	0.58	1 M KOH	10–100	1.033	1	62.5/10,000	35.93	1064.76	[73]
NiSe₂@Fe3Se₄	chemical bath deposition	1.7	6 M KOH	2–50	147	5	92/10,000	52	398	[74]
NiGa₂S₄ nanosheets	Hydrothermal	1.1	6 M KOH	10–100	488	0.5	109/20,000	40	5.5	[75]
CF@CoS	tube furnace	0.7	2 M KOH	10–100	3576.0	5.0	80/4000	149.4	4.3	[76]
copper sulfide	Chemical reaction	0.8	2 M KOH	1–50	1173	2	99/1500	301.4	1400	[77]
LaDySn₂O₇-SnSe nanocomposite	Hydrothermal	0.2–0.8	0.1 M KOH	10–100	1780	0.3	127/2000	67.46	6157.411	[78]
Zinc cobalt sulfide nano hybrid	hydrothermal	1.8 V	1MTEABF 4acetonitrile (ACN)	10	785	2	106/10,000	49.6	1799.6	[79]
NiCo₂Se₄/RGO (NCSG)	two-step hydrothermal	0.4	6 M KOH	30	1776	2	93.5/5000	66.2	1500	[80]
MoS₂/graphene oxide/meso-MnO₂ nanocomposite	two stage ultra-sonication	-	1 M H2SO4 and KI	1–500	980	0.5	-	-	-	[65]
MoS₂@3DG//NPC	solution-based process	0.0–4.0	1 M LiPF6	0.5	88.3	1.0	78/2000	156	197	[81]
MoS₂-C-RGO//PDPC	hydrothermal	0.01–3.0	1 M LiPF6	0.1	759	2	80/10,000	188	200	[82]

Material	Synthesis	Potential Window (V)	Electrolyte (M)	Scan Rate (mV/s)	Specific Capacitance (F/g/C/cm^2/mF cm^{-2}/Cg^{-1})	Current Density (A/g/mA/cm^2/mAcm^{-2})	% Retention Capacity/Cycles	Energy Density (Wh/kg mWh/cm^3/μWhcm^{-2})	Power Density (W/kg/mW/cm^3/mWcm^{-2})	Ref.
MoS$_2$/CP//AC	ball-milling and pyrolysis	1.5–4.5	1 M LiPF6	10	530	1	79.61/1000	87.74	200	[83]
(P-MoS$_2$/PANI/rGO HNSs)//rGO	hydrothermal	0.3–1.1	1 M Li2SO$_4$	5–20	221.9	5	93.5/30,000	56	0.45	[84]
MoS$_2$ @C//AC	hydrothermal	0.0–4.5	1 M LiPF6	1–20	1083.4	1	72.12/3000	119.68	11.25	[85]
MoS$_2$-C//PDPC	hydrothermal	0.4–3.0	1 M NaClO$_4$	5	200	2	77.3/10,000	111.4	12000	[86]
TiO$_2$/MoS$_2$ @NC//AC	Solid phase reaction	2.0–4.5	1 M NaClO$_4$	0.2	66.3	2	70/3000	148	200	[87]
VSe$_2$/rGO//AC	hydrothermal	1–4	1 M NaClO$_4$	0.5	365	1	68/1000	106	125	[88]
TiS$_2$ @Cpvp//AC	in situ conversion	2.0–4.0	1 M NaPF6	0.2–1.2	340	2	87/5000	101.7	200	[89]
MoS$_2$/CoS$_2$-RGO//Na$_3$V$_2$(PO$_4$)$_3$/C	facile hydrothermal	0.01–4.5	1 M NaClO$_4$	0.1	596.3	2	92.3/1000	152.98	562.5	[90]
CNF@VS$_2$//CNF@GS	Hydrothermal	0.01–3.0	1 M NaClO$_4$	0.5	52.3	5	82/4500	166	0.4	[91]
MoS$_2$/SnS$_2$-RGO//CC	-	0.01–3.00	1 M NaClO$_4$	-	550.3	2	100/3000	113.9	561.25	[92]
MoSe$_2$/TiO$_2$−x/ graphene//AC	hydrothermal	0.5–3.5	1M NaPF6	-	415.2	2	88/3000	109	100	[93]
MoSe$_2$/C//AC	hydrothermal	0.01–3.0	0.8 M KPF6	0.1	320	1	81.58/1000	169	106	[94]
WS$_2$@NCNs//NCHS	Hydrothermal	2.6–4.2	0.8 M KPF6	0.1	44	2	92.2/2000	103.4	235	[95]
MoS$_2$/graphene	L-cysteine-assisted hydrothermal process	−0.1–0 (vs. SCE)	1 M Na$_2$SO$_4$	20	243	1	92.7/1000	73.5	19.8	[96]
MoS$_2$/CA (Carbon Aerogel)	Hydrothermal	−0.8–0.2 (vs. Hg/HgO)	1 M Na$_2$SO$_4$	2–50	260	1	92.4/1500	-	-	[97]
MoS$_2$/graphene aerogel	Hydrothermal	-	1 M Na$_2$SO$_4$	-	268	0.5	93/1000	-	-	[98]
1T-2H MoS$_2$/GA (Graphene Aerogel)	Hydrothermal	−0.8–0.4	1 M H$_2$SO$_4$	-	416	-	-	-	-	[99]

Table 1. *Cont.*

Material	Synthesis	Potential Window (V)	Electrolyte (M)	Scan Rate (mV/s)	Specific Capacitance (F/g/C/cm²/mF cm⁻²/Cg⁻¹)	Current Density (A/g/mA/cm²/mAcm⁻²)	% Retention Capacity/Cycles	Energy Density (Wh/kg mWh/cm³/μWhcm⁻²)	Power Density (W/kg/mW/cm³/mWcm⁻²)	Ref.
NiCo$_2$S$_4$/CS (Carbon Sponge)	Direct carbonization	0–0.9	3 M KOH	5–20	1093	0.5	90/500	-	-	[100]
CoS$_2$/rGO	Solvothermal	−0.3–0.65	6 M KOH	5	331	0.5	97/2000	30	4750	[101]
CuS/rGO	Solvothermal	−0.4–0.6	6 M KOH	50	2317.8	1	96.2/1200	-	-	[102]
CuS/rGO	Solvothermal	0–0.5	6 M KOH	10	906	1	89/5000	105.5	2.5	[103]
CuS/rGO	Solvothermal	−1−−0.1	2 M KOH	5–100	368.3	1	88.4/1000	-	-	[104]
CuS/rGO	Hydrothermal	0–0.5	3 M KOH	5–80	1604	2	97/5000	21	315	[105]
NiCo$_{2.1}$Se$_{3.3}$ NSs/3D G/NF	CVD + Hydrothermal	0–0.6	6 M KOH	3–20	742.4	1	83.8/1000	-	-	[106]
NiCo$_2$Se$_4$-rGO	Hydrothermal	−0.2–0.5	1 M KOH	10–80	2038.55	1	90/1000	67.01	903.61	[107]
NiCo$_2$Se$_4$/rGO	Hydrothermal	−1–0	6 M KOH	30	1776	2	93.5/5000	66.2	1500	[80]
NiCo$_2$Se$_4$/rGO	Hydrothermal	−0.1–0.4	6 M KOH	30	139	2	87.27/5000	37.83	1433.55	[108]
CoNi$_2$S$_4$/rGO	One step pyrolysis	0–1.6	6 M KOH	50	-	-	93.7/8000	54.8	798	[109]
(Cu$_2$NiSnS$_4$)/rGO	Hydrothermal	0–0.6	6 M KOH	-	16.38	5	89.2/2000	5.68	98.8	[110]
MoS$_2$/MWCNT	Hydrothermal	−0.8–0.2	1 M Na$_2$SO$_4$	2–50	452.7	1	95.8/1000	-	-	[111]
MoS$_2$@CNTs/Ni core	PLD	−1–0	1 M Na$_2$SO$_4$	200	512	1	100/2000	25.5	44.2	[112]
CuS/MWCNTs	Hydrothermal	−0.4–0.6	6 M KOH	-	2831	1	90/600	-	-	[113]
CuS/CNT	PVP assisted refluxing	0–0.6	2 M KOH	20	2204	10	89/10,000	-	-	[114]
CuS/CNT	Hydrothermal	−0.2–0.6 (vs. Hg/HgO)	2 M KOH	1–50	566.4	1	94.5/5000	50.4	-	[115]
NiS/CNT	CBD + SILAR	−0.2–0.6	1 M Na$_2$S, 2 M S, and 0.1 M KCl in methanol: water (7:3)	100	398.16	1	98.39/1000	35.39	145.45	[116]

Table 1. *Cont.*

Material	Synthesis	Potential Window (V)	Electrolyte (M)	Scan Rate (mV/s)	Specific Capacitance (F/g/C/cm^2/mF cm^{-2}/Cg^{-1})	Current Density (A/g/mA/cm^2/mAcm^{-2})	% Retention Capacity/Cycles	Energy Density (Wh/kg mWh/cm^3/μWhcm^{-2})	Power Density (W/kg/mW/cm^3/mWcm^{-2})	Ref.
CNT/CoS	CBD + SILAR	−0.2–0.6	1 M Na$_2$S, 2 M S, and 0.1 M KCl in methanol: water (7:3)	100	288.43	1	95.3/1000	25.63	145.45	[116]
CNT/CuS	CBD + SILAR	−0.2–0.6	1 M Na$_2$S, 2 M S, and 0.1 M KCl in methanol:water (7:3)	100	176.2	1	78.57/1000	15.66	145.45	[116]
CNT/PbS	CBD + SILAR	−0.2–0.6	1 M Na$_2$S, 2 M S, and 0.1 M KCl in methanol:water (7:3)	100	101.94	1	69.49/1000	9.06	145.45	[116]
NiS$_2$/MWCNTs	Solid state method	−0.2–0.5	2 M KOH	2–20	2054.28	2	99.99/10,000	-	-	[117]
Ni$_3$S$_2$/CNT	Electrodeposition + ion exchange	−0.1–0.6	3 M KOH	30	1643	1	91.5/2000	-	-	[118]
VS$_2$/MWCNT	SILAR	−0.6–0.2	2 M KCl	100	182	2	95.9/1000	42	2.8	[119]
TiS$_2$/CNTs	Atomic layer deposition/sulfurization	−1.5–1.5	21 m LiTFSI/5% PVA	1–50	195	1	95/10,000	60.9	1250	[120]
NiS/graphene/CNT	Hydrothermal	−0.1–0.35	6 M KOH	100	2377	1	68/1000	14	16	[121]
MoS2@rGO-CNT	Micropatterning + pyrolysis	0–1	H$_2$SO$_4$/PVA gel	-	13.7	1	96.6/10,000	5.6	-	[122]
Hollow MoS$_2$/Carbon	Sonogashira coupling	−0.5–0.5	0.5 M Na$_2$SO$_4$	-	418	0.5	-	-	-	[123]
MnS/MoS$_2$/Carbon	Calcination+ sulphuration	0–1.55	2 M KOH	-	1162	0.5	81/5000	31	388.3	[124]
CoSe2/N-doped Carbon	Selenylation	0–0.4	6 M KOH		120.2	1	92/10,000	40.9	980	[125]

Table 1. *Cont.*

Material	Synthesis	Potential Window (V)	Electrolyte (M)	Scan Rate (mV/s)	Specific Capacitance (F/g/C/cm²/mF cm⁻²/Cg⁻¹)	Current Density (A/g/mA/cm²/mAcm⁻²)	% Retention Capacity/Cycles	Energy Density (Wh/kg mWh/cm³/µWhcm⁻²)	Power Density (W/kg/mW/cm³/mWcm⁻²)	Ref.
MoS2/NiCo2S4@Carbon	Self-templating	0–0.5	6 M KOH	10	250	2	90.1/10,000	36.46	73.75	[126]
CoTe/MOF	Hydrothermal	0–0.5	2 M KOH	5–100	297.27	2	83.33/10,000	43.84	738.88	[127]
Ni$_3$S$_2$/AC	Electrodeposition	0–1.4	PVA-KOH gel	10	2797.43	1	83.47/10,000	55.32	1053.71	[128]
ZnS/CuS/AC	SILAD	0–1.2	PVA-KOH gel	-	1925	4	79/2000	-	-	[129]
MoS$_2$/GA	Hydrothermal	−0.3–0.7	1 M Na$_2$SO$_4$	50	268	0.5	93/1000	-	-	[130]

Table 2. Chalcogenides for batteries.

Material	Synthesis	Voltage Range	Cycling Performance (mAh g^{-1}/No. of Cycles)	Maximum Rate Capability (mAh g^{-1}/)	Current Density (A/g/mA g^{-1})	Ref.
MoS$_2$@N-doped carbon nanowall @carbon cloth	Solvothermal	0.01–3	619.2/100	235	2	[131]
MoS$_2$/carbon fiber @MoS$_2$@C	Electrospinning	0.01–2.5	332.6/1000	233.6	10	[132]
MoS$_2$@CF	Vacuum infiltration	0.05–3	240/500	171	5	[133]
MoS$_2$/single-wall carbon nanotubes	Liquid Phase Exfoliation	0.1–3	390/100	192	20	[134]
N-doped hollow MoS$_2$/C nanospheres	Hydrothermal	0.01–3	128/5000	242	5	[135]
MoS$_2$/graphene	Ball milling/exfoliation	0.01–2.7	421/250	201	50	[136]
MoS$_2$/S-doped graphene	Hydrothermal	0.005–3	309/1000	264	5	[137]
Fe$_3$O$_4$@MoS$_2$ graphite paper	Modified hydrothermal	0.01–3	388/300	231	3.2	[138]
1T MoS$_2$/graphene tube	Solvothermal	0.01–3	313/200	175	2	[139]
MoS$_2$/cotton-derived carbon fibers	hydrothermal	0.01–3	323.1/150	355.6	2	[140]
NBT/C@MoS$_2$ NFs	electrospinning	0.01–3.0	448.2/600	2000	200	[141]
N-doped amorphous micron-sized carbon ribbons @MoS$_2$	Hydrothermal	0.01–3	305/300	302	2	[142]
Hollow flower-like MoS$_2$@C-RGO	one-pot hydrothermal	0.01–3	637/50	467	1	[143]
amorphous MoS$_3$@carbon nanotube	Facile acid precipitation method	0.05–2.8	565/100	2350	20	[144]
MoSe$_2$/N, P-rGO	solvothermal	0.01–3	378/1000	216	15	[145]
MoSe$_2$@MWCNT	one-step hydrothermal	0.01–3	459/90	385	2	[146]
VS$_4$-rGO	in situ hydrothermal	0.01–3	540/50	123	20	[147]
VS$_4$/rGO	hydrothermal	0.01–2.2	241/50	219.9	0.5	[148]
Co$_9$S$_8$@C nanospheres	facile hydrothermal	0.01–3	305/1000	297	5	[149]
CoS$_2$@ multichannel carbon nanofibers	facile solvothermal	0.4–2.9	315.7/1000	201.9	10	[150]
CoS$_2$eMWCNT	simple hydrothermal	1–2.9	568/100	550.5	0.8	[151]
Sb$_2$S$_3$ nanorods/C	facile hydrothermal	0–2	570/100	337	2	[152]
Sb$_2$S$_3$/S-doped graphene sheets	ultrasonication	0.01–2.5	524.4/900	591.6	5	[153]
ZnSeSb$_2$S$_3$@C	sulfurization reaction	0.01–1.8	630/120	390.6	0.8	[154]
Sb$_2$Se$_3$/C rods	self-assembly reaction	0.01–2.5	485.2/100	311.5	2	[155]
Sb$_2$Se$_3$ nanowire-based membrane	Hydrothermal/vacuum filtration	0.01–2	296/50	153	1.6	[156]
SnS/3D N-doped graphene	Facile, self-assembly method	0.01–2.5	509.9/1000	404.8	6	[157]
NiS$_2$@CoS$_2$@N-doped carbon coreshell nanocubes	co-precipitation method	0.01–3	600/250	560	5	[158]

Table 2. *Cont.*

Material	Synthesis	Voltage Range	Cycling Performance (mAh g^{-1}/No. of Cycles)	Maximum Rate Capability (mAh g^{-1}/)	Current Density (A/g/mA g^{-1})	Ref.
SnS$_2$/EDA-RGO	Hydrothermal	0.01–3	480/1000	250	11.2	[159]
MnS@CNF film	Electrospinning/thermal treatment	0.01–3	220/200	107	0.5	[160]

Table 3. Chalcogenides for fuel cells.

Material	Synthesis	Electrolyte	Current Density (mA cm^{-2}/Ag^{-1})	Potential (mV/V)	Ref.
β-NiS	Facile Hydrothermal	1 M NaOH	40	598	[161]
Ni$_3$S$_2$@NF	Hydrothermal	1 M NaOH	275	531	[162]
Ni–Co$_9$S$_8$	Hydrothermal	1 M KOH	75	478	[163]
NiCo$_2$S$_4$/C	Pyrolysis/hydrothermal	1 M KOH	100	180	[164]
NiS@C$_2$-550	Hydrothermal	1 M KOH	360	~577	[165]
MoS$_2$/Ni$_3$S$_2$/NiFe-LDH/NF	two-step hydrothermal	1 M KOH	280	~548	[166]
NiSe$_2$	Hydrothermal	1 M KOH NG	105	502	[167]
CoSe$_2$	one-step selenylation	1.0 M KOH	10	330	[168]
Ni–Co–S	electrodeposition	1.0 M KOH	100	363	[169]
(CoMn)Se$_2$	selenation	1.0 M KOH	10	270	[170]
NiCoSe$_2$	electrodeposition	1.0 M KOH	10	256	[171]
NiFeCoSe$_x$	electrodeposition	1.0 M KOH	10	150	[172]
NiCoFe-PS	hydrothermal electrodeposition	1.0 M KOH	10	195	[173]
CoOSeP/Co foil	thermal selenization	1.0 M KOH	10	155	[174]
CoP/CN@MoS2	solvothermal	1.0 M KOH	10	289	[175]
Co$_9$S$_8$/Co$_3$O$_4$	hydrothermal-sulfurization method	1.0 M KOH	20	260	[176]
Co$_3$O$_4$/MoS$_2$	liquid-phase deposition	1.0 M KOH	20	230	[177]
Ni$_3$S$_2$/Co(OH)$_2$	facile hydrothermal	1.0 M KOH	10	257	[178]
Co$_9$S$_8$/NiCo LDH	two-step hydrothermal	1.0 M KOH	30	278	[179]
NiFe/Co$_9$S$_8$	chemical bath deposition	1.0 M KOH	10	219	[180]
CoCO$_3$/CoSe	two-step hydrothermal	1.0 M KOH	10	255	[181]
CoO/CoSe$_2$	Hydrothermal	1.0 M KOH	10	510	[182]
CoMoNiSeNF	one-pot hydrothermal	1.0 M KOH	10	405	[183]
Co$_9$S$_8$	hydrothermal	1.0 M KOH	10	1.66	[184]
p-CoSe$_2$/CC	electrodeposition	1.0 M KOH	10	1.62	[185]
Co$_{0.85}$Se	liquid-phase chemical conversion	1.0 M KOH	10	1.60	[186]
Co$_{0.75}$Ni$_{0.25}$Se/NF	thermal conversion	1.0 M KOH	10	1.60	[187]
CoMoNiSeNF	hydrothermal	1.0 M KOH	10	1.45	[183]
CoeO/CoeSe/Cu	electrodeposition	1.0 M KOH	10	1.65	[188]
Co$_9$S$_8$/NiCo LDH/NF	hydrothermal	1.0 M KOH	10	1.63	[179]

3.2. Applications of Chalcogenides in Batteries

Rechargeable batteries, such as metal-ion batteries (MIBs), metal–sulfur batteries (MSBs), and metal–air batteries (MABs), have received a lot of press recently because of their improved efficiency, cheaper cost, and lower pollution. However, these energy storage devices' electrochemical performance (power density, energy density, charge–discharge rate, cycle performance, etc.) still needs to be improved. As a result, much research has shown that electrode materials have a large impact on electrochemical performance, implying that finding suitable materials is a key strategy for developing an effective energy storage device. Metal chalcogenides (MCs) have received a lot of interest because of their diverse structural kinds, abundant supply, low cost, high capacity, and incredible electrical conductivity [189–191]. Furthermore, as shown in Figure 11a, research on chalcogenides as electrode materials in rechargeable batteries has increased rapidly in the last decade, with MIB research taking the lead. Figure 11b shows the proportions and instances of such electrodes in various rechargeable batteries.
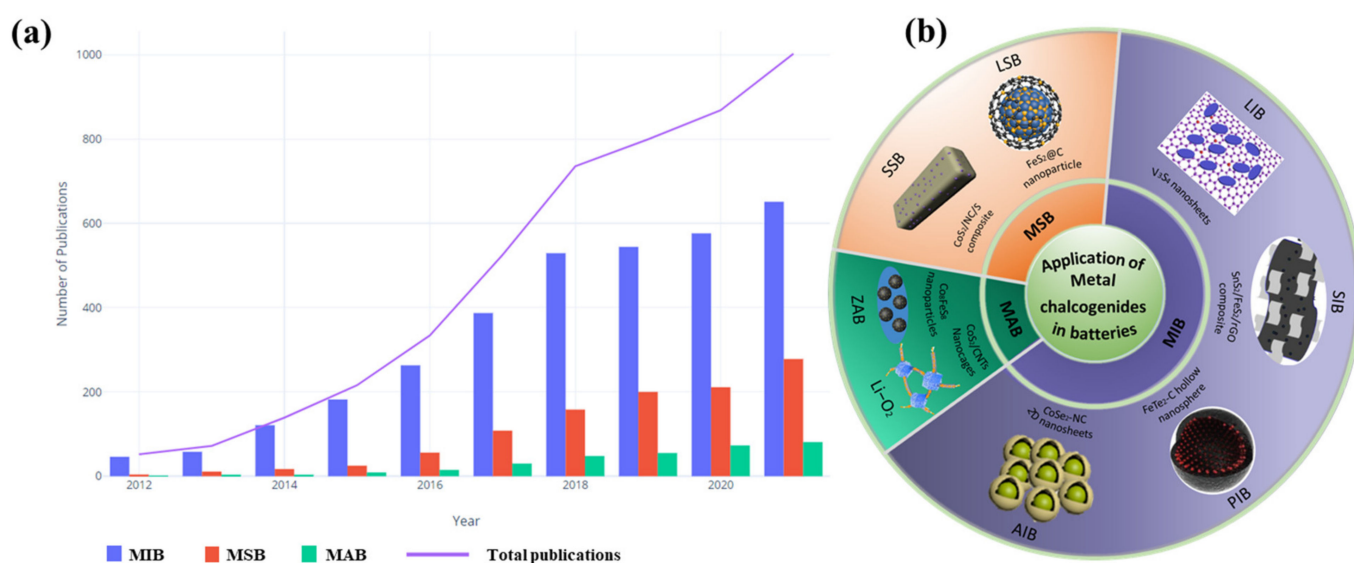
Figure 11. (**a**) Research trends for many published papers on metal chalcogenides for MIB, MSB, and MIB (**b**) Pie chart of Chalcogenides for Metal batteries in the last decade, with imbedded examples.

3.2.1. Applications of Chalcogenides in Metal-Ion Batteries

Metal-ion batteries are key enablers in the present transition from fossil fuels to renewable energy for a better society, with cleverly developed materials serving as the technology driver. Despite this, they have significant scalability and durability issues. A fundamental question is how to design appealing structural frameworks for enhanced electrodes and electrolytes for the next generation of batteries using the most efficient materials. Metal chalcogenides have received a lot of interest as a potential electrode for attaining the finest characteristics [192–194]. The most prevalent MIBs are listed in Table 4, along with their method of preparation, structure, and electrochemical properties.

Table 4. Electrochemical performance of some common MIBs in literature.

Material	Structure	Preparation Method	Rate Performance [Capacity (mAh g^{-1}) @ Current Density (Ag^{-1})]	Cycle Performance [Capacity (mAh g^{-1}) @ Current Density (Ag^{-1}) @ Cycles]	Ref.
LIB anode					
α-MnSe/CNF	Microspheres	Selenization	1226.75@0.1	845.54@0.1@100	[195]
α-MnSe/C	Microspheres	Selenization	945.78@0.1	784.82@1@100	[195]
Co$_9$S$_8$@CN	Nanoparticles	Direct annealing	618.1@ 0.1	406.5@1@100	[196]
SnS$_2$@g-C$_3$N$_4$	Porous nanosheets	Sintering	1592.8@0.5	1305.7@0.5@600	[197]
ZnS-QD@NC	Polymorph structures	Pyro-synthesis technique	805@0.1	620@1@500	[198]
CoSe/Co–NCNS	Layered structure	Selenization + annealing	401@0.2	640@1@500	[199]
Sb$_2$Se$_3$/C	Helical nanoparticles	Selenization	548@0.25	545@0.25@1000	[200]
SnSe$_2$/graphene	Heterostructure nanosheets	Hydrothermal	490.9@0.1	291.1@0.1@1500	[201]
SnS/TiS$_2$/GO	Misfit-layered heterostructure	Solvent-free hand-grinding	1147@0.5	614@2.0@1000	[202]
g-C$_3$N$_4$@WS$_2$	Hierarchical	Solvothermal	1136.1@0.1	433.8@0.1@1000	[203]
BiSbTe$_3$/N-rGO	Nanocomposite	Solvothermal	641.2@0.1	388.7@0.1@80	[204]
In$_2$Te$_3$–TiO$_2$–C	Hierarchical layered	High-energy ball-milling	~450@10	~435@0.5@500	[205]
SIB anode					
NiSe$_2$@BCNNTs	3D nanotubes	Pyrolysis	787@0.1	382.4@2@2000	[206]
SnS$_2$/CNT@rGO	Hierarchical powdery	Solvothermal	528@0.05	301@1@1000	[207]
MoSe$_2$/CN	3D flower-like	Hydrothermal	523.6@0.1	328.7@1@500	[208]
FeS$_2$@TiO$_2$	Core-shell structure	Hydrothermal	222.2@10	374.9@5.0@600	[209]
PNBH-VS$_4$	Hollow microspheres	Hydrothermal	866@0.2	629@0.2@250	[210]
MoS$_2$/CNF	Nanoflower	Hydrothermal	318.2@5.0	314@1@300	[211]
CoS$_2$	Aggregated nanoparticles	Facile-sulfuration process	580@0.1	500@2@500	[212]
Cu$_2$Se	Micro-sized monoclinic	Selenization	264@0.1	~260@1@1000	[213]
MC-NCNF/MoSe$_2$	Multi-channeled	Electrospinning+heat-treatment	285@10	386@0.5@300	[214]
SnS$_2$/EPC	Graphene-like	Hydrothermal	443@0.1	340@2@450	[215]
NiSe$_2$@N-TCF/CNTs	Nanofibers	Electrospinning + pyrolysis	428.0@0.05	392.1@0.2 @1000	[216]
FeS2@N/CNTs@rGO	Urchin-like hierarchitecture	Hydrothermal	578@0.1	570@2@>750	[217]
NSPCFS@CoS$_2$	Nanoparticles	Sulfuration	540.7@4	546.3@1@2095	[218]
Fe$_7$Ni$_3$S$_{11}$/CN	Hollow-spheres	One-pot hydrothermal + post-annealing	567@0.2	477@2@900	[219]

Table 4. *Cont.*

Material	Structure	Preparation Method	Rate Performance [Capacity (mAh g^{-1}) @ Current Density (Ag^{-1})]	Cycle Performance [Capacity (mAh g^{-1}) @ Current Density (Ag^{-1}) @ Cycles]	Ref.
MoS$_2$@RGO	Few-layer nano-roses	One-step solvothermal	513.8@0.1	223.2@0.5@500	[220]
WS$_2$/Ni$_3$S$_2$@NC	Layered-heterostructure	Solvothermal + annealing	329.6@0.1	219.7@0.1@80	[221]
PIB Anode					
CoSSe–C	Porous-shell nanospheres	Sulfo-selenization + calcination	185@5.0	286@1.5@3000	[222]
MoS$_2$/MXene	Layered nanosheets	Hydrothermal	290.7@0.05	145.5@0.2@50	[223]
ZnSe@N-PCNF	Ultrafine nanocrystals	Electrospinning + thermal-treatment	270@0.5	139@2.0@1000	[224]
FeSe$_2$/NC	Nanosheets	Pyrolysis + annealing + carbonizing	203@10	301@1@250	[225]
Co$_{0.85}$Se@NC	Mesoporous structure	Annealing + selenidation	600.9@0.1	114.7@1@250	[226]
ZnSeNP@NHC	Hollow polyhedron	Pyrolysis + selenization	310.5@0.5	~132.9@0.1@1200	[227]
WSe$_2$/N,P-C-2	Ultrathin nanosheets	One-pot calcination	659@0.1	333 @0.1@100	[228]
NPCP@MoSe$_2$	Hollow-interlayered nanosheets	Solvothermal	362@0.1	128@0.5@800	[229]
MoSe$_2$/N–C	Ultra-thin nanosheets	Selenization + calcination	914@0.1	240@0.1@100	[230]
Co$_{0.85}$Se/G	Hollow structure	Hydrothermal	430@0.05	324@0.05@200	[231]
CoSe$_2$@NCF	Flexible core/sheath	Solvothermal	351@0.05	335@0.05@200	[232]
AIB cathode					
CoSe@C	3D nanoparticles	Pyrolysis + annealing	427@1	62.4@5@100	[233]
NC@ZnSe	Dispersed porous	Pyrolysis + selenization	172.7@0.3	70.4@0.5@250	[234]
WS$_2$@NCNFs	Layered nanoplates	Electrospinning + annealing	314.07@0.1	195.81@0.1@100	[235]
MoSe$_2$@C	Sheet nanocomposite	Hydrothermal	294.97@0.1	110.3@0.1@3000	[236]
Ni$_{0.6}$Co$_{0.4}$S@MXene@NC	Layered sheet	Sulfurization + carbonization	481.2@ 0.4	125.2@1@300	[237]
VS$_4$	Nanowire clusters	Amine ions-assisted method	252.51@0.1	129.24@0.4@120	[238]
NiSe$_2$@GO	3D sponge	Selenidation + annealing	~281@0.5	~164@1@250	[239]
Bi$_2$Te$_3$/Sb$_2$Te$_3$	Nanoflakes	Solvothermal	230@1	203@1@300	[240]
Fe-NiSe	Nanoflake	Hydrothermal	304@1	197@1@13.500	[241]
MIB cathode					
1T-VSe$_2$@rGO	Thin-layered nanoparticles	Hydrothermal	235.5@0.05	147.66@0.05@500	[242]

Table 4. *Cont.*

Material	Structure	Preparation Method	Rate Performance [Capacity (mAh g^{-1}) @ Current Density (Ag^{-1})]	Cycle Performance [Capacity (mAh g^{-1}) @ Current Density (Ag^{-1}) @ Cycles]	Ref.
$Cu_{7.2}S_4$	Nanotubes	Microwave-induced selective-etching	314@0.1	59.1@1@1600	[243]
ZIB cathode					
$1T-WS_2$	Nanosheet	Hydrothermal	233.26@0.5	85.11@0.5@1000	[244]
TiS_2	Layered	Hydrothermal	76@1	~53.2@1@500	[245]
HMIB cathode					
$Cu_2S@C/MLIB$	Monodisperse	Sulfurization + carbonization	399.2@0.05	150@0.05@50	[246]
$MoS_2/MLIB$	Flower-like architectures	Solvothermal	220@0.07	160@0.07@65	[247]
$VS_4/MLIB$	Nanodendrites	Solution-phase approach	~300@0.5	110@1@1500	[248]
FeS-CNFs/MLIB	1D network	Electrospinning + thermal treatment	463@0.07	200@0.257@800	[249]
MoS_2&$MoSe_2/MLIB$	Nanosheets	Exfoliation processing	135@0.02&75@0.02	81@0.02@10&82@.02@3	[250]
Co_3S_4-F/MLIB	Particle-like	Solvothermal	779.8@0.1	399.5@0.1@100	[251]
$VS_2/MLIB$	Nanosheets	One-pot solvothermal	~234@0.1	~222@0.1@200	[252]
$TiS_2/SMIB$	Layered structure	As-received	200@1	67.5@20@3000	[253]

Li-Ion

LIBs are a good energy storage technology because of their high performance (capacity, cycling performance, rate capability, and others). However, existing commercially available graphite electrodes have low energy due to their small surface area, deterioration, large volume expansion, low theoretical capacity (372 mAh/g, based on un-lithiated graphite) [254], and low power due to sluggish kinetics [255]. Because of their excellent electroconductivity, rich redox chemistry, multiple valence states, various crystalline morphologies, and high specific capacity, MCs and relevant composites have attracted increasing attention as electrode materials for LIBs in recent years [256,257]. Nanostructures of chalcogenides, such as nanorods, nanowires, nanofibers, nanoflakes, nanocages, flower-like, and hollow spheres of chalcogenides, have all been successfully manufactured and tested as electrode materials in LIBs to date [196,197,199,204,205]. Many studies have recently demonstrated that doping with cations or heteroatoms can improve the lithium storage kinetics of MC electrodes by producing edge/surface defects and local charge polarization, both of which are significant in boosting charge and electron transport [199]. N-doped carbonaceous materials, for example, have substantial chemisorption for poly-sulfides, which can improve cycle performance, while S-doping could improve conductivity due to its more effective reduction and stronger electron donor ability [258].

A self-assembled approach was used to successfully manufacture V_3S_4 nanosheets anchored on an N, S co-coped graphene (VS/NSG) aerogel (Figure 12a) [259]. Decomposition, sulfuration, and N, S co-doping happened during the heat treatment process. The electrochemical performance was significantly improved by the dominant pseudocapacitive contribution (57.78% at 1 mV/s), including rate capacity of 480 and 330 mAh/g at 5 and 10 A/g, respectively (Figure 12b) and stable cyclic performance of 692 mAh/g after 400 cycles at 2 A/g. Because of the conductive network that had been built, this hybrid structure (Figure 12c,d) not only had good electron conductivity but also had a

significant ability to buffer volume growth. Apart from cation doping, the introduction of carbon-based composites of various dimensions, such as 1D, 2D, and 3D nanostructures, can also provide a viable way to design target materials with multifunctional or enhanced properties due to their excellent electronic conductivity and large surface area. For example, Xu et al. [203] described the solvothermal synthesis of a hierarchical g-C_3N_4@WS_2 composite. The g-C_3N_4@WS_2 composite, as synthesized, had a high discharge capacity of 1136.1 mAh/g at 0.1 C and excellent cycling stability of 433.8 mAh/g after 1000 cycles. MC having hierarchical porous architectures have a large number of channels for Li^+ transport, resulting in increased rate capacity [203,205]. Because of their high porosity, crystallinity, inherent modularity, and huge specific surface area, MOFs have recently been widely employed as precursors to manufacture certain derivatives of MCs, which preserve their unique shape and so display outstanding rate capacity.

Na-Ion

SIBs have emerged as one of the most promising alternatives for energy storage due to their high theoretical specific energy density (760 Wh/kg), long cycling life, low cost, low redox potential, and excellent energy storage mechanism [258,260,261]. However, there are significant obstacles that continue to stymie SIB development. Na's huge atomic weight and low standard electrochemical potential may result in explosions, corrosion, and high-power consumption. Second, during cycling, Na metal prefers to accumulate in a dendritic structure and endures a large volume change. Furthermore, high reactivity may lead to electrolyte degradation and battery breaking and reforming, resulting in poor cycle performance [262–264]. Furthermore, because Na^+ has a larger radius (1.02) than Li^+ (0.76), it is more difficult to intercalate/de-intercalate in the crystal lattice, causing severe mechanical stress/strain on the electrodes, resulting in excessive material capacity degradation [265,266]. Searching for appealing materials such as anode/cathode and appropriate electrolytes is the major technique for improving SIB performance. Due to their excellent theoretical gravimetric, thermodynamic stability, remarkable redox reversibility, and high theoretical capacity, conversion reaction-based materials, such as metal oxides/sulfides/selenides, specifically transition MCs, have recently been developed as electrode materials for SIBs. Nanostructure design, doping, and compounding with other materials, similar to LIBs, can provide improved performance because hollow structures can accommodate volume changes during sodiation/desodiation while also providing more surface area and well-defined cavities, which can improve SIB stability [192,267,268].

To combat these challenges, Chen et al. [219] used a simple one-pot hydrothermal approach with post-annealing to create a bimetallic solid solution of $Fe_7Ni_3S_{11}$ nanoparticles confined with nitrogen-doped carbon (CN). Used as an anode in SIBs, the material had a reversible specific capacity of 567 mAh/g at 0.2 A/g and maintained a capacity of 477 mAh/g after 900 cycles at 2 A/g with a capacity retention rate of 90%. Furthermore, Y. Chen et al. [269] created a heterojunction bimetallic sulfide nanosheet SnS_2/FeS_2/rGO composite by introducing FeS_2 to grow synchronously with SnS_2 on rGO in situ (Figure 12e) as an electrode in SIB and produced a capacity of 768.3 mAh/g at 0.1 A/g and 541.2 mAh/g at 1 A/g (see Figure 12f). Chen et al. [206] also used a simple pyrolysis process to create a novel self-supporting $NiSe_2$ composite enclosed in boron carbonitride (BCN) nanotubes ($NiSe_2$@BCNNTs). The as-made $NiSe_2$@BCNNTs anode demonstrated a remarkable reversible Na^+ storage capacity of 787 mAh/g at a current density of 100 mA/g and improved long-term cycling stability of 382.4 mAh/g at 2 A/g after 2000 cycles.

K-Ion

Potassium has a lower reduction potential than lithium and sodium, allowing potassium-ion batteries (KIBs) to operate at greater potentials and hence provide more energy density. However, the development of KIBs has been hampered by the lack of adequate electrode materials, which affect cell capacity and probable overload [270]. Because of their high

theoretical capacities and low cost, metal chalcogenide materials have attracted a lot of attention for usage as anodes in KIBs [271–273].

Yang et al. [274] used a direct vacuum filtration and subsequent reduction process to make flexible Sb_2Se_3 nanorods supported by holey rGO composite membranes (Sb_2Se_3 @h-rGO), where the pre-electrostatic interaction of Sb^{3+} and O^{2-} pushed the formation of Sb–O–C bonds between Sb_2Se_3 nanorods and h-rGO. Free-standing Sb_2Se_3 @h-rGO electrodes showed outstanding cycling stability when used as anodes for KIBs, with a high capacity of 382.8 mAh/g at 100 mA/g after 500 cycles. In order to compensate for the significant volume change of nanocrystals throughout the potassiation and depotassiation processes, hollow carbon nanospheres containing iron telluride nanocrystals ($FeTe_2$-C) are manufactured via easy infiltration and a one-step tellurization procedure (Figure 12g) [275]. The synergistic impact of the heterointerfaced $FeTe_{1.1}$ and metalloid Te produced after one cycle, as well as the yolkshell architecture with uniformly distributed nanocrystals contained in a carbon shell, result in excellent electrochemical characteristics. Even at a high current density of 10 A/g, the $FeTe_2$-C electrode exhibits outstanding long-term cycle performance (171 mAh/g during the 500th cycle at a high current density of 0.5 A/g) and great rate capability (126 mAh/g). Park et al. [222] recently published a new strategy for the synthesis of cobalt sulfoselenide solid solution embedded in the porous shells of hollow carbon nanospheres, in which a porous hollow carbon nanosphere was used as a co-infiltrating matrix to create electrode material with high conductivity and robust stability. CoSSe-C was an outstanding anode for KIBs, with a cycle life of 286 mAh/g for 3000 cycles at 1.5 A/g and a rate capability of 185 mAh/g at 5.0 A/g.

Mg-Ion

MIBs are widely used as a safe, low-cost system with a high charge density, theoretical capabilities, and lower reduction potential (Mg metal can reach 3833 mAh/cm^3) (−2.37 V vs. SHE). Above all, unlike lithium-metal and sodium-metal batteries, magnesium metal batteries can successfully avoid dendrite formation during the cycle, making them safer [276–278]. The rechargeable MIB electrode, on the other hand, has slow kinetics and poor cycle stability due to its high charge density, slow solid-state diffusion rate, and great polarization ability of Mg^{2+} [279,280]. Furthermore, the low specific capacity of the classic carbonate electrolyte is due to a lack of proper active sites for Mg^{2+} intercalation in the lattice, as well as magnesium's ability to rapidly form a dense passivation film. The strong contact between Mg^{2+} and the lattice of the cathode material prevents Mg^{2+} from becoming embedded in the cathode material, lowering the Mg^{2+} diffusion rate.

Exploring innovative and effective materials such as cathodes to achieve high voltage, big capacity, and a long stable cycle is critical for improving MIB electrochemical performance [281]. $Cu_{7.2}S_4$ [243], VS_2 [282], and $MoSe_2$ [283] are considered promising cathode materials for magnesium batteries because they have more active sites, expandable spacing leading to increased active sites and increased diffusion rate, and improve the mobility and desolvation of Mg^{2+} at the electrolyte/electrode interface [284]. Gao et al. [242] employed a simple hydrothermal process to create 1T-VSe_2 nanoparticles that cooperated with reduced graphene oxide (1T-VSe_2@rGO) composite in an APC electrolyte environment, and it was used as the cathode material of the second-generation rechargeable MIB. The 1T-VSe_2@rGO composite cathode material demonstrated outstanding reversible capacity (235.5 mAh/g at 50 mA/g) and long cycle life (62.7% of the initial capacitance is preserved at 50 mA/g after 500 cycles). A 46% initial capacitance rate capability was recorded, equating to a current density of 1000 mA/g.

Al-Ion

Rechargeable aluminum-ion batteries (RAIBs) have emerged as one of the most promising multivalent metal-ion battery types, owing to their low flammability, low cost, and high volumetric energy density (8040 mAh/cm^3) [285]. Despite extensive efforts, RAIBs' electrochemical performance was nevertheless hampered by many difficulties, including

low discharge voltage, poor cycling stability, and electrode disintegration. Alternative cathode materials capable of generating higher energy densities have been the subject of recent research. Transition metal chalcogenides have caught the attention of researchers because of their weak binding strengths between host frameworks, which could lead to more favorable kinetics for aluminum storage, such as high reversible specific capacities of more than 250 mAh/g [191,233,235,241].
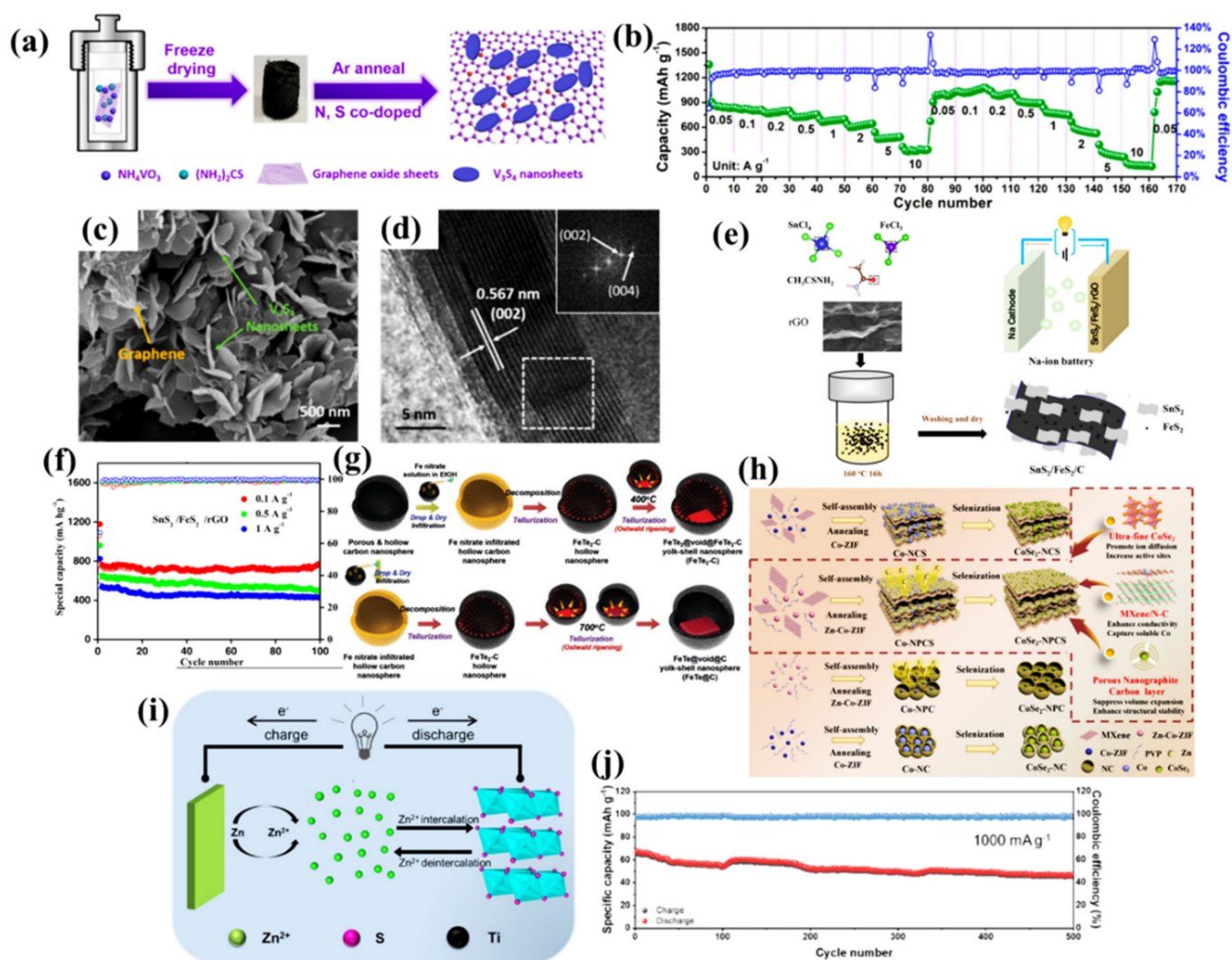

Figure 12. (**a**) A schematic representation of the VS/NSG electrode preparation method. (**b**) the rate capability of the VS/NSG electrode. (**c**) SEM pictures of VS/NSG as prepared. (**d**) In the designated white box of VS/NSG, TEM picture, HRTEM image, and FFT patterns. Adapted from reference [259]. This article is an open access article distributed under the terms and conditions of the Creative Commons Attribution (CC BY) license. (**e**) The $SnS_2/FeS_2/rGO$ composite's synthesis method. (**f**) The $SnS_2/FeS_2/rGO$ composite's cycling performance at 0.1, 0.5, and 1 Ag^{-1}. Adapted with permission [269]. Copyright (2021) American Chemical Society. (**g**) The hollow carbon nanosphere containing the iron telluride nanocrystals and its formation mechanism. Adapted with permission [275]. Copyright (2020) John Wiley and Sons. (**h**) A schematic illustration of the $CoSe_2$-NC, $CoSe_2$-NPC, $CoSe_2$-NPCS, and $CoSe_2$-NCS synthetic stages, respectively. Adapted with permission [286]. Copyright (2021) American Chemical Society. (**i**) A Zn/TiS_2 aqueous battery schematic example. (**j**) Performance at 1000 mA/g in cyclic mode. Adapted with permission [245]. Copyright (2020) American Chemical Society.

RAB's cathodes containing ultrafine $CoSe_2$ particles embedded in nitrogen-doped porous carbon nanosheet (NPCS)/MXene hybrid materials were developed using a spatial isolation technique to solve the associated problems of limited structural stability and poor reaction kinetics [286]. As shown in Figure 12h, the two-dimensional NPCS structures were created via self-assembly of metal frameworks on MXene surfaces. This synthetic technique allowed the researchers to manipulate the particle size of active materials even at high pyrolysis temperatures, allowing them to investigate the impact of size on electrochemical performance. The $CoSe_2$-NPCS electrode delivered a high discharge capacity, outstanding rate capability, and long-term cycling stability, according to spectroscopic examination. Zhang et al. [239] described a simple method for making a novel cathode material for RAIBs out of a standard transition metal chalcogenide $NiSe_2$ with a 3D sponge-structure and graphene oxide (GO) nanosheets decoration (3D $NiSe_2$ sponges@carbon composite). After 250 cycles, the product had a high capacity of 281 mAh/g at 500 mA/g and a better cycling performance of 164 mAh/g at 1000 mA/g.

Zn-Ion (ZIB)

Because of their non-toxicity, natural abundance, low cost, good air stability, high theoretical specific capacity (820 mAh/g), low redox potential (0.76 V vs. SHE), high energy density, and good reversibility in mild aqueous electrolyte, rechargeable zinc ion batteries (ZIBs) are considered one of the most promising. TMD has been examined as a suitable cathode material for reversible storage of zinc ions to improve the performance of ZIBs due to their unique layered architectures [287,288].

Tang et al. [244] revealed for the first time that 1T-WS_2 nanosheets could be a viable cathode choice for rechargeable ZIBs. The as-synthesized WS_2-200 has reversible discharge capacities of 233.26, 206.25, and 179.99 mAh/g at current densities of 50, 100, and 200 mA/g, respectively, thanks to the large interlayer spacing and high conductivity of 1T phase. WS_2-200 has an initial discharge capacity of 85.11 mAh/g even at a high current density of 1000 mA/g. In the work of Wang et al. [245], layered TiS_2 was effectively demonstrated as a lasting host material for neutral aqueous ZIBs with a comparatively low charge voltage of 0.4 V. As shown schematically in Figure 12i, TiS_2 undergoes a reversible (de)intercalation process in conjunction with the valence change of the titanium element during cycling. In a Zn/TiS_2 cell, the TiS_2 material provided a stable capacity of 120 mAh/g at 100 mA/g, a high-rate capability of 76 mAh/g at 1000 mA/g, and strong cycle performance (70% capacity retention after 500 cycles at 1000 mA/g (Figure 12j)). Ex situ X-ray diffraction analysis revealed that the superior electrochemical capabilities are due to the good maintenance of TiS_2 during cycling, in which the Zn^{2+} cations can be easily inserted/extracted into/from the layered structure with only minor structural change.

Hybrid Metal Ion

Mg–Li batteries hybrid (MLIBs), which feature lithiation/delithiation at the cathode and magnesiation/demagnesiation at the anode, have received a lot of attention because they combine the benefits of the Mg anode and Li intercalation cathode with quick kinetics and high reversibility. In Mg–Li batteries, a number of chalcogenides have been effectively produced, including VS_4 [248], VS_2 [252], CuS [289,290], Cu_2S [246], Cu_2Se [291], FeS [249] and MoS_2 [247].

Cai et al. [251] first built an Mg–Li hybrid battery with a spinel Co_3S_4 cathode and an Mg anode. With a discharge voltage platform of 1.10 V vs. Mg^{2+}/Mg and a high energy density of 439.5 Wh/kg at 0.1 A/g, the particle-like Co_3S_4-F provides an initial high discharge capacity of 779.8 mAh/g and retains 399.5 mAh/g in the 100th cycle. The synergistic effect of hierarchical Co_3S_4-F micro/nano particles and the APC-LiCl hybrid electrolyte resulted in the remarkable spinel Co_3S_4-F electrochemical performance during cycling. During the discharge process, the conversion reaction of Co_3S_4-F to metallic Co and sulfide Li_2S contributes to the ultrahigh capacity of the Mg–Li hybrid battery. On the other hand, due to the vast reserves of Na and Mg in the earth's crust, the Na^+/Mg^{2+}

hybrid-ion battery (NMIB) has been provided some thought. A metallic Mg anode, a TiS_2 generated titanium sulfide cathode, and a 1.0 M $NaBH_4$ + 0.1 M $Mg(BH_4)_2$/diglyme hybrid electrolyte were used to create a highly reversible Na^+/Mg^{2+} hybrid-ion battery [253]. With a large discharge capacity (200 mAh/g at 1 C rate), high-rate capability (75 mAh/g at 20 C rate), and long cycle life, the battery demonstrated outstanding electrochemical performance (90% capacity retention after 3000 cycles).

3.2.2. Applications of Chalcogenides in Metal–Sulfur Batteries
Li–S Batteries

Because of the vast reserves, low cost, and environmental friendliness of the S cathode material, as well as the high theoretical energy density (2567 Wh/kg) and specific capacity (1675 mAh/g), LSBs have become a promising contender for next-generation energy storage devices. However, ordinary LSBs, which include the S cathode, metallic Li anode, separator, and electrolyte, still have many flaws that make them unsuitable for practical applications [292,293]. There are several issues with the S cathode, including low conductivity of S and its discharge products (Li_2S), dissolution of lithium polysulfides followed by severe shuttle effects, and severe volume change of the S electrode on lithiation, all of which result in poorer utilization of S, self-discharging, lower Coulombic efficiency, and weaker cycle stability [294,295]. Various approaches have been reported to solve these difficulties, including combining sulfur with a range of conductive materials, optimizing the organic electrolyte, and integrating multifunctional separators or interlayers. Meanwhile, the most effective way is to investigate acceptable electrode materials with high conductivity and stability, as well as new electrolytes [296,297].

Because of their low Li/Li^+ lithiation voltages, significant chemical interaction with sulfur-containing species, and good conductivity, TMC materials have proven to be promising. Furthermore, nanostructure design and compounding with other materials can improve the electrode's performance. The unique nanostructure (nanotubes, core-shell, porous, yolk-shell, and hollow morphologies) can provide various active adsorption sites to fix S particles and polysulfide, allowing the stability to be maintained even further. The use of conductive materials on the cathode, such as metal oxides/sulfides, carbon materials, and conductive polymers, can improve electroconductivity, provide more active sites, prevent polysulfide dissolution, and lower interface resistance [297,298]. The electrochemical performance of composites is proved to be dependent on S dispersion, and MS materials can operate as S carriers for LSBs due to their superior conductivity, which can provide strong chemical adsorptions with polysulfides and prevent the shuttle process [299].

Jin et al. [300], for example, realized a strong sulfur limitation to eliminate polysulfide shuttling in the nanostructure of carbon-coated metal sulfides instead of pure sulfur cathodes. Figure 13a displays nanoparticles with a carbon shell and an iron disulfide core (FeS_2@C) that were made using the plasma evaporation process and then sulfurized. During the lithiation reaction, the FeS bonds in FeS_2 chemically bind the sulfur atoms, while the carbon shell physically limits sulfur loss within the enclosed structure. After 300 cycles, the FeS_2@C cathode delivers a steady specific capacity of 862 mAh/g due to the outstanding dual constraint of S (Figure 13b). Furthermore, by etching and subsequently selenizing layered double hydroxide (Figure 13c–e), Xu et al. [301] created $CoSe_2$ porous hollow flowers ($CoSe_2$-PHF), which combined the strong catalytic activity of transition metal compounds with the high electrical conductivity of selenium. The $CoSe_2$-PHF produced may effectively speed up the catalytic conversion of LiPSs, accelerate electron transport, and increase active sulfur usage during the charge–discharge process. As a result, the LSBs with $CoSe_2$- PHF/S-based cathodes had a reversible specific capacity of 955.8 mAh/g at 0.1 C and 766 mAh/g at 0.5 C, as well as a remarkably low-capacity decay rate of 0.070% per cycle within 400 cycles at 1 C (Figure 13f,g). The specific capacity of 542.9 mAh/g may be maintained even at a high rate of 3 C.
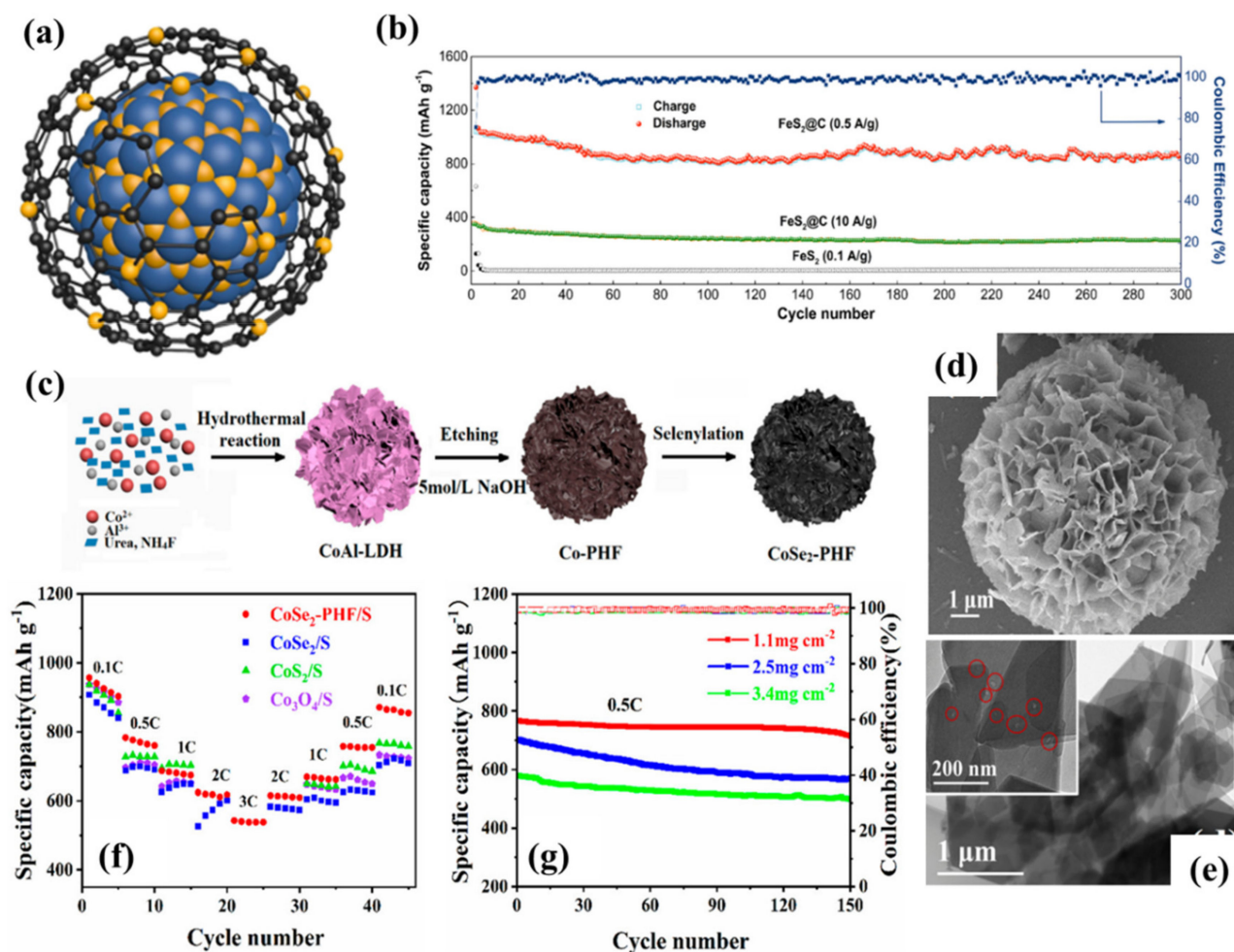
Figure 13. (**a**) A single FeS$_2$@C nanoparticle is depicted; [Fe] atoms are represented by light-blue balls, [S] atoms are represented by light-yellow balls, and [C] atoms are represented by black balls. (**b**) Cycling performance of FeS$_2$@C and FeS$_2$ electrodes at various current densities between 0.01 and 3.00 V. Adapted with permission [300]. Copyright (2020) American Chemical Society. (**c**) A diagram of the CoSe$_2$-PHF production process. (**d**) CoSe$_2$-PHF SEM and (**e**) CoSe$_2$-PHF TEM. (**f**) At various current rates, the rate performance of CoSe$_2$-PHF/S, CoSe$_2$/S, CoS$_2$/S, and Co$_3$O$_4$/S based electrodes, (**g**) CoSe$_2$-PHF/S specific capacity at 0.5 C with various sulfur loadings. Adapted from reference [301]. This article is an open access article distributed under the terms and conditions of the Creative Commons Attribution (CC BY) license.

Na-S Batteries

Because of the natural abundance and low toxicity of sodium and sulfur, as well as a two-electron transfer per sulfur atom, which delivers six times the energy density of conventional Li-ion batteries, sodium–sulfur batteries (SSB) have emerged as an appealing choice for large-scale energy storage applications [302–305]. The development of SSB is hampered by the dissolution of intermediate sodium polysulfides. Short-chain sulfur (S$_{24}$) loading is one promising strategy for avoiding this problem, as it may prevent the formation of soluble polysulfides during the sodiation process. In addition to the creation of traditional carbon hosts, the incorporation of sulfiphilic sites into composite hosts has garnered some interest. It has long been known that polar metal or sulfide materials, such as Fe/Ni/Cu clusters, Co, and NiS$_2$, can provide strong polar-polar interactions for polysulfide immobilization, preventing polysulfide diffusion via a chemical catalytic effect and thus speeding up conversion kinetics from polysulfides to Na sulfides [296,306–309].

Using the synergistic catalytic effect of CoS_2 and the suitable hole size, F. Xiao et al. [309] reported a new approach for generating short-chain sulfur in bigger pores (>0.5 nm) (Figure 14a–d). They estimated that CoS_2 could act as a catalyst to weaken the SS bond in the S_8 ring structure, allowing for the synthesis of short-chain sulfur molecules based on density functional theory simulations. This prevents the formation of soluble polysulfides and provides the composite materials used in SSB with better electrochemical characteristics. Figure 14e,f demonstrates the optimized CoS_2/N-doped carbon/S electrode's electrochemical performance, which includes high reversible specific capacities of 488 mAh/g after 100 cycles at 0.1 A/g and 403 mAh/g after 1000 cycles at 1 A/g, as well as improved rate performance of 262 mAh/g at 5.0 A/g.
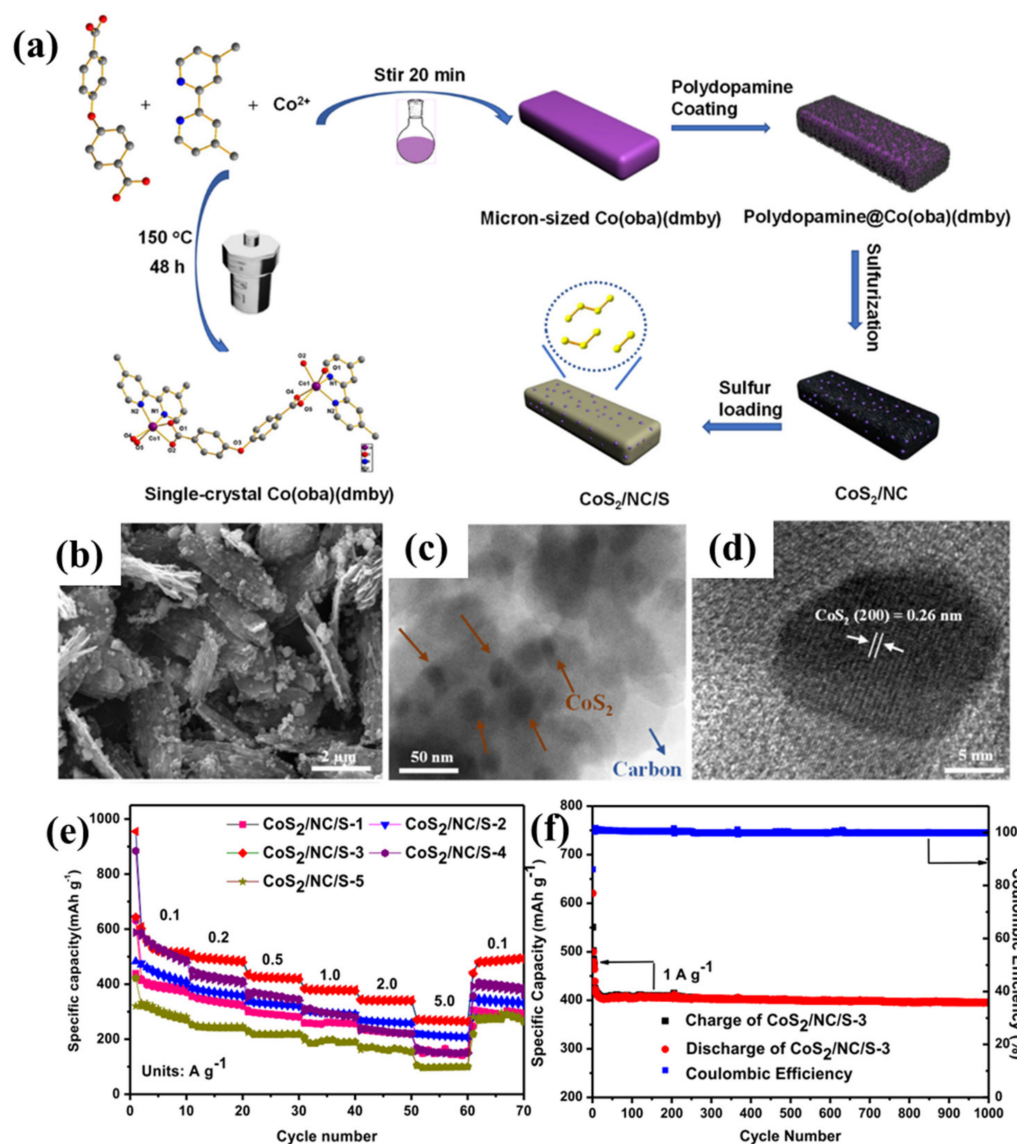
Figure 14. (**a**) Schematics of the CoS_2/NC/S composite fabrication stages. (**b**) SEM picture of the composite CoS_2/NC. (**c**) TEM pictures of the CoS_2/NC composite, with red and blue arrows indicating the locations of CoS_2 nanocrystals and the surrounding carbon matrix, respectively. (**d**) HRTEM picture of a single CoS_2 nanocrystal embedded in a CoS_2/NC composite. (**e**) CoS_2/NC/S-x electrode rate performance. (**f**) 1 A/g long-term cycling of the CoS_2/NC/S-3 electrode. Adapted with permission [309]. Copyright (2021) American Chemical Society.

Mg–S Batteries

The development of rechargeable Mg–S batteries is becoming a more appealing choice in recent times than current Li–S batteries owing to the low cost. Developing high-energy-density Mg–S batteries, however, is fraught with difficulties. To begin with, sulfur's inherent electrical and ionic insulating properties necessitate the use of a large number of conductive additives throughout the electrode preparation process. During cycling, magnesium polysulfide (MgPS) intermediates and solid MgS deposition and decomposition are involved, which is a more complex multi-electron solid-liquid-solid conversion than in Li–S batteries [310]. The shuttling phenomenon happens when soluble polysulfides are produced, leading to capacity loss, Coulombic efficiency decline, and anode corrosion. On the other hand, the bivalent Mg ion's large ionic size and slow diffusion capabilities will further impede the reaction kinetics [311]. In reversible Mg–S batteries, then, to promote cathode reaction kinetics and achieve fast Mg ion conduction and diffusion is critical [312,313]. To tackle this challenge, Zhao et al. [314] presented a Co_3S_4@MXene heterostructure as a sulfur host for reversible Mg–S batteries. The chemical interaction between the decorated Co_3S_4 nanocrystals host and polysulfide intermediates could well absorb and catalyze the polysulfide conversion, thus improving the electrochemical redox kinetics, according to XPS measurements and DFT calculations. Meanwhile, the MXene matrix has the potential to dramatically enhance Mg ion transport dynamics. As a result, the produced Mg–S batteries using Co_3S_4@MXene-S as the cathode material were able to display high sulfur utilization with a specific capacity of 1220 mAh/g and a capacity of 528 mAh/g after 100 cycles, as well as a reasonable rate performance even at 2 C. The innovative cathode design for reversible high-energy Mg–S batteries was revealed in this study.

3.2.3. Applications of Chalcogenides in Metal–Air Batteries

Because of its high energy density and environmental friendliness, rechargeable metal–air batteries have recently piqued researchers' curiosity. Metal–Air batteries, among the several types of batteries, have received a lot of attention in recent years due to their impressive specific energies. Metal–Air batteries, with an abundant supply of oxygen from the atmosphere, may theoretically be lighter, cheaper, and last longer than traditional batteries.

Li–Air

Due to its high theoretical energy density, rechargeable $Li–O_2$ batteries (LOBs) have gained increasing interest and therefore been recognized as one of the potential prospects for electrochemical power sources [315,316]. Unfortunately, several technological challenges remain, including poor capacity, short cycle life, and low coulombic efficiency, which are mostly caused by the slow reaction kinetics and side reactions of the O_2 cathode catalyst [317–319]. As a result, developing effective cathode catalyst materials is critical. By using extremely active catalysts, researchers are currently working to improve the efficiency and selectivity of the process that takes place in the O_2 cathode. Although Pt, Ru, Pd, Au, and their oxides have good catalytic properties, their high costs prevent them from being used in large-scale commercial applications. Particularly, transition metal chalcogenides and their composites have therefore gained popularity for oxygen reduction reaction (ORR) and oxygen evolution reaction (OER) [320–324] due to their low cost, higher conductivity, and high intrinsic reactivities.

CoS_2 nanocages produced from ZIF-67 and interconnected carbon nanotubes (CoS_2/CNTs) were recently developed and employed in the manufacturing of air electrodes for LiO_2 batteries (Figure 15a–d) [325]. The reversible capacity was 2398.9 mAh/g, which is 90% of the discharge capacity. When the cycling capacity was limited to 500 mAh/g, the battery maintained cycling stability for 52 cycles while keeping the cutoff potential above 2.0 V. CNTs are used as channels for fast electron transfer, which compensates for CoS_2's weak conductivity. Additionally, the porous CoS_2 nanocages may provide abundant active sites for an ORR and an OER, facilitating O_2 diffusion and electrolyte infiltration.

Li et al. [326] also described a method for causing $CoSe_2$ to transition from the cubic to the orthorhombic phase by doping it with phosphorus (Figure 15e). Because phosphorus has a lower electronegativity than selenium, it is useful for altering the number of d electrons on the Co cation and so contributes significantly to structural phase transition and electrocatalytic activity. As a result, the LiO_2 battery with the phosphorus-doped orthogonal phase $CoSe_2$ (o-$CoSe_2$|P) electrode shows outstanding rate capability and cyclability (Figure 15f).
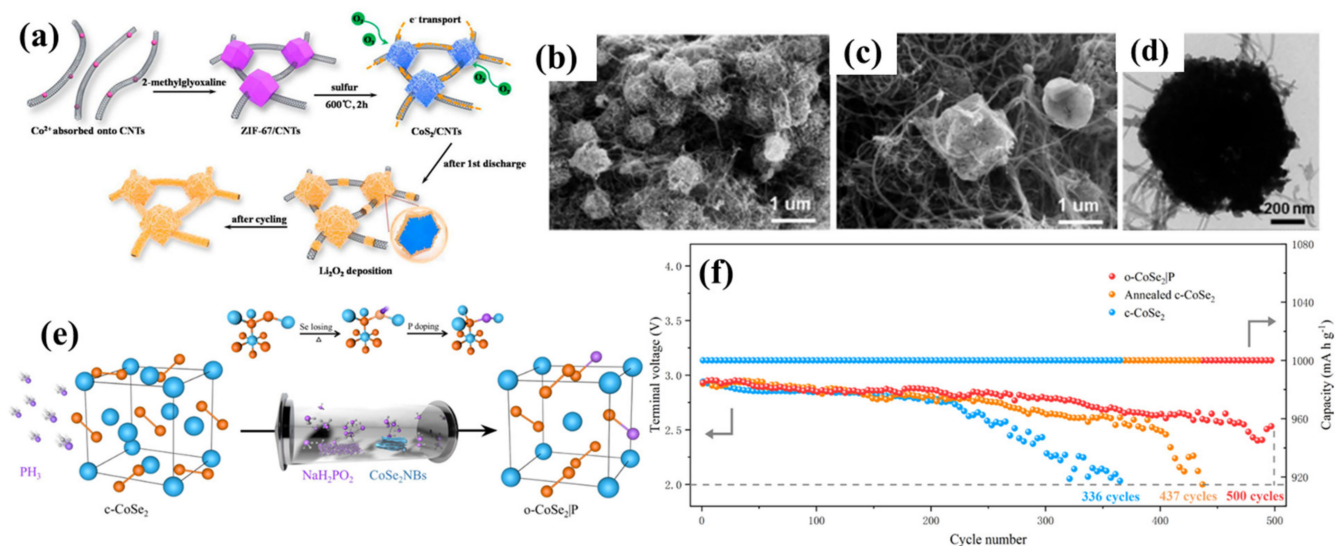
Figure 15. (**a**) Illustration of the CoS_2/CNTs composite fabrication technique. (**b**,**c**) SEM pictures of CoS_2/CNTs (**d**) CoS_2/CNT TEM images. Adapted with permission [325]. Copyright (2020) American Chemical Society. (**e**) The synthesis of o-$CoSe_2$|P. P-doped induction of $CoSe_2$ in the cubic phase into $CoSe_2$ in the orthogonal phase flow diagram. Co, P, and Se atoms are represented by blue, purple, and orange spheres, respectively. (**f**) Cycling performance of LiO_2 batteries based on o-$CoSe_2$|P, annealed c-$CoSe_2$, and c-$CoSe_2$ with a limited capacity of 1000 mAh/g at a current density of 50 mA/g at a current density of 50 mA/g at a current density of 50 mA/g. Adapted with permission [326]. Copyright (2020) American Chemical Society.

Zn–Air

Because of its low cost, great safety, and ultra-high theoretical energy density (1086 Wh/kg), zinc–air batteries (ZABs) are one of the most promising clean energy technologies for meeting the next generation green energy demand [327,328]. Nonetheless, the sluggish kinetics of the processes involved in these devices, particularly the hydrogen evolution reaction (HER), OER, and ORR [329,330], significantly limit the devices' work efficiency. As a result, low-cost catalysts with high activity and endurance are critical for the development of effective rechargeable zinc–air batteries. The most effective electrocatalysts for these processes are currently noble metal Pt, Ir, and Ru-based catalysts and alloys, which are expensive [331,332]. Chalcogenide-based catalysts [333] have piqued interest as cost-effective, high-efficiency, diverse composition, customizable electronic structure, unique redox characteristics, robust durability, and many active site alternatives for a variety of catalytic reactions. Transition metal sulfides (TMSs), for example, have drawn a lot of interest because of their high conductivity, ease of synthesis, and high activity [334].

Liu et al. [335], for example, used a metal-organic framework as a precursor to creating a CoS_2@MoS_2@NiS_2 nano polyhedron with a double-shelled structure that exhibited high catalytic activity for HER, OER, and ORR. Low overpotentials of 156 and 200 mV were attained for HER and OER, respectively, with a current density of 10 mA/cm^2, an ORR half-wave potential of 0.80 V, and a power density of 80.28 mW/cm^2 in Zn–air battery. Hybrid materials made of bimetallic (Co and Fe) sulfide (Co_8FeS_8) nanoparticles supported on N, S-doped carbon microparticles can serve as dual-function oxygen electrocatalysts, according

to Chen and coworkers [336]. The materials are made by pyrolyzing silica-protected Fe- and Co-modified S-containing polyphthalocyanine at various temperatures (Figure 16a–e). The materials were provided with the names (Fe,Co)SPPc-T-sp, where T stands for pyrolysis temperature, and sp stands for silica protection. Among them, the material synthesized at 900 °C, denoted (Fe,Co)SPPc-900- sp, exhibits excellent electrocatalytic activities in an alkaline solution for both the ORR and the OER, with a half-wave potential ($E_{1/2}$) of 0.830 V vs. RHE and a current density of 10 mA/cm^2 at an overpotential (η_{10})of 353 mV. Figure 16f shows an alkaline Zn–air battery with (Fe,Co)SPPc-900- sp as an air electrode that had a high peak power density of 158.6 mW/cm^2 (Figure 16g) and excellent charge–discharge cycling stability (for over 50 h), demonstrating superior catalytic performance over the corresponding battery with Pt/C and RuO$_2$ electrocatalysts (Figure 16h).
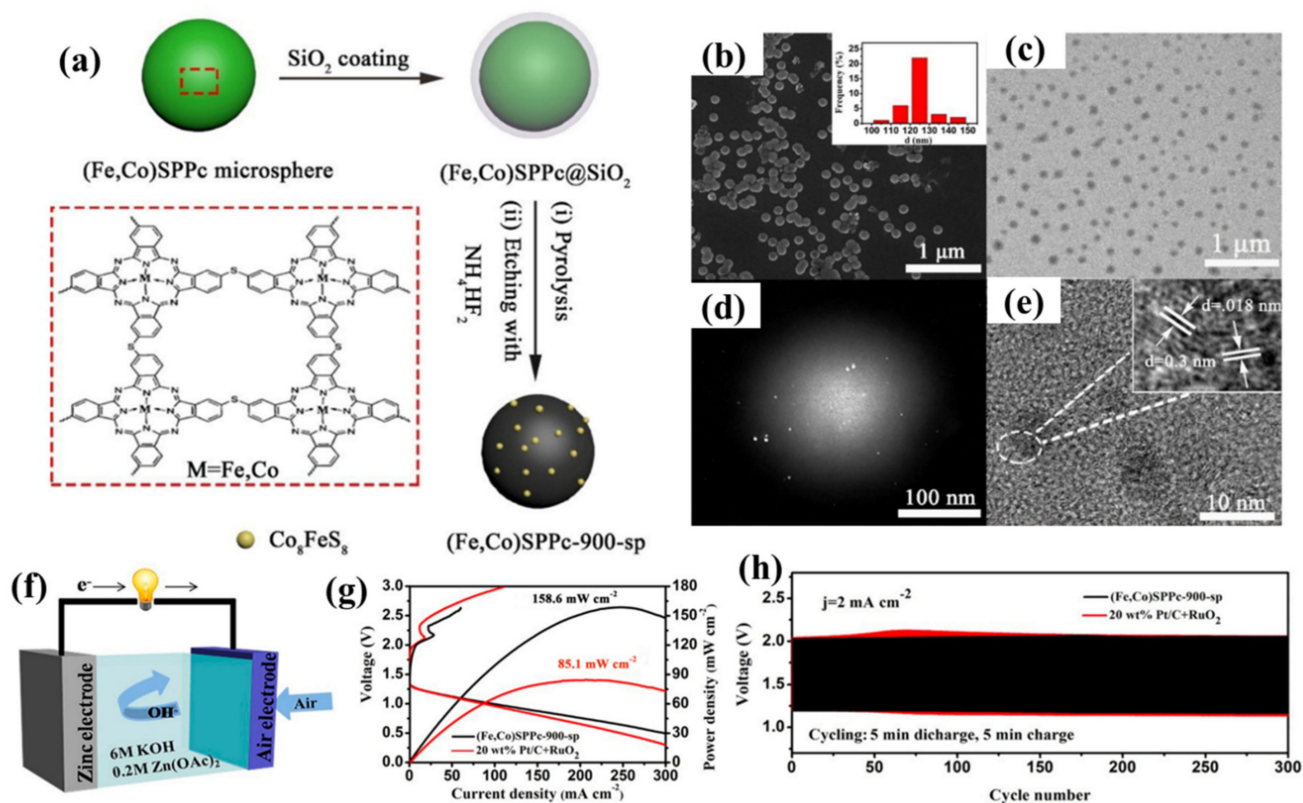
Figure 16. (**a**) Synthetic technique for nanoporous (Fe,Co)SPPc-900-sp and other (Fe,Co)SPPc-T-sp and control materials. (**b**) SEM picture of (Fe,Co)SPPc-900-sp, demonstrating particle size dispersion in the inset. (Fe,Co)SPPc-900-sp (**c**) TEM image, (**d**) HAADF-STEM image, and (**e**) HRTEM image (**f**) Schematic representation of a typical aqueous Zn–air battery with air electrodes made from the electrocatalysts researched here. (**g**) Charge–Discharge curves and power density of Zn–air batteries with air electrodes made up of (Fe,Co)SPPc-900-sp and Pt/C+RuO$_2$ electrocatalysts. (**h**) Plots of galvanostatic charge–discharge at 2 mA/cm^2 current density. Adapted with permission [336]. Copyright (2020) American Chemical Society.

Wang et al. [337] described a simple method for making a new MnS$_x$O$_{2x}$/MnCo$_2$S$_4$ heterostructured electrocatalyst. Controlling the S–O atomic ratio on the surface of MnS$_x$O$_{2x}$ fine-tuned the density and configuration of the active centers. With an overpotential of 367 mV @ 50 mA/cm^2 in 1.0 M KOH, the optimized MnS$_{0.10}$O$_{1.90}$/MnCo$_2$S$_4$ sample had outstanding oxygen evolution reaction performance. More remarkably, the overpotential at 10 mA/cm^2 in 0.2 M phosphate buffer solution was just 414 mV, with cycle efficiency declining by only 3.8% at 10 mA/cm^2 after 140 h. Li et al. [338] created a 3D ordered macroporous N-doped trimetal sulfides (3DOM N-Co$_{0.8}$Fe$_{0.1}$Ni$_{0.1}$S$_x$) bifunctional catalyst. The porous 3DOM structure provided several routes for bulk movement and catalytic active

site exposure. This 3DOM catalyst demonstrates high bifunctional catalytic activity, with an ORR half-wave potential of 0.80 V (versus RHE) and low OER overpotential of 370 mV at a current density of 10 mA/cm^2 due to the synergistic action of trimetallic sulfide and N-doped carbon layer. At 10 mA/cm^2, the zinc–air battery with 3DOM N-$Co_{0.8}Fe_{0.1}Ni_{0.1}S_x$ has a stable cyclability and a lifetime of over 200 h.

Al–Air

Many appealing features of an alkaline electrolyte aluminum–air (Al–air) battery include abundant resources, nontoxicity, zero-emission, easy recycling of $Al(OH)_3$ by-product, theoretical specific energy of 8135 Wh/kg, and fast replacement of Al electrode, all of which are ideal for electric vehicles [339]. However, due to the sluggish kinetics of the ORR and/or OER for the cathodic process, numerous major difficulties have been met for Al–air batteries, including reaction instability and high polarization. The development of highly efficient, low-cost, and long-lasting electrocatalysts or air electrodes for both alkaline and non-aqueous conditions is a vital component in putting this technology into practice [340].

In that regard, Cao et al. [341] used a one-step electrospinning method combined with a pyrolytic process to make graphitic layers covered with Co_9S_8 nanoparticles trapped inside N,S dual-doped hierarchical porous carbon nanofibers. The obtained Co_9S_8@G/NS-PCNFs exhibited ORR activity (E_{onset} = 0.93 V vs. RHE, $E_{1/2}$ = 0.82 V vs. RHE) comparable to those of state-of-the-art Pt/C (E_{onset} = 0.98 V vs. RHE, $E_{1/2}$ = 0.84 V vs. RHE) in alkaline electrolyte Al–air batteries. Specific capacity of 2812 mAh/g at a current density of 35 mA/cm^2, a high open-circuit voltage of 1.74 V, and a peak power density of 79.04 mW/cm^2 were achieved, demonstrating good electrochemical capabilities.

3.3. Applications of Chalcogenides in Supercapacitors

Supercapacitors (SCs), because of their high power density, long cycling life, quick charging-discharging rate, and environmental safety, are thought to be one of the most popular technologies for energy storage. However, charge accumulation is limited on the electrode surface, which limits the energy density of SCs in practical engineering applications. As a result, various research projects have been launched to obtain high energy density while maintaining its power density and cycling stability. The innovation of hybrid supercapacitors (HSCs), which consists of negative and positive electrodes with charge storage operations based on capacitive and faradaic processes, respectively, has emerged in recent decades. Nonetheless, selecting appropriate negative and positive electroactive material that can work well in a variety of potential window ranges in the same electrolyte is a major problem in the production of HSCs. One of the most significant factors for the design architecture and manufacture of the negative and positive electrodes for HSCs is the above-mentioned component. Carbon-based materials were formerly thought to be a potential negative electroactive material for HSCs because of their extended cycle life, large specific surface area (SSA), good chemical stability, strong electronic conductivity, and enhanced porosity. Various kinds of carbon nanostructural architectures, such as graphene, activated carbon (AC), and carbon nanotubes (CNTs), have been employed as negative electrode materials in the recent past for aqueous alkaline-based HSCs.

Due to the abundance of carbon-based resources on the planet, ease of processing, and environmental friendliness, AC is a viable option. Metal chalcogenides which have faradaic and battery-like characteristics, on the other hand, have been widely used as the positive electrode material in HSCs in recent years. Because metal chalcogenides have superb reversible redox mechanisms on the bulk or surface of the electrode materials, they have a higher energy density as compared to the various commercialized carbon-based electrode materials [342]. In addition, the abundant redox-active sites, variable oxidation states, decreased bandgap, and significant electrical conductivity of transition metal chalcogenides (TMCs) are thought to be favorable battery types and SC electrode material [343]. They also allow for fast ion transport kinetic as a result of decreased diffusion path and low

resistance at the electrode/electrolyte interface. This helps to increase the electrochemical properties in terms of rate capability, high capacity, and long cycle stability. The extended metallic characteristic of chalcogenides, as opposed to metal oxides/hydroxides, is largely responsible for their superior properties. This section focuses on various applications of chalcogenides in pseudocapacitors and HSCs.

3.3.1. Applications of Chalcogenides in Pseudocapacitors

Because electrochemical capacitors, particularly pseudocapacitors, have greater specific capacitances than EDLCs, they are promising for energy storage systems. Among various nanomaterial electrodes, such as carbon, transition metal oxides and/or hydroxides, and conducting polymers, TMCs (e.g., sulfides, tellurides, selenides, etc.) have been identified as one class of promising electrode materials for pseudocapacitors, due to their rich electroactive sites and electrical conductivity.

Metal Tellurides

Research on transition metal tellurides (TMTes) for electrochemical energy storage is still in its infancy. However, Te has a higher electrical conductivity, lower electronegativity, and a bigger atomic size than that of S and Se, allowing for more electrolyte ions to be accommodated with better diffusion kinetics. Tellurides are more distinctive among the chalcogenides because their chemical and physical properties are intermediate between metal and non-metal, resulting in products that have good electrochemical properties as well as high conductivity. Kumbhar et al. [344] described the pseudocapacitive performance of samarium telluride (Sm_2Te_3) thin films obtained via single-stage chemical synthesis. In a $LiClO_4$-propylene carbonate electrolyte, cyclic voltammetry indicated a specific capacitance of 207 F/g as well as a power density of 14.18 kW/kg. In recent years, the production of multilayer transition metal dichalcogenide nanocrystals with good energy conversion and storage capabilities has been thoroughly described. However, due to Te's metallic nature, chemical synthesis of homogeneous, well-defined $MoTe_2$ nanoarchitectures remains a problem, particularly for achieving metasTable 1 T'-$MoTe_2$. For this reason, Liu et al. [345] synthesized ultrathin 1T'-$MoTe_2$ nanosheets using a colloidal chemical approach. Changing the Mo precursors and reaction environment can influence the morphologies of 1T'-$MoTe_2$, with CO playing a key role in determining the characteristic of the nanosheet. The few-layer 1T'-$MoTe_2$ nanosheets, after optimization, were employed as an efficient SC electrode, with a specific capacitance of 1393 F/g at a current density of 1 A/g. Using a simple one-step solvothermal technique with no surfactants, highly disseminated CoTe electrode material was effectively generated [346]. A solvothermal approach employing ethylene glycol as a solvent produced a regular nanowire-based CoTe, as opposed to the traditional hydrothermally generated irregularly-shaped CoTe. At a current density of 1 A/g, the produced CoTe nanowire electrode delivered a very high specific capacitance (643.6 F/g) and outstanding cyclic stability, even after 5000 cycles at a high current density (5 A/g), demonstrating exceptional rate performance.

Metal Selenides

In the electrochemical energy-storage industry, highly conductive metal selenides are gaining traction as viable electrode materials in pseudocapacitors. However, phase-pure-bimetallic selenides are difficult to come by, and their charge-storage methods remain a mystery. Metal selenides have proven to be a new family of faradic electrode materials that have been used in supercapacitors recently. In comparison to metal sulfides, no significant study on metal selenides has been documented in the TMC class of electrode materials. Selenium is the group VIA closest neighbor, with the same valence electrons and oxidation state as sulfur. As a result, the electrochemical and chemical properties of sulfides and selenides are nearly identical. Because of their superior electronic conductivity, superb redox chemistry, and better mechanical and thermal stability, metal selenides can be useful in supercapacitors [347]. Due to the high electrical conductivities, superior life

cycle, pseudocapacitive behaviors, large SSA, and cost efficiency, silver nanostructured materials and their compounds, as well as silver-doped materials, have been employed as pseudocapacitor electrode materials. A well-controlled deposition of a pseudocapacitive thin-film nanostructured silver selenide (Ag_2Se) on a stainless steel substrate was prepared recently by using a simple, low-cost, room temperature, and scalable successive ionic layer adsorption and reaction technique and employed as an electrode material for supercapacitors [348]. After 2000 charge–discharge cycles, the Ag_2Se electrode retains 85.10% of its capacitive performance when used in a pseudocapacitor. This performance could be attributed to the surface-induced capacitive and diffusion-controlled reactions at the electrode/electrolyte interface.

A solvothermal approach was adopted to fabricate monodispersed hollow $NiCoSe_2$ (H-$NiCoSe_2$) for SC application, as shown schematically in Figure 17a [349]. The synthesized composite material displayed hollow sub-microsphere structures (Figure 17b), which contributed to enhanced ionic mobility. After about 100 CV cycles, it showed a competitive pseudocapacitance of 750 F/g at a current density of 3 A/g as compared to the other electrode materials (Figure 17c). The inherent energy-storage process of the as-synthesized H-$NiCoSe_2$ is convincingly revealed by the systematic physicochemical or electrochemical properties of the device, which accounted for the superb pseudocapacitance after cycling. An array of $Co_{0.85}Se$ hollow nanowires (HNW) was also used to make an SC electrode, which was made utilizing wet chemical hydrothermal selenization of originally formed nanowires of cobalt hydroxyl carbonate on conductive CFP (carbon fiber paper) (Figure 17d) [350]. Scanning electron microscopy revealed the dense self-organized structures of the $Co_{0.85}Se$ HNWs, which helped in facilitating ionic transport, as shown in Figure 17e. The as-synthesized electrode showed a strong pseudocapacitive characteristic (Figure 17f), as well as high capacitance retention and endurance.
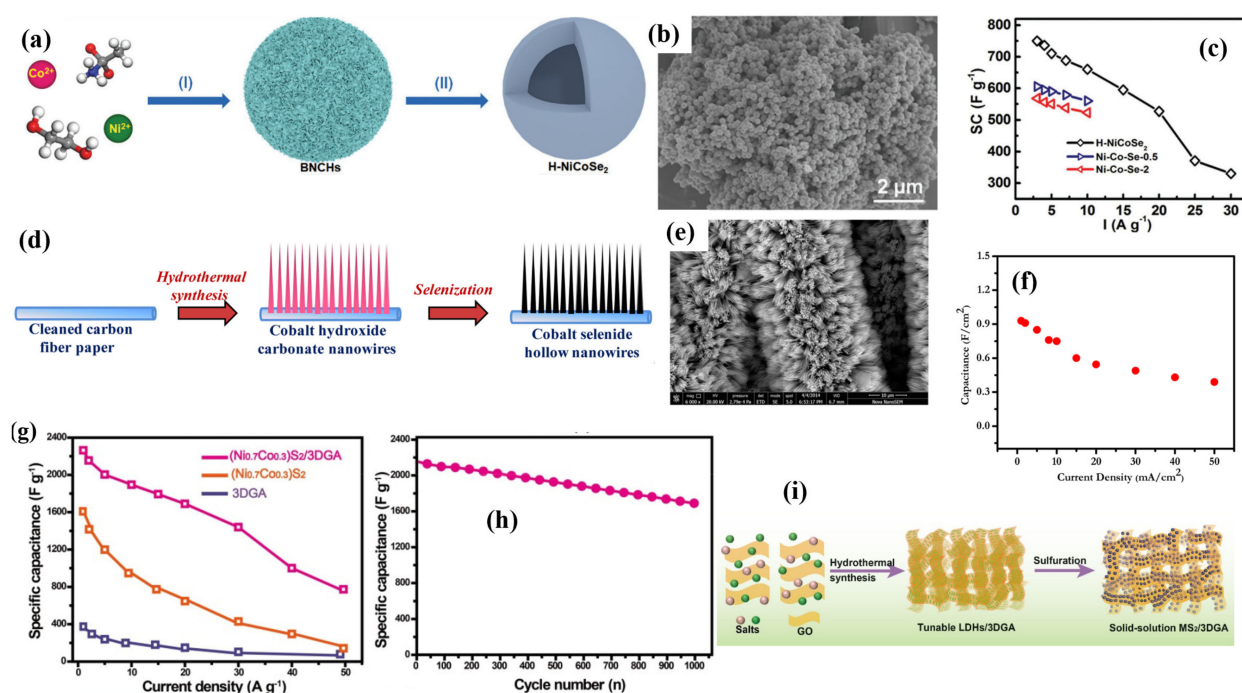
Figure 17. (**a**) Schematic preparation for the synthesis, (**b**) FESEM image of the H-NiCoSe₂ sub-microspheres. (**c**) Capacitance comparison vs. current density for different electrodes. Adapted with permission [349]. Copyright (2018) John Wiley and Sons. (**d**) Schematic illustration of the formation, (**e**) SEM image, and (**f**) The capacitance of the Co$_{0.85}$Se HNWs. Adapted with permission [350]. Copyright (2014) American Chemical Society. (**g**) Capacitance comparison of different fabricated electrodes. (**h**) Specific capacitance as a function of cycle number (**i**) Schematics of the preparation process for the solid-solution MS₂/3DGA composites. Adapted with permission [351]. Copyright (2017) American Chemical Society.

Metal Sulfides

Due to the benefits of high theoretical capacitance, transition metal sulfides (TMSs) are projected to meet the high energy storage requirements of SCs. Simultaneously, they have a good electronic conductivity, which is mostly due to the lower electronegativity of sulfur compared to oxygen. Many researchers have developed a range of sulfides with various phase and metal structures, such as NiS, NiS₂, Ni₃S₂, Co₉S₈, MoS₂, and CoS, etc., in recent years. The introduction of vacancies/defects engineering, for example, can greatly increase the performance of TMSs. TMSs have been proposed as potential electrode materials for electrochemical pseudocapacitors. However, they are usually made of mixed composites or commercially stoichiometric TMSs (for example, NiCo₂S₄ and Ni₂CoS₄). The composites materials offer to enhance electrochemical performance. Several strategies have been used to improve the electrochemical performance of bi-metallic sulfides based on the above concerns. Through the sulfuration of NiCo-layer double hydroxide (NiCo-LDH) as a precursor on 3D graphene aerogel, a solid-solution sulfide composite electrode material (Ni$_{0.7}$Co$_{0.3}$)S₂/3DGA was prepared, as shown in Figure 17i [351]. The as-synthesized electrode delivered a capacitance of 2165 F/g at 1 A/g and retained about 78.5% of the initial capacitance after 1000 cycles for pseudocapacitors, according to the electrochemical studies shown in Figure 17g,h. These findings suggest that engineering LDH precursors can be used to generate a variety of TMSs for energy storage due to their ease of ionic transport.

Recently, an easy and direct-one-step chemical bath deposition technique was used to create binder-free nickel sulfide (NiS) nanostructures on commercial Ni-foam [352]. The electrochemical properties of the device were studied for pseudocapacitor performance. The porous architectures aided fast ionic/charge movement in the electrodes, which is advantageous for the development of electrochemical SCs. The as-synthesized

device delivered a high pseudocapacitance (1442 F/g at 1.1 A/g), as well as good rate capability and a high specific energy and power density. As a result, the produced NiS electrodes are a suitable candidate for energy storage, as they provide faster ion/electron transport, a large SSA, higher electrical conductivity, and strong structural stability. For high-performance pseudocapacitors, Hong et al. [353] fabricated a binder-free electrode consisting of nanowire arrays of Co_3O_4@Co-NiS core/shell with varying Ni/Co ratios. The as-fabricated electrode provided the structural properties required for efficient active material use. This hierarchical electrode delivered a high specific capacitance of 1844 F/g at 5 mA/cm^2 due to the superiority of the well-ordered structure, making it a potential material to be used in electrochemical energy storage. Liu et al. [62] have recently synthesized a metal sulfide porous composite material with exceptional pseudocapacitance qualities. FeCo-MIL-88 was first synthesized using a solvothermal technique. The FeCo-MIL-88 was then treated at high temperature with thiourea, nickel chloride, and sodium sulfide to produce $Fe_xCo_yS_z$-MIL-88@NimSn. Finally, $Fe_{.92}Co_{.08}S$@NiS/NiO composite was formed by calcining $Fe_xCo_yS_z$-MIL-88@NimSn in an N_2 atmosphere. The lamellar architecture created a huge gap for efficient electron transmission, and the composite exhibited notable electrochemical capabilities. This featured a high specific capacitance of 1868 F/g at 1 A/g and a high level of cycling stability even after 5000 cycles.

3.3.2. Applications of Chalcogenides in Hybrid Capacitors

In order to overcome the limitations of rechargeable batteries and conventional SCs, transition metal hybrid capacitors have been advanced. They are mostly used in high-efficient energy storage devices due to their excellent electrical conductivity and electrochemical activity. The negative electrode of the hybrid capacitor is made up of SC materials (carbon-based materials), while the positive electrodes are made up of battery-type or pseudo-capacitor materials. In comparison to conventional SCs and batteries, the resulting hybrid capacitor has a high energy and power density as well as good cycling stability. Nanomaterials, for example, cobalt and nickel-based transition metal hydroxides, sulfides, oxides, phosphates, tellurides, nitrides, etc., have been well researched as superb electrode materials in hybrid capacitors, storing energy in aqueous electrolytes via characteristic reversible redox actions.

Metal Sulfides

Scientists are particularly interested in nickel sulfide nanoparticles (NiS) with hierarchical structures because of their numerous uses in domains such as catalysis, energy, materials, etc. NiS hierarchical structures have appealing features such as a low density and large SSA, which are ideal for electrocatalytic and energy storage applications. NiS is also highly stable, with better redox behavior, and has lower dissolution in alkaline solutions rich in hydroxide ions. As a result, NiS and its various composites are used in battery-type hybrid capacitors as a positive electrode [354]. Nesakumar and co [355] used thiourea and aqueous nickel chloride mixture as an electrolyte to create hierarchical NiS on nickel foam (NiS@Ni) by adopting a simple and easy cathodic electrodeposition technique. Common electroanalytical procedures (cyclic voltammetry, CV and galvanostatic charge–discharge, GCD) were used to examine the positive electrode performance of the NiS@Ni in aqueous KOH. In aqueous KOH, the CV and GCD curves of NiS@Ni revealed distinct reversible redox peaks, confirming the Faradaic battery-type features. The NiS@Ni exhibited an excellent specific capacitance of 1109 C/g at a scan rate of 5 mV/s and 2 A/g, which could be employed as a potential battery-type hybrid-capacitor positive electrode. In the same way, Kaliaraj and Ramadoss [356] also utilized RF magnetron co-sputtering to create a thin film of nickel–zinc sulfide nanocomposite (Ni–ZnS) on a stainless steel substrate, which was employed as the cathode material in an HSC. When compared to the thin film of the ZnS electrode, the electrochemical analysis demonstrated that the Ni–ZnS thin film nanocomposite electrode delivered a greater specific capacitance. The findings show that

doping with Ni has a significant impact on the electrochemical performance of ZnS and that the as-synthesized material can be employed as a possible positive electrode for HSCs.

The structure of vanadium sulfide (VS_2), which is likewise a family of the transition metal dichalcogenides (TMDs), can be expressed as vanadium metal sandwiched between two sulfur layers, which in turn forms a tri-layer of S–V–S glued together using weak Van der Waals forces. The structure allows guest ions to be inserted without altering it, allowing for fast and efficient Faradic operations. It is believed that carbon addition to VS_2 improves the storage performance. With this knowledge, Meyer et al. [357] adopted a hydrothermal synthesis and subsequent optimization of carbon-supported vanadium disulfide nanocomposites that could be used as SC electrodes. The enhanced electronic conductivity of multi-walled CNTs, combined with vanadium disulfide's mild electrocatalytic capacity, generated a synergy that improved effective redox transfer of charges, resulting in increased capacitance. The optimum electrode's minimum resistance to charge transfer and peak to peak voltage difference indicated considerably enhanced charge transfer, which was due to the increased electronic conductivity bolstered by the carbon content. Their findings indicate that vanadium disulfide electrodes with carbon support could be utilized in SCs in the future.

Molybdenum disulfide (MoS_2) nanostructure is one of the metal sulfides that have been studied for SC applications in recent years. Because of structural breakdown, a considerable change in volume during cycling, nanostructure aggregation, and poor conductivity, MoS_2 nanostructures have low-rate efficiency and cyclability. In addition, MoS_2's low cycle stability remains a problem, restricting its broad use in energy storage devices; as a result, several ways are frequently offered to address these concerns, including MoS_2 modification with appropriate atom doping. Nitrogen and carbon doping has proven to be effective in addressing these shortcomings. Fayed and co-researchers used a simple one-step hydrothermal approach to co-doped carbon and nitrogen into MoS_2 nanoflakes [358]. The as-synthesized material, when used as an electrode in SC, recorded a specific power and specific energy of 912 W/kg and 45 Wh/kg, respectively, with retention of about 90% after 3000 cycles. All of these findings demonstrated the material's utility in energy storage applications as a result of heteroatom doping. Recently, vacuum freeze-drying, cross-linking mechanism, heat treatment, and hydrothermal technique were employed by Liu et al. [359] to fabricate a variety of nickel–cobalt–bimetallic sulfide doped with graphite carbon (NCBS/C) nanohybrids. By altering the composition, the electrochemical characteristics of the NCBS/C nanohybrids electrode materials were studied. When used in an asymmetric SC, the NCBS/C nanohybrid and AC as the positive and the negative electrode respectively displayed high electrochemical performance. The transition metal ions cross-linking was well disseminated in the carbon source matrix, which accounted for these performances.

To manufacture ternary arrays of Ni–Co–S linked-nanosheet on conductive carbon substrates as HSC electrodes, Chen et al. [360] adopted a simple one-step electrodeposition process, which resulted in outstanding energy storage capabilities. The asymmetric SC fabricated by the nanosheet arrays of the ternary sulfide (positive electrode) and porous graphene film (negative electrode) (Figure 18a) demonstrated enhanced electrochemical performance for real-life energy storage applications (Figure 18d,e). This was attributed to the nanosheets' mesoporous nature and open framework of the 3D nanostructures, as shown in Figure 18b,c. The device also displayed long-term cycling stability even up to 50,000 cycles, as shown in Figure 18f.
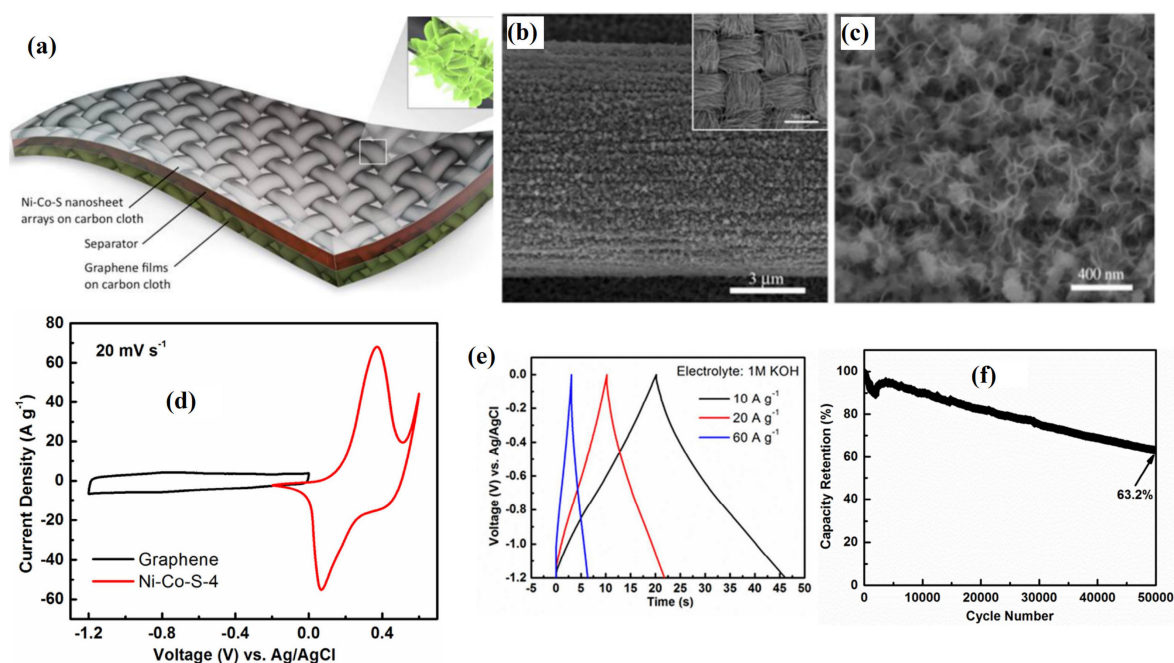
Figure 18. (**a**) Schematic fabrication of the asymmetric SCs. (**b**,**c**) SEM images of the Ni–Co–S-4 nanosheet arrays. (**d**) The CV profiles of the Ni–Co–S-4 (positive electrode) and graphene (negative electrode) in 1M KOH electrolyte. (**e**) GCD of the negative electrode in 1 M KOH electrolyte. (**f**) Cycling stability of the asymmetric SC. Adapted with permission [360]. Copyright (2014) American Chemical Society.

Metal Selenides

Transition metal selenides (TMSes) and their composite have been reported recently as electrode material in battery-type SCs, which have high theoretical capacitance. Because of their possible use in various energy storage devices, they have received a lot of interest owing to their great electrochemical activities and high inherent electrical conductivity. However, the reported TMSe's low energy densities, which are due to their poor mobility of electrolytic ions and tiny active surface area, severely limit their real-life application. For its use in HSC, a simple electrodeposition approach was used to develop Zn–Co–Se on diverse conductive substrates (Figure 19a) [361]. With a maximum operating potential of 1.6 V, the constructed HSC (Zn-Co-Se@Graphene-Ink) (Figure 19c) as the outer and core electrode produced an ultrahigh energy density (approximately 16.97 Wh/kg) and a power density of 539.63 W/kg as shown in Figure 19b. A series of two asymmetric SC devices were used to light up light-emitting diode (LED) bulbs with high intensity for real-time applications, which was successful. As a result, the research offers a novel approach to creating TMSes for energy storage and conversion. Because of the slow diffusion-controlled electrochemical mechanisms in aqueous alkaline electrolytes, nickel chalcogenides as electrode materials frequently have poor rate capabilities and cycle stability. Recently, Co ions were used to manufacture nanotubes of $Ni_xCo_{1-x}Se_2$ [362]. Co ions served as both electronic and morphological modulators. Furthermore, by adjusting the Co^{2+} input amount, the electrochemical kinetics of the device was adjusted utilizing a conventional two-step hydrothermal technique, which delivered a high specific capacitance (1157 F/g at 1 A/g). These performances could be attributed to the synergistic impact that combines the complementary benefits of metal Co and Ni ions, resulting in a large increase in specific capacitance and cycling performance.
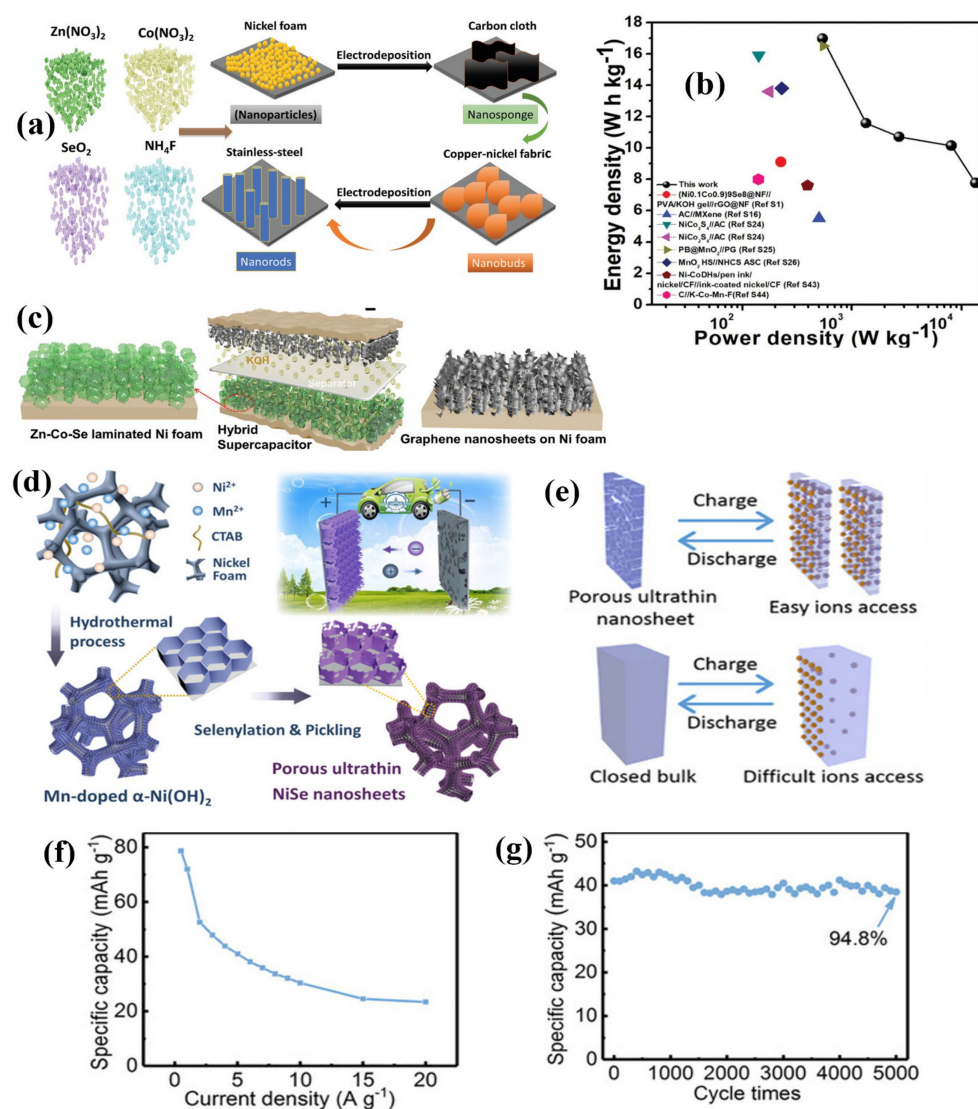
Figure 19. (**a**) Schematic preparation of Zn–Co–Se and Zn–Mn–Se. (**b**) Energy and power density comparison of FAHSC with previous works. (**c**) Schematic illustration of the FAHSC. Adapted with permission [361]. Copyright (2019) John Wiley and Sons. (**d**) Schematics of the fabrication process and application of the porous ultrathin NiSe NNs. (**e**) Schematics of the charge/discharge mechanism, (**f**) Specific capacitance vs. current density, (**g**) Cycle stability of the put-NiSe NNs//PC HSC. Adapted with permission [363]. Copyright (2019) John Wiley and Sons.

A unique, simple approach was also used to fabricate nanosheet networks of porous ultrathin nickel selenide (NiSe NNs) on nickel foam, as shown in Figure 19d [363]. The removal of Mn produced NNs with a highly porous architecture. The ultra-thin nanosheets and superabundant pores of the device aided in the creation of electroactive sites resulting in fast ionic reactions, as shown in Figure 19e. This novel technique for developing new electrode materials for use in HSCs delivered an enhanced electrochemical performance (Figure 19f,g) and provides new paths toward commercializing HSCs using TMSe electrodes. Structural architecture and heteroatom doping are two popular means for improving supercapacitor electrochemical performance. Using a facile two-step hydrothermal process with a SiO_2 template, Qu et al. [364] effectively synthesized a novel tremella-like Ni–Co selenide with ultra-thin and porous nanosheets. The selenization process lowered the resistance and increased the device's conductivity. The assembled HSC delivered an unusual energy density (53.7 Wh/kg at a power density of 822.5 W/kg), which is higher

than the majority of Ni–Co selenide. These features demonstrate the material's enormous potential in practical SC applications.

Metal Tellurides

Metal tellurides, despite being less studied in SC applications, have distinct advantages over other chalcogenide elements. Tellurium (Te) is part of the same O family as other elements with similar chemical properties. It does, however, have some unique physical and chemical features. Te atoms are known to be bonded together in a hexagonal lattice by weak Van der Waals forces to form 1D architectures. Because they provide a large SSA, a robust inter-penetrating channel, and a proficient electron/ion transport pathway, metal tellurides have recently attracted new interest due to their substantial applications in the domains of energy storage, sensing, and thermoelectric devices. For example, Bhol et al. [365] reported the production of Co-decorated Te nanotubes (NTs) employing TeNTs as a template (Figure 20a), as well as the evaluation of their electrochemical performance in HSCs. To begin, they synthesized 1D TeNTs. They further constructed an asymmetric SC with AC as the cathode material. At a current density of 2 A/g, the fabricated device (CoTe-2/AC) demonstrated a high specific capacitance (147 F/g) in a 4 M KOH electrolyte. Furthermore, the CoTe-2/AC assembly attained an exceptional energy density of 51.1 Wh/kg (at a power density of 2294 W/kg), confirming the as-prepared Co-decorated TeNTs to be an effective electrode material (Figure 20b). The device also exhibited good stability during the cycling operations even after 4000 cycles, as shown in Figure 20c. The material's exceptional electrochemical performance is due to its 1D nanostructure with good conductivity. The hydrothermal technique was also used in preparing nickel–cobalt telluride nanorods (NiCoTe-NRs) in one pot utilizing ascorbic acid and cetyltrimethylammonium bromide as reducing agents (Figure 20d) [366]. After modification, the synthesized composite material (NCT-1 NR) was employed as a supercapacitor electrode. A hybrid asymmetric supercapacitor device based on NCT-1 (positive electrode) and orange-peel-derived AC (negative electrode) delivered a high energy density of 43 Wh/kg and a power density of 905 W/kg, as well as a 91% cyclic stability after 25,000 cycles (Figure 20e,f). In a follow-up work by Bhol and his group [54], cobalt–iron (Co–Fe) adorned TeNTs were synthesized using a wet chemical approach. Co–Fe adorned TeNTs together with TeNTs in the backbone had a 1D structure that provided improved conductivity and displayed enhanced electrochemical performance. It was then paired with the AC electrode to optimize the energy density performance. In the 4M KOH electrolyte, the asymmetric arrangement delivered a specific capacitance of 179.2 F/g (at 0.9 A/g). This possible discovery demonstrates TeNTs' usefulness as a template for bimetallic tellurides synthesis with unique geometries. For energy storage applications, the synergistic impact of several metals and anisotropic shape is advantageous.
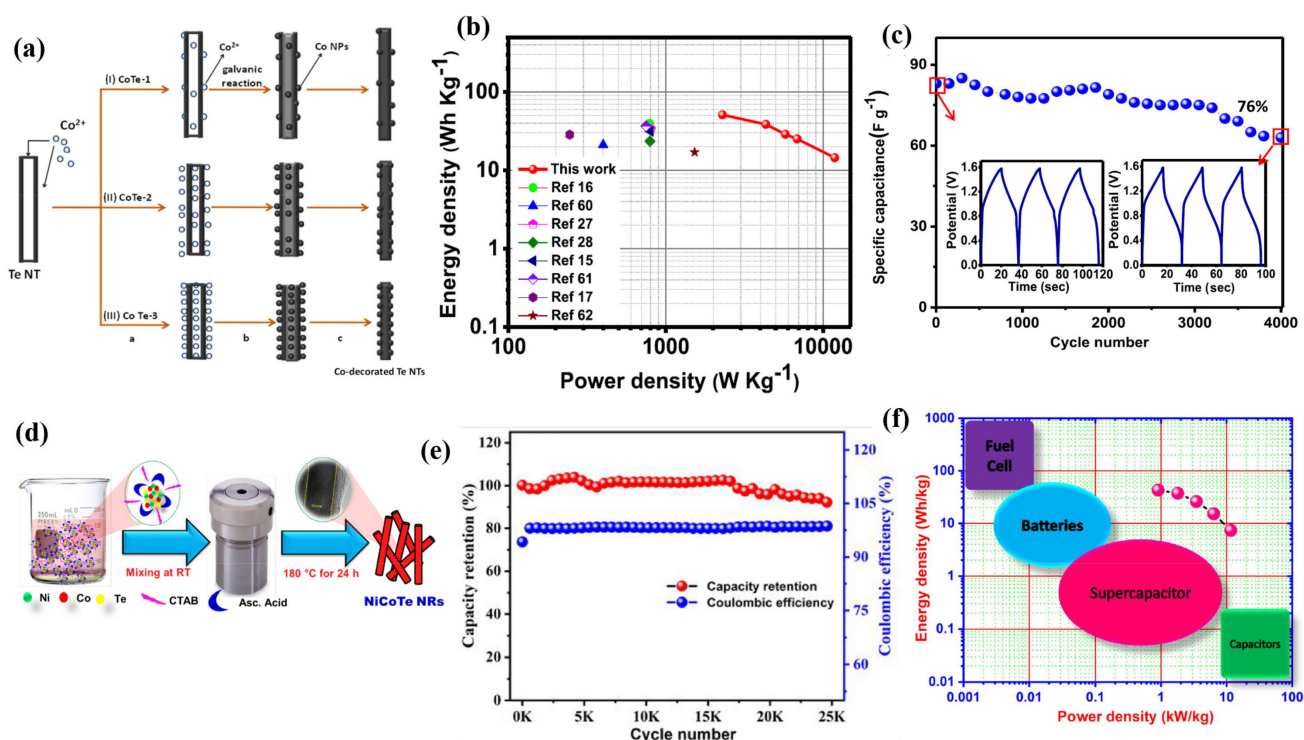
Figure 20. (**a**) Schematics of the preparation process for the formation of Co-decorated TeNTs. (**b**) Ragone plot, and (**c**) Stability measurement of CoTe-2//AC at 4 A/g in a two-electrode setup. Adapted with permission [365]. Copyright (2021) American Chemical Society. (**d**) Illustration process for NiCoTe NR preparation. (**e**) Specific capacity and columbic efficiency vs. cycle number, and (**f**) Ragone plot for the fabricated ASC cell. Adapted with permission [366]. Copyright (2021) American Chemical Society.

3.4. Chalcogenides for Flexible Devices

3.4.1. Flexible Supercapacitors

Due to rapid technological advancements, wearable and portable devices have increasingly become a part of our daily life. As a result, the design of wearable energy storage gadgets is increasingly focusing on the creation of flexible wearable technologies. In wearable devices, a flexible SC is essential. Flexible electrodes, being a crucial component of flexible SC, have an impact on the capacitor's flexibility, stability, and performance. The electrospinning technique is used to create nanofiber materials. They are appropriate for usage as flexible electrodes due to their high flexibility. They also have a lot of potential as the next generation of wearable SCs. Carbon-based materials for SCs, on the other hand, cannot compete with conventional batteries due to their poor energy density, which limits their applicability. Transition metal chalcogenides such as metal sulfides, metal selenides, metal tellurides, etc., have shown high electrochemical performance for flexible devices. As a result, TMCs with specific morphologies, such as hollow and linear, must be prepared. TMCs in flexible SCs require qualities such as high power density, long cycling stability, and exceptional mechanical integrity. The electrolyte and separator used in flexible SCs must also have outstanding mechanical qualities, as well as the properties of traditional capacitor electrolytes and separators. The shape of electrode materials is crucial for fabricating flexible SCs. The materials must be able to bear mechanical stress as well as have the qualities that high-performance energy storage technologies require.

For example, through a hydrothermal reaction, nanowire arrays of binary sulfides $Ni_3Co_6S_8$ (NCS) were produced directly on a nitrogen-doped carbon foam (NCF), which was used as a binder-free electrode for an all-solid-state SC (Figure 21a) [367]. Nanosheet's unique needle-like structures (Figure 21b–e) efficiently improved the active material consumption efficiency and enhanced the electrochemical performance. The NCS–NCF elec-

trode delivered a high-specific capacitance of 243 mAh/g, as well as good rate capability and outstanding cycling stability, as shown in Figure 21f,g. To construct an asymmetric all-solid-state SC, the NCS–NCF was used as a positive electrode and the NCF electrode as a negative electrode. The fabricated device was used in a real-life application to light an LED lamp, which showed an outstanding performance over time (Figure 21h), indicating its potential as an electrode in flexible SCs. A composite material made up of copper sulfide, zinc sulfide, and porous carbon (PC) was also prepared by Zhai et al. [129], which demonstrated an outstanding SC electrode performance. The combination of copper sulfide/zinc sulfide with high pseudo-capacitance and PC material with superb double-layer capacitance produced exceptional electrochemical performances as a flexible SC electrode. The fabricated composite electrode material, when used in symmetric flexible SC, delivered a high energy density, 0.39 Wh/cm^2 at 4.32 W/cm^2 power density. As a result, the copper sulfide/zinc sulfide/PC cotton nanocomposites developed served as an energy storage device with high energy density, which is fascinating and crucial for increasing the flexible SC practical applications.
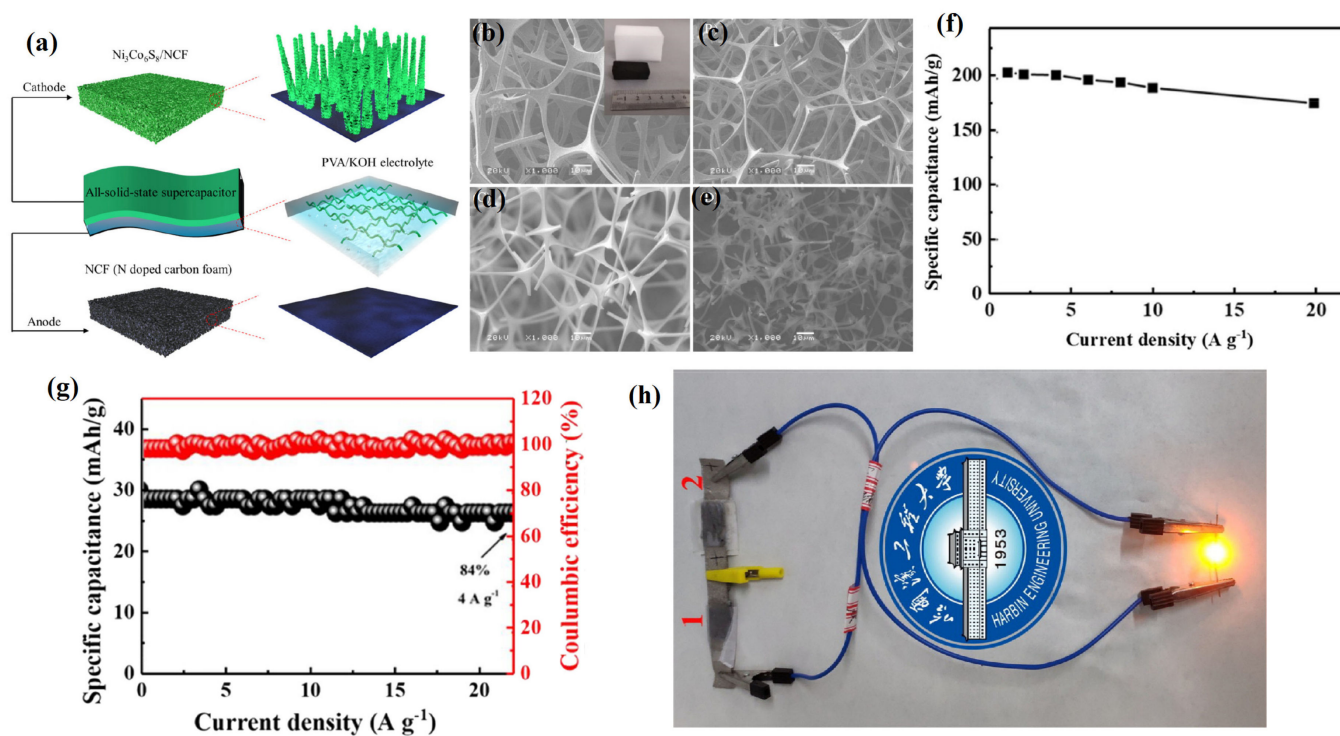
Figure 21. (**a**) Material preparation process and assembly of SCs. SEM images of (**b**) melamine sponge, (**c**) NCF carbonized for 2 h at 800 °C, (**d**) 900 °C, and (**e**) 1000 °C. (**f**) Specific capacitance vs. current density curve. (**g**) Coulombic efficiency and cycling performance of ASC. (**h**) Using the two all-solid-state ASC in series to light LED lamps. Adapted with permission [367]. Copyright (2020) John Wiley and Sons.

Layered metal chalcogenide is a promising new material for high-performance flexible SC electrodes. However, due to poor conductivity caused by the low mobility of carriers, SC performance based on layered TMCs cannot be improved further. To help address this, Mu and co-researchers [368] manufactured flexible interdigital all-solid-state micro-SCs (MSCs) with high mobility of carriers using layered III-VI InSe metal chalcogenides. The MSCs exhibited exceptional performance, including long-term cycling stability and enhanced mechanical flexibility after several bending cycles. The MSCs also delivered a high energy density and an extraordinary power density, which could be attributed to the unique structural layers of the material. Because the electronic structures of ultra-thin 2D crystals are so closely linked to their qualities, several efforts have been made to adjust their

electronic structures to satisfy the high requirements for the fabrication of next-generation smart and portable electronics. For the first time, Hu et al. [369] showed that hydrogen inclusion could alter the conductive behavior of a layered ternary chalcogenide of Cu_2WS_4 (Figure 22a) from semiconducting to metallic, accompanied by a large increase in electrical conductivity. The synthesized material showed nanosized free-standing sheets with a single-crystalline structure as shown in Figure 22b–d. Furthermore, the metallicity of Cu_2WS_4 with hydrogen inclusion was stable and could withstand the high-temperature treatment. With a capacitance of 583.3 F/cm^3 at a current density of 0.31 A/cm^3 (Figure 22e) the constructed all-solid-state flexible SC based on the hydrogenated-Cu_2WS_4 nanosheet film demonstrated remarkable electrochemical capabilities with excellent capacitance retention after 3000 cycles (Figure 22f).
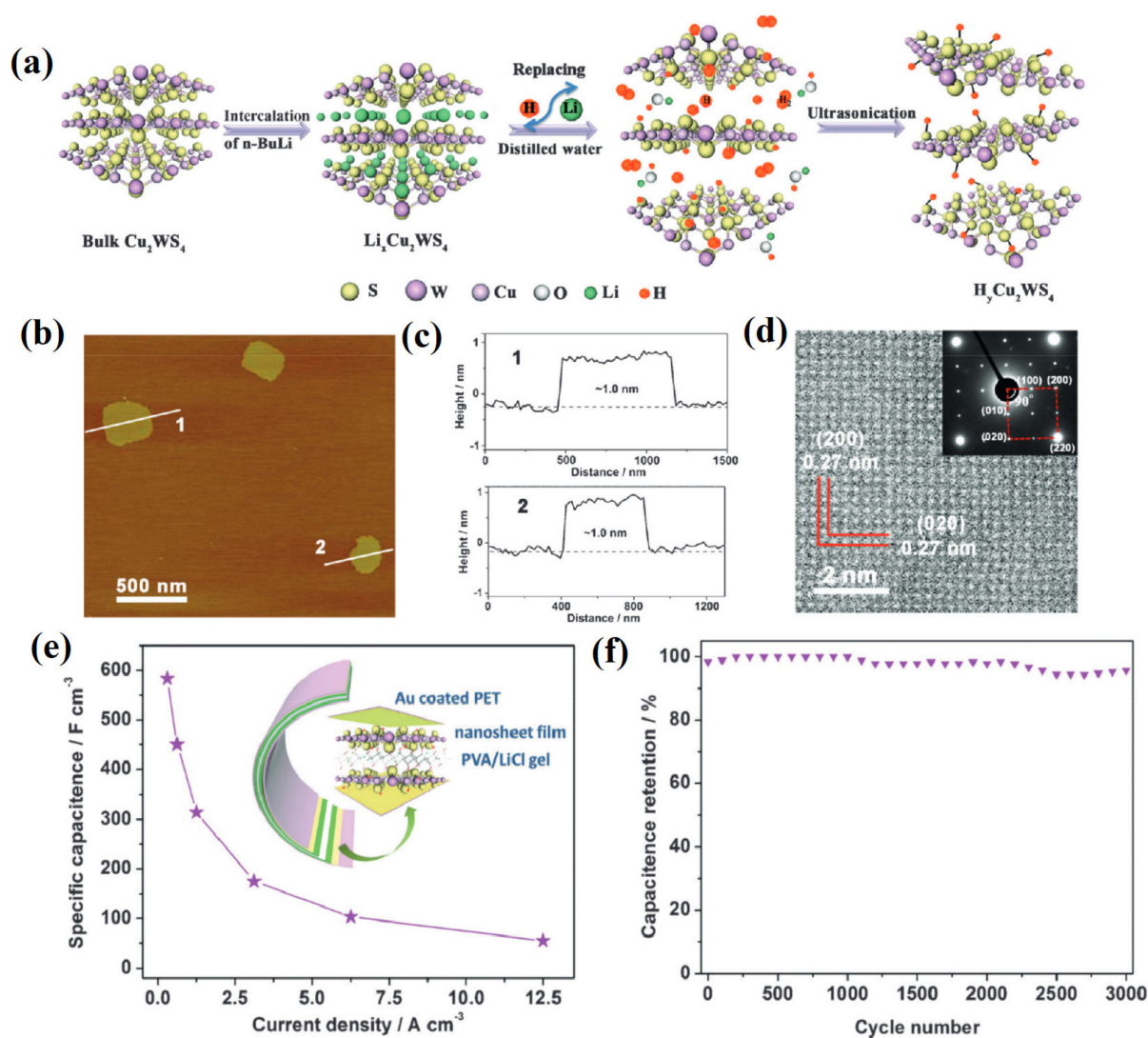
Figure 22. (**a**) Formation of nanosheets of hydrogenated-Cu_2WS_4. (**b**) AFM image, (**c**) Corresponding height diagram, (**d**) HRTEM image, and SAED pattern of the as-synthesized nanosheets. (**e**) Specific capacitance vs. current density (inset: schematic illustration of the as-fabricated symmetrical SC). (**f**) Cycling performance at 1.25 A/cm^3. Adapted with permission [369]. Copyright (2016) John Wiley and Sons.

To increase the sulfide conductivity and transfer rate of ions, an in situ carbon coating technique was employed to embed MXene loaded with sulfide in carbon nanofibers (CNFs) via electrospinning [370]. As a CNF, polyacrylonitrile (PAN) with a good rate of carbon conversion was utilized, and as a sacrificial pore-forming agent, polyvinylpyrroli-

done (PVP) possessing a low carbon conversion rate was used. A thermally-induced phase separation procedure was used to create PAN-PVP-based porous CNFs (PCNF) with high meso- or macropore structures. In situ, nanoparticles of $FeCo_2S_4$ and $Ti_3C_2T_x$ MXene with ultra-thin structures were fixed uniformly in PCNF, and a flexible hybrid film ($FeCo_2S_4$/MXene/PCNF) was created as the SC electrode material. The device produced a continuous pathway for fast electrolyte transport. As a result, the optimized, flexible hybrid membrane film exhibited outstanding cycling stability, effectively addressing the issues of weak cyclic stability and sulfide conductivity.

3.4.2. Flexible Batteries

Various flexible electronic gadgets such as skin-like sensors, roll-up displays, flexible watches, etc., are currently being developed at a rapid pace. These devices require flexible storage systems, e.g., flexible batteries. As a result, efficient electrocatalysts must be developed to optimize the cathodic reactions of the storage devices at the same time. Nonetheless, the slow electrochemical kinetics of the oxygen evolution reaction (OER), oxygen reduction reaction (ORR), and hydrogen evolution reaction (HER) severely limit their energy exploitation and power generation. For HER, ORR, and OER, noble metals such as IrO_2, Pt, and RuO_2 have been utilized as extremely efficient standard catalysts. Their high cost and paucity, on the other hand, expressly limit their application to industrial areas on a massive scale. Therefore, designing highly stable, active, cost-effective, versatile catalysts to improve OER, ORR, and HER activities for scientific purposes is critical. Transition metals chalcogenides and related compounds such as sulfide, oxides, tellurides, and selenide-based catalysts for flexible battery storage are emerging as a class of cost-effective prospective alternatives to the conventional noble metal catalysts. For example, Harish et al. [371] recently created Fe–Sn oxy-selenide ($Fe_xSn_{1-x}OSe$) through a simple and easy hydrothermal and subsequent selenization procedure with enriched oxygen vacancies. The $Fe_{0.33}Sn_{0.67}OSe$ air-cathode-based flexible zinc–air battery (FZAB) delivered a high-power density of 153.96 mW/cm^2 and an ultralong 400-h cycle life, demonstrating its prospects in flexible energy storage.

Exploration of efficient, cost-effective, and corrosion-resistant oxygen electrocatalysts aids in the advancement of ZABs. A unique ternary spinel $CoIn_2Se_4$ nanomaterial was created utilizing a simple and environmentally acceptable process, with In^{3+} and Co^{2+} filling the octahedral and tetrahedral positions of the crystalline structure, respectively, as shown in Figure 23a [372]. The SEM image in Figure 23b showed the composite's nanosheets with equal distribution of the various elements. The fabricated composite material ($CoIn_2Se_4$) was employed as the air cathode for a solid FZAB because of its lower charge resistance and higher active site exposure. The system outperformed the catalyst made of Pt@Ir/C, with a much higher specific capacity of 733 mAh/g$_{Zn}$ and outstanding flexibility, as well as a long cycle life of over 400 cycles (Figure 23c). The $CoIn_2Se_4$-based FZABs were connected in series and successfully powered LED screens for more than 10 h as displayed in Figure 23d,e. Nitrogen-doped carbon (NC) materials and TMSs have both been reported as effective ORR and OER electrocatalysts. An in situ generated 3D-array-structured catalyst constituted of nanoneedles of $Co_{1-x}S$ enwrapped by NC was used to study the electrochemical performance of FZABs [373]. When cycling at 5 mA/cm^2, the FZAB with the catalyst delivered a significantly higher peak power density (242 mW/cm^2) and a high round-trip efficiency of 64%. A macro-porous architecture of hydrangea-shaped $Co_{0.85}Se$ electrocatalyst was also synthesized by Feng and colleagues [374]. Certain defects (S-doped) were inserted into the crystal structure to increase the electronic conductivity of $Co_{0.85}Se$ (Figure 23f). Due to the synergistic effect of Se and S, the S-doped $Co_{0.85}Se$ displayed an extraordinary electrocatalytic activity when used as a Li–S battery cathode on flexible carbon cloth ($Co_{0.85}SeS@CC$). The device's performance (Figure 23h,i) can be attributed to the porous and open networks (Figure 23g) which allowed electrolyte penetration and accommodated sulfur volume fluctuation during the charge–discharge operation.
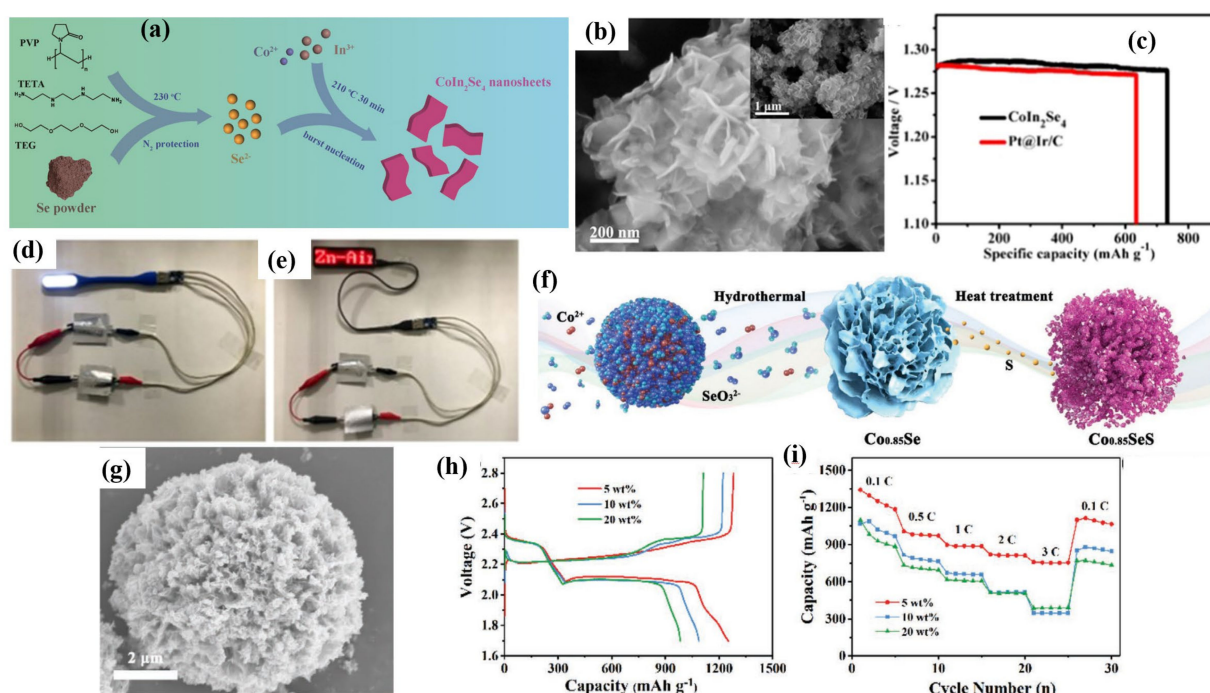
Figure 23. (**a**) Preparation process of $CoIn_2Se_4$ ternary spinel selenide. (**b**) SEM image of $CoIn_2Se_4$ nanosheets. (**c**) Specific capacities of Pt/C- and $CoIn_2Se_4$-based FZABs. (**d**,**e**) Photographs of LED lamps powered by the two-series-connected FZABs. Adapted with permission [372]. Copyright (2020) American Chemical Society. (**f**) Schematics for the synthesis, and (**g**) SEM image of $Co_{0.85}SeS$. (**h**) Charge/discharge curves of Li–S cells cathodes at 0.1 C with different amounts of $Co_{0.85}SeS$. (**i**) Rate capabilities of Li–S cells cathodes with different amounts of $Co_{0.85}SeS$. Adapted with permission [374]. Copyright (2021) John Wiley and Sons.

The use of self-supported electrodes with oxygen catalysts grown directly on the electrode support provides a viable alternative for improving ZAB performance. Yin et al. [375] first used a simple technique to make a self-supporting air electrode for ZABs with Mn doping and grown NiS on nickel foam ($Mn–Ni_3S_2/NF$). After a simple hydrophobic treatment, the optimized $Mn–Ni_3S_2/NF$ electrode could serve as the flexible quasi-solid-state ZAB's air cathode, which delivered a high maximum power density of 75.8 mW/cm^2, superb charge–discharge property, and enhanced stability after 100 cycles. Hybrid Zn batteries (HZBs), which mix Zn-ion (ZIBs) and ZABs, are primarily concerned with the development of high-performance cathodes. As a trifunctional electrode material for HZB, a freestanding hollow fiber joined by heterostructures of S, N-co-doped CNTs (SNCNT) contained Ni_3S_2 nanoparticles was proposed recently [376]. The porous and conductive networks of the device allowed for quick electron/ion routes and a large number of active spots, resulting in higher electrochemical performance. Furthermore, flexible HZB devices fabricated based on the $Ni_3S_2@SNCNT$ flexible cathode achieved outstanding performance and adaptability in a variety of working environments. Even during abrupt changes in the working environment, they have a good unbroken working ability.

4. Conclusions and Future Remark

TMCs are ideal materials for electrochemical energy storage applications because of their unique chemical, structural, electrical, and electrochemical properties. As a result, this review opens with a brief overview of the importance of energy, energy storage devices, and their synthesis based on metal chalcogenides over traditional carbon-based electroactive materials in terms of improved energy and power densities. Due to their intrinsic fragile architecture and defect-assisted constrained charge transports, TMCs perform poorly as standalone electrode materials. This has prompted researchers to experiment with various

organic/inorganic materials to improve the electrochemical performance of pristine TMCs. Fabrication of ternary and quaternary TMCs, composite manufacturing with carbon or conducting polymers, and heteroatom doping using several in situ, one-pot, and ex situ synthesis methods are all examples of modifications that have been studied in recent years. By changing TMCs with the various organic or inorganic materials, the inherent constraints of analogous materials will be compensated while maintaining or improving the performance of old systems, and new capabilities will be realized that are not possible with conventional materials. We have also included a list of many well-known synthesis techniques for creating modified and nanostructured TMCs. Furthermore, we have focused on the critical role of various modifying agents, such as carbon-based allotropes, heteroatoms, other metal-based composites, etc., in significantly influencing the pristine features of electroactive TMCs. How these agents aid in optimizing the electrochemical performance of TMCs by optimizing their rate of redox reaction kinetics and charge transport processes has also been discussed. Special attention was paid to utilizing various TMCs (such as selenides, tellurides, and sulfides) and their composites as electrode materials in solid-state batteries, supercapacitors, and their flexible components in real-life applications.

Although great efforts have been made in recent years to improve TMCs' electrochemical performance to realize state-of-the-art applicable energy storage devices, there are still several key problems that need to be addressed. Prospects in this particular path will be defined by how we address such issues and overcome considerable limitations, some of which have been listed as follows:

(i).   Although several studies on modified TMCs have been published, their architecture-dependent feature modification has not been thoroughly examined. TMCs, for example, can be made in a variety of morphologies, including hierarchical, core-shell, and surface ornamentations.

(ii).   Advanced characterization methods such as in situ spectroscopy and imaging are appealing to the research industry because they provide real-time information about the reaction methods involved. These techniques can be used to establish a relationship between the material's composition, structure, characteristics, and electrochemical performance. Furthermore, these techniques would aid in determining the underlying electrochemical reactions as well as monitoring the structural changes in the material during applications.

(iii). Doping various heteroatoms such as oxygen, nitrogen, phosphorous, etc., into electroactive materials has been shown to improve their capacitive performance. Although this is relatively prevalent in carbon-based electroactive materials, it is quite rare in TMCs. Heteroatoms have been discovered to improve the electroactive materials' electronic conductivity, which could aid rate performance in electrochemical energy storage applications. Furthermore, because of their affinity for various ionic species, these heteroatoms can act as anchoring points for ions within the electrolytes, thus increasing charge storage capabilities dramatically. For high-performance storage applications, heteroatom-doped TMC-based hybrid electroactive materials will be of great interest.

References

1. Badwal, S.P.S.; Giddey, S.S.; Munnings, C.; Bhatt, A.I.; Hollenkamp, A.F. Emerging electrochemical energy conversion and storage technologies. *Front. Chem.* **2014**, *2*, 79. [CrossRef] [PubMed]
2. Gielen, D.; Boshell, F.; Saygin, D.; Bazilian, M.D.; Wagner, N.; Gorini, R. The role of renewable energy in the global energy transformation. *Energy Strategy Rev.* **2019**, *24*, 38–50. [CrossRef]
3. Gao, M.-R.; Xu, Y.-F.; Jiang, J.; Yu, S.-H. Nanostructured metal chalcogenides: Synthesis, modification, and applications in energy conversion and storage devices. *Chem. Soc. Rev.* **2013**, *42*, 2986–3017. [CrossRef]
4. Yu, X.-Y.; Yu, L.; Lou, X.W. Metal Sulfide Hollow Nanostructures for Electrochemical Energy Storage. *Adv. Energy Mater.* **2016**, *6*, 1501333. [CrossRef]
5. Yuan, H.; Kong, L.; Li, T.; Zhang, Q. A review of transition metal chalcogenide/graphene nanocomposites for energy storage and conversion. *Chin. Chem. Lett.* **2017**, *28*, 2180–2194. [CrossRef]
6. Choi, W.; Choudhary, N.; Han, G.H.; Park, J.; Akinwande, D.; Lee, Y.H. Recent development of two-dimensional transition metal dichalcogenides and their applications. *Mater. Today* **2017**, *20*, 116–130. [CrossRef]
7. Kulandaivalu, S.; Sulaiman, Y. Recent Advances in Layer-by-Layer Assembled Conducting Polymer Based Composites for Supercapacitors. *Energies* **2019**, *12*, 2107. [CrossRef]
8. Yan, Z.; Ji, M.; Xia, J.; Zhu, H. Recent Advanced Materials for Electrochemical and Photoelectrochemical Synthesis of Ammonia from Dinitrogen: One Step Closer to a Sustainable Energy Future. *Adv. Energy Mater.* **2020**, *10*, 1902020. [CrossRef]
9. Luo, F.; Li, J.; Yuan, H.; Xiao, D. Rapid synthesis of three-dimensional flower-like cobalt sulfide hierarchitectures by microwave assisted heating method for high-performance supercapacitors. *Electrochim. Acta* **2014**, *123*, 183–189. [CrossRef]
10. Zhang, H.; Li, X.; Liu, W.; Yue, H.; Shi, Z.; Yin, Y.; Yang, S. Olivine LiFePO4 as an additive into LiCoO2 electrodes for LIBs to improve high-voltage performances. *J. Alloys Compd.* **2021**, *869*, 159188. [CrossRef]
11. Abraham, K.M. Intercalation positive electrodes for rechargeable sodium cells. *Solid State Ionics* **1982**, *7*, 199–212. [CrossRef]
12. Rajabathar, J.R.; Al-lohedan, H.A.; Arunachalam, P.; Issa, Z.A.; Gnanamani, M.K.; Appaturi, J.N.; Ibrahim, S.N.; Mohammed Dahan, W. Unexpected discovery of low-cost maricite NaFePO$_4$ as a high-performance electrode for Na-ion batteries. *J. Alloys Compd.* **2021**, *850*, 540–545.
13. Rajabathar, J.R.; Al-lohedan, H.A.; Arunachalam, P.; Issa, Z.A.; Gnanamani, M.K.; Appaturi, J.N.; Ibrahim, S.N.; Mohammed Dahan, W. Challenges for Na-ion negative electrodes. *J. Alloys Compd.* **2021**, *850*, A1011.
14. Rajabathar, J.R.; Al-lohedan, H.A.; Arunachalam, P.; Issa, Z.A.; Gnanamani, M.K.; Appaturi, J.N.; Ibrahim, S.N.; Mohammed Dahan, W. Sodium-Ion Batteries. *J. Alloys Compd.* **2021**, *850*, 947–958. [CrossRef]
15. Hwang, J.-Y.; Myung, S.-T.; Sun, Y.-K. Sodium-ion batteries: Present and future. *Chem. Soc. Rev.* **2017**, *46*, 3529–3614. [CrossRef] [PubMed]
16. Nagde, K.R.; Dhoble, S.J. Li-S ion batteries: A substitute for Li-ion storage batteries. In *Energy Materials*; Elsevier: Amsterdam, The Netherlands, 2021; pp. 335–371.
17. Evers, S.; Yim, T.; Nazar, L.F. Understanding the nature of absorption/adsorption in nanoporous polysulfide sorbents for the Li–S battery. *J. Phys. Chem. C* **2012**, *116*, 19653–19658. [CrossRef]
18. Moy, D.; Narayanan, S.R. Mixed Conduction Membranes Suppress the Polysulfide Shuttle in Lithium-Sulfur Batteries. *J. Electrochem. Soc.* **2017**, *164*, A560–A566. [CrossRef]
19. Moy, D.; Manivannan, A.; Narayanan, S.R. Direct Measurement of Polysulfide Shuttle Current: A Window into Understanding the Performance of Lithium-Sulfur Cells. *J. Electrochem. Soc.* **2014**, *162*, A1–A7. [CrossRef]
20. Li, H.; Tsai, C.; Koh, A.L.; Cai, L.; Contryman, A.W.; Fragapane, A.H.; Zhao, J.; Han, H.S.; Manoharan, H.C.; Abild-Pedersen, F.; et al. Activating and optimizing MoS2 basal planes for hydrogen evolution through the formation of strained sulphur vacancies. *Nat. Mater.* **2016**, *15*, 48–53. [CrossRef]
21. Ji, G.; Yu, Y.; Yao, Q.; Qu, B.; Chen, D.; Chen, W.; Xie, J.; Lee, J.Y. Promotion of reversible Li+ storage in transition metal dichalcogenides by Ag nanoclusters. *NPG Asia Mater.* **2016**, *8*, e247. [CrossRef]
22. Lin, H.; Yang, L.; Jiang, X.; Li, G.; Zhang, T.; Yao, Q.; Zheng, G.W.; Lee, J.Y. Electrocatalysis of polysulfide conversion by sulfur-deficient MoS2 nanoflakes for lithium–sulfur batteries. *Energy Environ. Sci.* **2017**, *10*, 1476–1486. [CrossRef]
23. Clark, S.; Latz, A.; Horstmann, B. A Review of Model-Based Design Tools for Metal-Air Batteries. *Batteries* **2018**, *4*, 5. [CrossRef]
24. Zou, X.; Lu, Q.; Liao, K.; Shao, Z. Towards practically accessible aprotic Li-air batteries: Progress and challenges related to oxygen-permeable membranes and cathodes. *Energy Storage Mater.* **2022**, *45*, 869–902. [CrossRef]
25. Lu, S.-H.; Lu, H.-C. Pouch-type hybrid Li-air battery enabled by flexible composite lithium-ion conducting membrane. *J. Power Source* **2021**, *489*, 229431. [CrossRef]
26. Parveen, N.; Khan, Z.; Ansari, S.A.; Park, S.; Senthilkumar, S.T.; Kim, Y.; Ko, H.; Cho, M.H. Feasibility of using hollow double walled Mn2O3 nanocubes for hybrid Na-air battery. *Chem. Eng. J.* **2019**, *360*, 415–422. [CrossRef]
27. Wang, H.; Xu, Q. Materials Design for Rechargeable Metal-Air Batteries. *Matter* **2019**, *1*, 565–595. [CrossRef]
28. Hou, X.; Zhang, Y.; Cui, C.; Lin, C.; Li, Y.; Bu, D.; Yan, G.; Liu, D.; Wu, Q.; Song, X.-M. Photo-assisted Al-air batteries based on gel-state electrolyte. *J. Power Source* **2022**, *533*, 231377. [CrossRef]
29. Wu, P.; Zhao, Q.; Yu, H.; Tang, Z.; Li, Y.; Huang, D.; Sun, D.; Wang, H.; Tang, Y. Modification on water electrochemical environment for durable Al-Air Battery: Achieved by a Low-Cost sucrose additive. *Chem. Eng. J.* **2022**, *438*, 135538. [CrossRef]

30. Zhang, L.; Shao, Q.; Zhang, J. An overview of non-noble metal electrocatalysts and their associated air cathodes for Mg-air batteries. *Mater. Rep. Energy* **2021**, *1*, 100002. [CrossRef]

31. Vaghefinazari, B.; Snihirova, D.; Wang, C.; Wang, L.; Deng, M.; Höche, D.; Lamaka, S.V.; Zheludkevich, M.L. Exploring the effect of sodium salt of Ethylenediaminetetraacetic acid as an electrolyte additive on electrochemical behavior of a commercially pure Mg in primary Mg-air batteries. *J. Power Source* **2022**, *527*, 231176. [CrossRef]

32. Leong, K.W.; Wang, Y.; Ni, M.; Pan, W.; Luo, S.; Leung, D.Y.C. Rechargeable Zn-air batteries: Recent trends and future perspectives. *Renew. Sustain. Energy Rev.* **2022**, *154*, 111771. [CrossRef]

33. Qian, M.; Guo, M.; Qu, Y.; Xu, M.; Liu, D.; Hou, C.; Isimjan, T.T.; Yang, X. Energy barrier engineering of oxygen reduction reaction synergistically promoted by binary Zn-Cu pair sites for advanced Zn–air batteries. *J. Alloys Compd.* **2022**, *907*, 164527. [CrossRef]

34. Hang, B.T.; Watanabe, T.; Egashira, M.; Watanabe, I.; Okada, S.; Yamaki, J. The effect of additives on the electrochemical properties of Fe/C composite for Fe/air battery anode. *J. Power Source* **2006**, *155*, 461–469. [CrossRef]

35. Hang, B.T.; Hayashi, H.; Yoon, S.-H.; Okada, S.; Yamaki, J. Fe_2O_3-filled carbon nanotubes as a negative electrode for an Fe–air battery. *J. Power Source* **2008**, *178*, 393–401. [CrossRef]

36. Inoishi, A.; Ida, S.; Uratani, S.; Okano, T.; Ishihara, T. High capacity of an Fe–air rechargeable battery using LaGaO3-based oxide ion conductor as an electrolyte. *Phys. Chem. Chem. Phys.* **2012**, *14*, 12818–12822. [CrossRef]

37. Lyu, Z.; Zhou, Y.; Dai, W.; Cui, X.; Lai, M.; Wang, L.; Huo, F.; Huang, W.; Hu, Z.; Chen, W. Recent advances in understanding of the mechanism and control of Li $2 O_2$ formation in aprotic Li–O_2 batteries. *Chem. Soc. Rev.* **2017**, *46*, 6046–6072. [CrossRef]

38. Geng, D.; Ding, N.-N.; Hor, T.S.A.; Chien, S.W.; Liu, Z.; Zong, Y. Cobalt sulfide nanoparticles impregnated nitrogen and sulfur co-doped graphene as bifunctional catalyst for rechargeable Zn–air batteries. *RSC Adv.* **2015**, *5*, 7280–7284. [CrossRef]

39. Olabi, A.G.; Sayed, E.T.; Wilberforce, T.; Jamal, A.; Alami, A.H.; Elsaid, K.; Rahman, S.M.; Shah, S.K.; Abdelkareem, M.A. Metal-Air Batteries—A Review. *Energies* **2021**, *14*, 7373. [CrossRef]

40. Bao, S.-J.; Li, C.M.; Guo, C.-X.; Qiao, Y. Biomolecule-assisted synthesis of cobalt sulfide nanowires for application in supercapacitors. *J. Power Source* **2008**, *180*, 676–681. [CrossRef]

41. Subramanian, A.; Punnoose, D.; Raman, V.; Gopi, C.V.V.M.; Rao, S.S.; Khan, M.A.; Kim, H.-J. Layer by layer approach to enhance capacitance using metal sulfides for supercapacitor applications. *Mater. Lett.* **2018**, *231*, 64–67. [CrossRef]

42. Sajedi-Moghaddam, A.; Saievar-Iranizad, E.; Pumera, M. Two-dimensional transition metal dichalcogenide/conducting polymer composites: Synthesis and applications. *Nanoscale* **2017**, *9*, 8052–8065. [CrossRef] [PubMed]

43. Kim, Y.; Park, T.; Na, J.; Yi, J.W.; Kim, J.; Kim, M.; Bando, Y.; Yamauchi, Y.; Lin, J. Layered transition metal dichalcogenide/carbon nanocomposites for electrochemical energy storage and conversion applications. *Nanoscale* **2020**, *12*, 8608–8625. [CrossRef] [PubMed]

44. Cherusseri, J.; Choudhary, N.; Sambath Kumar, K.; Jung, Y.; Thomas, J. Recent trends in transition metal dichalcogenide based supercapacitor electrodes. *Nanoscale Horiz.* **2019**, *4*, 840–858. [CrossRef]

45. Ahmad, M.; Hussain, I.; Nawaz, T.; Li, Y.; Chen, X.; Ali, S.; Imran, M.; Ma, X.; Zhang, K. Comparative study of ternary metal chalcogenides (MX; M= Zn–Co–Ni; X= S, Se, Te): Formation process, charge storage mechanism and hybrid supercapacitor. *J. Power Source* **2022**, *534*, 231414. [CrossRef]

46. Teli, A.M.; Beknalkar, S.A.; Mane, S.M.; Bhat, T.S.; Kambale, B.B.; Patil, S.B.; Sadale, S.B.; Shin, J.C. Electrodeposited crumpled MoS_2 nanoflakes for asymmetric supercapacitor. *Ceram. Int.* **2022**, *in press*. [CrossRef]

47. Sharma, G.K.; Ranjan, B.; Kaur, D. Electrochemical kinetics of 2D-MoS_2 sputtered over stainless-steel mesh: Insights into the Na+ ions storage for flexible supercapacitors. *Ceram. Int.* **2022**, *in press*. [CrossRef]

48. Gao, Y.-P.; Huang, K.-J.; Wu, X.; Hou, Z.-Q.; Liu, Y.-Y. MoS2 nanosheets assembling three-dimensional nanospheres for enhanced-performance supercapacitor. *J. Alloys Compd.* **2018**, *741*, 174–181. [CrossRef]

49. Thanh, T.D.; Chuong, N.D.; Van Hien, H.; Kshetri, T.; Kim, N.H.; Lee, J.H. Recent advances in two-dimensional transition metal dichalcogenides-graphene heterostructured materials for electrochemical applications. *Prog. Mater. Sci.* **2018**, *96*, 51–85. [CrossRef]

50. Yang, X.; Zhao, L.; Lian, J. Arrays of hierarchical nickel sulfides/MoS2 nanosheets supported on carbon nanotubes backbone as advanced anode materials for asymmetric supercapacitor. *J. Power Source* **2017**, *343*, 373–382. [CrossRef]

51. Sun, T.; Li, Z.; Liu, X.; Ma, L.; Wang, J.; Yang, S. Facile construction of 3D graphene/MoS_2 composites as advanced electrode materials for supercapacitors. *J. Power Source* **2016**, *331*, 180–188. [CrossRef]

52. Ray, S.K.; Pant, B.; Park, M.; Hur, J.; Lee, S.W. Cavity-like hierarchical architecture of WS_2/α-$NiMoO_4$ electrodes for supercapacitor application. *Ceram. Int.* **2020**, *46*, 19022–19027. [CrossRef]

53. Li, Y.; Wang, H.; Shu, T.; Yuan, J.; Lu, G.; Lin, B.; Gao, Z.; Wei, F.; Ma, C.; Qi, J.; et al. Two-dimensional hierarchical MoS2 lamella inserted in CoS2 flake as an advanced supercapacitor electrode. *J. Energy Storage* **2022**, *51*, 104299. [CrossRef]

54. Bhol, P.; Swain, S.; Altaee, A.; Saxena, M.; Samal, A.K. Cobalt–iron decorated tellurium nanotubes for high energy density supercapacitor. *Mater. Today Chem.* **2022**, *24*, 100871. [CrossRef]

55. Rathore, H.K.; Hariram, M.; Ganesha, M.K.; Singh, A.K.; Das, D.; Kumar, M.; Awasthi, K.; Sarkar, D. Charge storage mechanism in vanadium telluride/carbon nanobelts as electroactive material in an aqueous asymmetric supercapacitor. *J. Colloid Interface Sci.* **2022**, *621*, 110–118. [CrossRef] [PubMed]

56. Theerthagiri, J.; Karuppasamy, K.; Durai, G.; Rana, A.U.H.S.; Arunachalam, P.; Sangeetha, K.; Kuppusami, P.; Kim, H.-S. Recent Advances in Metal Chalcogenides (MX; X = S, Se) Nanostructures for Electrochemical Supercapacitor Applications: A Brief Review. *Nanomaterials* **2018**, *8*, 256. [CrossRef]

57. Miao, C.; Xia, G.; Zhu, K.; Ye, K.; Wang, Q.; Yan, J.; Cao, D.; Gong, F.; Wang, G. Enhanced supercapacitor performance of bimetallic metal selenides via controllable synergistic engineering of composition. *Electrochim. Acta* **2021**, *370*, 137802. [CrossRef]

58. Lei, H.; Zhou, J.; Zhao, R.; Peng, H.; Xu, Y.; Wang, F.; Hamouda, H.A.; Zhang, W.; Ma, G. Design and assembly of a novel asymmetric supercapacitor based on all-metal selenides electrodes. *Electrochim. Acta* **2020**, *363*, 137206. [CrossRef]

59. Amiri, M.; Saeed Hosseiny Davarani, S.; Ebrahim Moosavifard, S.; Fu, Y.-Q. Cobalt-molybdenum selenide double-shelled hollow nanocages derived from metal-organic frameworks as high performance electrodes for hybrid supercapacitor. *J. Colloid Interface Sci.* **2022**, *616*, 141–151. [CrossRef]

60. Liu, Q.; Hong, X.; You, X.; Zhang, X.; Zhao, X.; Chen, X.; Ye, M.; Liu, X. Designing heterostructured metal sulfide core-shell nanoneedle films as battery-type electrodes for hybrid supercapacitors. *Energy Storage Mater.* **2020**, *24*, 541–549. [CrossRef]

61. Wang, Q.; Qu, Z.; Chen, S.; Zhang, D. Metal organic framework derived P-doping CoS@C with sulfide defect to boost high-performance asymmetric supercapacitors. *J. Colloid Interface Sci.* **2022**, *in press*. [CrossRef]

62. Lu, L.; Xu, Q.; Chen, Y.; Zhou, Y.; Jiang, T.; Zhao, Q. Preparation of metal sulfide electrode materials derived based on metal organic framework and application of supercapacitors. *J. Energy Storage* **2022**, *49*, 104073. [CrossRef]

63. Yu, S.; Xiong, X.; Ma, J.; Qian, H. One-step preparation of cobalt nickel oxide hydroxide @ cobalt sulfide heterostructure film on Ni foam through hydrothermal electrodeposition for supercapacitors. *Surf. Coat. Technol.* **2021**, *426*, 127791. [CrossRef]

64. Sahoo, S.; Krishnamoorthy, K.; Pazhamalai, P.; Mariappan, V.K.; Kim, S.-J. Copper molybdenum sulfide: A novel pseudocapacitive electrode material for electrochemical energy storage device. *Int. J. Hydrogen Energy* **2018**, *43*, 12222–12232. [CrossRef]

65. Rajabathar, J.R.; Al-lohedan, H.A.; Arunachalam, P.; Issa, Z.A.; Gnanamani, M.K.; Appaturi, J.N.; Ibrahim, S.N.; Mohammed Dahan, W. Synthesis and characterization of metal chalcogenide modified graphene oxide sandwiched manganese oxide nanofibers on nickel foam electrodes for high performance supercapacitor applications. *J. Alloys Compd.* **2021**, *850*, 156346. [CrossRef]

66. Nagaraju, M.; Chandra Sekhar, S.; Ramulu, B.; Arbaz, S.J.; Yu, J.S. In situ deposited cobalt-magnesium selenates as an advanced electrode for electrochemical energy storage. *J. Magnes. Alloys* **2022**, *in press*. [CrossRef]

67. Sakthivel, M.; Sukanya, R.; Chen, S.-M.; Pandi, K.; Ho, K.-C. Synthesis and characterization of bimetallic nickel-cobalt chalco-genides (NiCoSe$_2$, NiCo$_2$S$_4$, and NiCo$_2$O$_4$) for non-enzymatic hydrogen peroxide sensor and energy storage: Electrochemical properties dependence on the metal-to-chalcogen composition. *Renew. Energy* **2019**, *138*, 139–151. [CrossRef]

68. Wang, Y.; Zhang, W.; Guo, X.; Liu, Y.; Zheng, Y.; Zhang, M.; Li, R.; Peng, Z.; Zhang, Y.; Zhang, T. One-step microwave-hydrothermal preparation of NiS/rGO hybrid for high-performance symmetric solid-state supercapacitor. *Appl. Surf. Sci.* **2020**, *514*, 146080. [CrossRef]

69. Nandhini, S.; Muralidharan, G. Facile microwave-hydrothermal synthesis of NiS nanostructures for supercapacitor applications. *Appl. Surf. Sci.* **2018**, *449*, 485–491. [CrossRef]

70. Ansari, A.; Badhe, R.A.; Babar, D.G.; Garje, S.S. One pot solvothermal synthesis of bimetallic copper iron sulfide (CuFeS$_2$) and its use as electrode material in supercapacitor applications. *Appl. Surf. Sci. Adv.* **2022**, *9*, 100231. [CrossRef]

71. Qu, J.; Bai, Y.; Li, X.; Song, K.; Zhang, S.; Wang, X.; Wang, X.; Dai, S. Rational design of NiSe$_2$@rGO nanocomposites for advanced hybrid supercapacitors. *J. Mater. Res. Technol.* **2021**, *15*, 6155–6161. [CrossRef]

72. Gowrisankar, A.; Sherryn, A.L.; Selvaraju, T. In situ integrated 2D reduced graphene oxide nanosheets with MoSSe for hydrogen evolution reaction and supercapacitor application. *Appl. Surf. Sci. Adv.* **2021**, *3*, 100054. [CrossRef]

73. Liu, Y.; Zhao, D.; Liu, H.; Umar, A.; Wu, X. High performance hybrid supercapacitor based on hierarchical MoS$_2$/Ni$_3$S$_2$ metal chalcogenide. *Chin. Chem. Lett.* **2019**, *30*, 1105–1110. [CrossRef]

74. Manikandan, R.; Justin Raj, C.; Nagaraju, G.; Velayutham, R.; Moulton, S.E.; Puigdollers, J.; Chul Kim, B. Selenium enriched hybrid metal chalcogenides with enhanced redox kinetics for high-energy density supercapacitors. *Chem. Eng. J.* **2021**, *414*, 128924. [CrossRef]

75. Kim, Y.; Samuel, E.; Joshi, B.; Park, C.; Lee, H.S.; Yoon, S.S. Flexible metallized carbon nanofibers decorated with two-dimensional NiGa$_2$S$_4$ nanosheets as supercapacitor electrodes. *Chem. Eng. J.* **2021**, *420*, 130497. [CrossRef]

76. Zhang, S.; Dai, P.; Liu, H.; Yan, L.; Song, H.; Liu, D.; Zhao, X. Metal-organic framework derived porous flakes of cobalt chalcogenides (CoX, X = O, S, Se and Te) rooted in carbon fibers as flexible electrode materials for pseudocapacitive energy storage. *Electrochim. Acta* **2021**, *369*, 137681. [CrossRef]

77. Shaikh, S.; Rabinal, M.K. Rapid ambient growth of copper sulfide microstructures: Binder free electrodes for supercapacitor. *J. Energy Storage* **2020**, *28*, 101288. [CrossRef]

78. Gohar, R.S.; Ahmad, I.; Shah, A.; Majeed, S.; Najam-Ul-Haq, M.; Ashiq, M.N. Fabrication of transition-metal oxide and chalcogenide nanostructures with enhanced electrochemical performances. *J. Energy Storage* **2020**, *31*, 101621. [CrossRef]

79. Maity, C.K.; Goswami, N.; Verma, K.; Sahoo, S.; Nayak, G.C. A facile synthesis of boron nitride supported zinc cobalt sulfide nano hybrid as high-performance pseudocapacitive electrode material for asymmetric supercapacitors. *J. Energy Storage* **2020**, *32*, 101993. [CrossRef]

80. Ghosh, S.; Samanta, P.; Murmu, N.C.; Kuila, T. Investigation of electrochemical charge storage in nickel-cobalt-selenide/reduced graphene oxide composite electrode and its hybrid supercapacitor device. *J. Alloys Compd.* **2020**, *835*, 155432. [CrossRef]

81. Zhang, F.; Tang, Y.; Liu, H.; Ji, H.; Jiang, C.; Zhang, J.; Zhang, X.; Lee, C.-S. Uniform Incorporation of Flocculent Molybdenum Disulfide Nanostructure into Three-Dimensional Porous Graphene as an Anode for High-Performance Lithium Ion Batteries and Hybrid Supercapacitors. *ACS Appl. Mater. Interfaces* **2016**, *8*, 4691–4699. [CrossRef]

82. Wang, R.; Wang, S.; Jin, D.; Zhang, Y.; Cai, Y.; Ma, J.; Zhang, L. Engineering layer structure of MoS2-graphene composites with robust and fast lithium storage for high-performance Li-ion capacitors. *Energy Storage Mater.* **2017**, *9*, 195–205. [CrossRef]

83. Wang, C.; Zhan, C.; Ren, X.; Lv, R.; Shen, W.; Kang, F.; Huang, Z.-H. MoS2/carbon composites prepared by ball-milling and pyrolysis for the high-rate and stable anode of lithium ion capacitors. *RSC Adv.* **2019**, *9*, 42316–42323. [CrossRef] [PubMed]

84. Chao, J.; Yang, L.; Zhang, H.; Liu, J.; Hu, R.; Zhu, M. Engineering layer structure of MoS_2/polyaniline/graphene nanocomposites to achieve fast and reversible lithium storage for high energy density aqueous lithium-ion capacitors. *J. Power Source* **2020**, *450*, 227680. [CrossRef]

85. Zhang, H.-J.; Jia, Q.-C.; Kong, L.-B. Multi-dimensional hybrid heterostructure MoS_2@C nanocomposite as a highly reversible anode for high-energy lithium-ion capacitors. *Appl. Surf. Sci.* **2020**, *531*, 147222. [CrossRef]

86. Wang, R.; Wang, S.; Peng, X.; Zhang, Y.; Jin, D.; Chu, P.K.; Zhang, L. Elucidating the Intercalation Pseudocapacitance Mechanism of MoS_2–Carbon Monolayer Interoverlapped Superstructure: Toward High-Performance Sodium-Ion-Based Hybrid Supercapacitor. *ACS Appl. Mater. Interfaces* **2017**, *9*, 32745–32755. [CrossRef]

87. Li, Y.; Wang, H.; Wang, L.; Wang, R.; He, B.; Gong, Y.; Hu, X. Ultrafast Na+-storage in TiO_2-coated MoS_2@N-doped carbon for high-energy sodium-ion hybrid capacitors. *Energy Storage Mater.* **2019**, *23*, 95–104. [CrossRef]

88. Wu, Y.; Chen, H.; Zhang, L.; Li, Q.; Xu, M.; Bao, S. A rough endoplasmic reticulum-like VSe_2/rGO anode for superior sodium-ion capacitors. *Inorg. Chem. Front.* **2019**, *6*, 2935–2943. [CrossRef]

89. Tang, J.; Huang, X.; Lin, T.; Qiu, T.; Huang, H.; Zhu, X.; Gu, Q.; Luo, B.; Wang, L. MXene derived TiS_2 nanosheets for high-rate and long-life sodium-ion capacitors. *Energy Storage Mater.* **2020**, *26*, 550–559. [CrossRef]

90. Liu, J.; Xu, Y.-G.; Kong, L.-B. Synthesis of polyvalent ion reaction of MoS_2/CoS_2-RGO anode materials for high-performance sodium-ion batteries and sodium-ion capacitors. *J. Colloid Interface Sci.* **2020**, *575*, 42–53. [CrossRef]

91. Xu, D.; Wang, H.; Qiu, R.; Wang, Q.; Mao, Z.; Jiang, Y.; Wang, R.; He, B.; Gong, Y.; Li, D.; et al. Coupling of bowl-like VS_2 nanosheet arrays and carbon nanofiber enables ultrafast Na+-Storage and robust flexibility for sodium-ion hybrid capacitors. *Energy Storage Mater.* **2020**, *28*, 91–100. [CrossRef]

92. Liu, J.; Xu, Y.-G.; Kong, L.-B. High-capacity and fast Na-ion diffusion rate three-dimensional MoS_2/SnS_2-RGO anode for advanced sodium-ion batteries and sodium-ion capacitors. *Solid State Ionics* **2020**, *355*, 115416. [CrossRef]

93. Liu, C.; Zhang, M.; Zhang, X.; Wan, B.; Li, X.; Gou, H.; Wang, Y.; Yin, F.; Wang, G. 2D Sandwiched Nano Heterostructures Endow $MoSe_2$/TiO_2−x/Graphene with High Rate and Durability for Sodium Ion Capacitor and Its Solid Electrolyte Interphase Dependent Sodiation/Desodiation Mechanism. *Small* **2020**, *16*, 2004457. [CrossRef] [PubMed]

94. Shen, Q.; Jiang, P.; He, H.; Chen, C.; Liu, Y.; Zhang, M. Encapsulation of MoSe2 in carbon fibers as anodes for potassium ion batteries and nonaqueous battery–supercapacitor hybrid devices. *Nanoscale* **2019**, *11*, 13511–13520. [CrossRef] [PubMed]

95. Yi, Y.; Sun, Z.; Li, C.; Tian, Z.; Lu, C.; Shao, Y.; Li, J.; Sun, J.; Liu, Z. Designing 3D Biomorphic Nitrogen-Doped MoSe2/Graphene Composites toward High-Performance Potassium-Ion Capacitors. *Adv. Funct. Mater.* **2020**, *30*, 1903878. [CrossRef]

96. Huang, K.J.; Wang, L.; Liu, Y.J.; Liu, Y.M.; Wang, H.B.; Gan, T.; Wang, L.L. Layered MoS2-graphene composites for supercapacitor applications with enhanced capacitive performance. *Int. J. Hydrogen Energy* **2013**, *38*, 14027–14034. [CrossRef]

97. Huang, K.J.; Wang, L.; Zhang, J.Z.; Xing, K. Synthesis of molybdenum disulfide/carbon aerogel composites for supercapacitors electrode material application. *J. Electroanal. Chem.* **2015**, *752*, 33–40. [CrossRef]

98. Wang, L.; Ma, Y.; Yang, M.; Qi, Y. Hierarchical hollow MoS_2 nanospheres with enhanced electrochemical properties used as an Electrode in Supercapacitor. *Electrochim. Acta* **2015**, *186*, 391–396. [CrossRef]

99. Gigot, A.; Fontana, M.; Serrapede, M.; Castellino, M.; Bianco, S.; Armandi, M.; Bonelli, B.; Pirri, C.F.; Tresso, E.; Rivolo, P. Mixed 1T-2H Phase MoS2/Reduced Graphene Oxide as Active Electrode for Enhanced Supercapacitive Performance. *ACS Appl. Mater. Interfaces* **2016**, *8*, 32842–32852. [CrossRef]

100. Liang, X.; Nie, K.; Ding, X.; Dang, L.; Sun, J.; Shi, F.; Xu, H.; Jiang, R.; He, X.; Liu, Z.; et al. Highly Compressible Carbon Sponge Supercapacitor Electrode with Enhanced Performance by Growing Nickel-Cobalt Sulfide Nanosheets. *ACS Appl. Mater. Interfaces* **2018**, *10*, 10087–10095. [CrossRef]

101. Tang, J.; Shen, J.; Li, N.; Ye, M. A free template strategy for the synthesis of CoS_2-reduced graphene oxide nanocomposite with enhanced electrode performance for supercapacitors. *Ceram. Int.* **2014**, *40*, 15411–15419. [CrossRef]

102. Huang, K.J.; Zhang, J.Z.; Liu, Y.; Liu, Y.M. Synthesis of reduced graphene oxide wrapped-copper sulfide hollow spheres as electrode material for supercapacitor. *Int. J. Hydrogen Energy* **2015**, *40*, 10158–10167. [CrossRef]

103. Zhao, T.; Yang, W.; Zhao, X.; Peng, X.; Hu, J.; Tang, C.; Li, T. Facile preparation of reduced graphene oxide/copper sulfide composite as electrode materials for supercapacitors with high energy density. *Compos. Part B Eng.* **2018**, *150*, 60–67. [CrossRef]

104. Xiao, W.; Zhou, W.; Feng, T.; Zhang, Y.; Liu, H.; Yu, H.; Tian, L.; Pu, Y. One-pot solvothermal synthesis of flower-like copper sulfide/reduced graphene oxide composite superstructures as high-performance supercapacitor electrode materials. *J. Mater. Sci. Mater. Electron.* **2017**, *28*, 5931–5940. [CrossRef]

105. Boopathiraja, R.; Parthibavarman, M.; Prabhu, S.; Ramesh, R. A facile one step hydrothermal induced hexagonal shaped CuS/rGO nanocomposites for asymmetric supercapacitors. *Mater. Today Proc.* **2019**, *26*, 3507–3513. [CrossRef]

106. Wang, Y.; Zhang, W.; Guo, X.; Jin, K.; Chen, Z.; Liu, Y.; Yin, L.; Li, L.; Yin, K.; Sun, L.; et al. Ni-Co Selenide Nanosheet/3D Graphene/Nickel Foam Binder-Free Electrode for High-Performance Supercapacitor. *ACS Appl. Mater. Interfaces* **2019**, *11*, 7946–7953. [CrossRef]

107. Amin, B.G.; Masud, J.; Nath, M. Facile one-pot synthesis of NiCo2Se4-rGO on Ni foam for high performance hybrid supercapacitors. *RSC Adv.* **2019**, *9*, 37939–37946. [CrossRef]

108. Ghosh, S.; Samanta, P.; Samanta, P.; Murmu, N.C.; Kuila, T. Investigation of Electrochemical Charge Storage Efficiency of $NiCo_2Se_4$/RGO Composites Derived at Varied Duration and Its Asymmetric Supercapacitor Device. *Energy Fuels* **2020**, *34*, 13056–13066. [CrossRef]

109. Zhang, K.; Wei, Y.; Huang, J.; Xiao, Y.; Yang, W.; Hu, T.; Yuan, K.; Chen, Y. A generalized one-step in situ formation of metal sulfide/reduced graphene oxide nanosheets toward high-performance supercapacitors. *Sci. China Mater.* **2020**, *63*, 1898–1909. [CrossRef]

110. Sarkar, S.; Howli, P.; Das, B.; Das, N.S.; Samanta, M.; Das, G.C.; Chattopadhyay, K.K. Novel Quaternary Chalcogenide/Reduced Graphene Oxide-Based Asymmetric Supercapacitor with High Energy Density. *ACS Appl. Mater. Interfaces* **2017**, *9*, 22652–22664. [CrossRef]

111. Huang, K.J.; Wang, L.; Zhang, J.Z.; Wang, L.L.; Mo, Y.P. One-step preparation of layered molybdenum disulfide/multi-walled carbon nanotube composites for enhanced performance supercapacitor. *Energy* **2014**, *67*, 234–240. [CrossRef]

112. Sun, P.; Wang, R.; Wang, Q.; Wang, H.; Wang, X. Uniform MoS_2 nanolayer with sulfur vacancy on carbon nanotube networks as binder-free electrodes for asymmetrical supercapacitor. *Appl. Surf. Sci.* **2019**, *475*, 793–802. [CrossRef]

113. Huang, K.J.; Zhang, J.Z.; Xing, K. One-step synthesis of layered CuS/multi-walled carbon nanotube nanocomposites for supercapacitor electrode material with ultrahigh specific capacitance. *Electrochim. Acta* **2014**, *149*, 28–33. [CrossRef]

114. Lu, Y.; Liu, X.; Wang, W.; Cheng, J.; Yan, H.; Tang, C.; Kim, J.K.; Luo, Y. Hierarchical, porous CuS microspheres integrated with carbon nanotubes for high-performance supercapacitors. *Sci. Rep.* **2015**, *5*, 16584. [CrossRef] [PubMed]

115. Hou, X.; Liu, X.; Lu, Y.; Cheng, J.; Luo, R.; Yu, Q.; Wei, X.; Yan, H.; Ji, X.; Kim, J.K.; et al. Copper sulfide nanoneedles on CNT backbone composite electrodes for high-performance supercapacitors and Li-S batteries. *J. Solid State Electrochem.* **2017**, *21*, 349–359. [CrossRef]

116. Muralee Gopi, C.V.V.; Ravi, S.; Rao, S.S.; Eswar Reddy, A.; Kim, H.J. Carbon nanotube/metal-sulfide composite flexible electrodes for high-performance quantum dot-sensitized solar cells and supercapacitors. *Sci. Rep.* **2017**, *7*, 46519. [CrossRef] [PubMed]

117. Azad, M.; Hussain, Z.; Baig, M.M. MWCNTs/NiS_2 decorated Ni foam based electrode for high-performance supercapacitors. *Electrochim. Acta* **2020**, *345*, 136196. [CrossRef]

118. Ma, X.; Kang, Z. A facile electrodeposition technique for synthesis of nickel sulfides/carbon nanotubes nanocomposites as high performance electrodes for supercapacitor. *Mater. Lett.* **2019**, *236*, 468–471. [CrossRef]

119. Pandit, B.; Karade, S.S.; Sankapal, B.R. Hexagonal VS_2 Anchored MWCNTs: First Approach to Design Flexible Solid-State Symmetric Supercapacitor Device. *ACS Appl. Mater. Interfaces* **2017**, *9*, 44880–44891. [CrossRef]

120. Zang, X.; Shen, C.; Kao, E.; Warren, R.; Zhang, R.; Teh, K.S.; Zhong, J.; Wei, M.; Li, B.; Chu, Y.; et al. Titanium Disulfide Coated Carbon Nanotube Hybrid Electrodes Enable High Energy Density Symmetric Pseudocapacitors. *Adv. Mater.* **2018**, *30*, 1704754. [CrossRef]

121. Chen, H.; Li, J.; Long, C.; Wei, T.; Ning, G.; Yan, J.; Fan, Z. Nickel sulfide/graphene/carbon nanotube composites as electrode material for the supercapacitor application in the sea flashing signal system. *J. Mar. Sci. Appl.* **2014**, *13*, 462–466. [CrossRef]

122. Yang, W.; He, L.; Tian, X.; Yan, M.; Yuan, H.; Liao, X.; Meng, J.; Hao, Z.; Mai, L. Carbon-MEMS-Based Alternating Stacked MoS_2@rGO-CNT Micro-Supercapacitor with High Capacitance and Energy Density. *Small* **2017**, *13*, 1700639. [CrossRef] [PubMed]

123. Lee, H.; Choi, J.; Myung, Y.; Lee, S.M.; Kim, H.J.; Ko, Y.J.; Yang, M.; Son, S.U. Yolk-Shell Polystyrene@Microporous Organic Network: A Smart Template with Thermally Disassemblable Yolk to Engineer Hollow MoS_2/C Composites for High-Performance Supercapacitors. *ACS Omega* **2017**, *2*, 7658–7665. [CrossRef] [PubMed]

124. Yan, Z.S.; Long, J.Y.; Zhou, Q.F.; Gong, Y.; Lin, J.H. One-step synthesis of MnS/MoS_2/C through the calcination and sulfurization of a bi-metal-organic framework for a high-performance supercapacitor and its photocurrent investigation. *Dalt. Trans.* **2018**, *47*, 5390–5405. [CrossRef]

125. Miao, C.; Xiao, X.; Gong, Y.; Zhu, K.; Cheng, K.; Ye, K.; Yan, J.; Cao, D.; Wang, G.; Xu, P. Facile Synthesis of Metal-Organic Framework-Derived CoSe2 Nanoparticles Embedded in the N-Doped Carbon Nanosheet Array and Application for Supercapacitors. *ACS Appl. Mater. Interfaces* **2020**, *12*, 9365–9375. [CrossRef] [PubMed]

126. Li, Q.; Lu, W.; Li, Z.; Ning, J.; Zhong, Y.; Hu, Y. Hierarchical MoS_2/$NiCo_2S_4$@C urchin-like hollow microspheres for asymmetric supercapacitors. *Chem. Eng. J.* **2020**, *380*, 122544. [CrossRef]

127. Kshetri, T.; Singh, T.I.; Lee, Y.S.; Khumujam, D.D.; Kim, N.H.; Lee, J.H. Metal organic framework-derived cobalt telluride-carbon porous structured composites for high-performance supercapacitor. *Compos. Part B Eng.* **2021**, *211*, 108624. [CrossRef]

128. Shi, Z.; Yue, L.; Wang, X.; Lei, X.; Sun, T.; Li, Q.; Guo, H.; Yang, W. 3D mesoporous hemp-activated carbon/Ni_3S_2 in preparation of a binder-free Ni foam for a high performance all-solid-state asymmetric supercapacitor. *J. Alloys Compd.* **2019**, *791*, 665–673. [CrossRef]

129. Zhai, S.; Fan, Z.; Jin, K.; Zhou, M.; Zhao, H.; Zhao, Y.; Ge, F. Synthesis of zinc sulfide/copper sulfide/porous carbonized cotton nanocomposites for flexible supercapacitor and recyclable photocatalysis with high performance. *J. Colloid Interface Sci.* **2020**, *575*, 306–316. [CrossRef]

130. Yang, M.; Jeong, J.; Suk, Y.; Gill, B. High-performance supercapacitor based on three-dimensional MoS$_2$/graphene aerogel composites. *Compos. Sci. Technol.* **2015**, *121*, 123–128. [CrossRef]
131. Li, P.; Jeong, J.Y.; Jin, B.; Zhang, K.; Park, J.H. Vertically Oriented MoS$_2$ with Spatially Controlled Geometry on Nitrogenous Graphene Sheets for High-Performance Sodium-Ion Batteries. *Adv. Energy Mater.* **2018**, *8*, 1703300. [CrossRef]
132. Cui, C.; Wei, Z.; Xu, J.; Zhang, Y.; Liu, S.; Liu, H.; Mao, M.; Wang, S.; Ma, J.; Dou, S. Three-dimensional carbon frameworks enabling MoS$_2$ as anode for dual ion batteries with superior sodium storage properties. *Energy Storage Mater.* **2018**, *15*, 22–30. [CrossRef]
133. Zhao, Z.H.; Hu, X.D.; Wang, H.; Ye, M.Y.; Sang, Z.Y.; Ji, H.M.; Li, X.L.; Dai, Y. Superelastic 3D few-layer MoS2/carbon framework heterogeneous electrodes for highly reversible sodium-ion batteries. *Nano Energy* **2018**, *48*, 526–535. [CrossRef]
134. Liu, Y.; He, X.; Hanlon, D.; Harvey, A.; Coleman, J.N.; Li, Y. Liquid Phase Exfoliated MoS$_2$ Nanosheets Percolated with Carbon Nanotubes for High Volumetric/Areal Capacity Sodium-Ion Batteries. *ACS Nano* **2016**, *10*, 8821–8828. [CrossRef] [PubMed]
135. Cai, Y.; Yang, H.; Zhou, J.; Luo, Z.; Fang, G.; Liu, S.; Pan, A.; Liang, S. Nitrogen doped hollow MoS$_2$/C nanospheres as anode for long-life sodium-ion batteries. *Chem. Eng. J.* **2017**, *327*, 522–529. [CrossRef]
136. Sun, D.; Ye, D.; Liu, P.; Tang, Y.; Guo, J.; Wang, L.; Wang, H. MoS$_2$/Graphene Nanosheets from Commercial Bulky MoS2 and Graphite as Anode Materials for High Rate Sodium-Ion Batteries. *Adv. Energy Mater.* **2018**, *8*, 1702383. [CrossRef]
137. Li, G.; Luo, D.; Wang, X.; Seo, M.H.; Hemmati, S.; Yu, A.; Chen, Z. Enhanced Reversible Sodium-Ion Intercalation by Synergistic Coupling of Few-Layered MoS$_2$ and S-Doped Graphene. *Adv. Funct. Mater.* **2017**, *27*, 1702562. [CrossRef]
138. Kong, D.; Cheng, C.; Wang, Y.; Huang, Z.; Liu, B.; Von Lim, Y.; Ge, Q.; Yang, H.Y. Fe$_3$O$_4$ quantum dot decorated MoS2 nanosheet arrays on graphite paper as free-standing sodium-ion battery anodes. *J. Mater. Chem. A* **2017**, *5*, 9122–9131. [CrossRef]
139. Geng, X.; Jiao, Y.; Han, Y.; Mukhopadhyay, A.; Yang, L.; Zhu, H. Freestanding Metallic 1T MoS$_2$ with Dual Ion Diffusion Paths as High Rate Anode for Sodium-Ion Batteries. *Adv. Funct. Mater.* **2017**, *27*, 1702998. [CrossRef]
140. Li, X.; Yang, Y.; Liu, J.; Ouyang, L.; Liu, J.; Hu, R.; Yang, L.; Zhu, M. MoS$_2$/cotton-derived carbon fibers with enhanced cyclic performance for sodium-ion batteries. *Appl. Surf. Sci.* **2017**, *413*, 169–174. [CrossRef]
141. Wang, L.; Yang, G.; Wang, J.; Peng, S.; Yan, W.; Ramakrishna, S. Controllable Design of MoS$_2$ Nanosheets Grown on Nitrogen-Doped Branched TiO$_2$/C Nanofibers: Toward Enhanced Sodium Storage Performance Induced by Pseudocapacitance Behavior. *Small* **2020**, *16*, 1904589. [CrossRef]
142. Pang, Y.; Zhang, S.; Liu, L.; Liang, J.; Sun, Z.; Wang, Y.; Xiao, C.; Ding, D.; Ding, S. Few-layer MoS$_2$ anchored at nitrogen-doped carbon ribbons for sodium-ion battery anodes with high rate performance. *J. Mater. Chem. A* **2017**, *5*, 17963–17972. [CrossRef]
143. Zhang, Y.; Yu, S.; Wang, H.; Zhu, Z.; Liu, Q.; Xu, E.; Li, D.; Tong, G.; Jiang, Y. A novel carbon-decorated hollow flower-like MoS2 nanostructure wrapped with RGO for enhanced sodium-ion storage. *Chem. Eng. J.* **2018**, *343*, 180–188. [CrossRef]
144. Ye, H.; Wang, L.; Deng, S.; Zeng, X.; Nie, K.; Duchesne, P.N.; Wang, B.; Liu, S.; Zhou, J.; Zhao, F.; et al. Amorphous MoS$_3$ Infiltrated with Carbon Nanotubes as an Advanced Anode Material of Sodium-Ion Batteries with Large Gravimetric, Areal, and Volumetric Capacities. *Adv. Energy Mater.* **2017**, *7*, 1601602. [CrossRef]
145. Niu, F.; Yang, J.; Wang, N.; Zhang, D.; Fan, W.; Yang, J.; Qian, Y. MoSe$_2$-Covered N,P-Doped Carbon Nanosheets as a Long-Life and High-Rate Anode Material for Sodium-Ion Batteries. *Adv. Funct. Mater.* **2017**, *27*, 1700522. [CrossRef]
146. Zhang, Z.; Yang, X.; Fu, Y.; Du, K. Ultrathin molybdenum diselenide nanosheets anchored on multi-walled carbon nanotubes as anode composites for high performance sodium-ion batteries. *J. Power Source* **2015**, *296*, 2–9. [CrossRef]
147. Wang, S.; Gong, F.; Yang, S.; Liao, J.; Wu, M.; Xu, Z.; Chen, C.; Yang, X.; Zhao, F.; Wang, B.; et al. Graphene Oxide-Template Controlled Cuboid-Shaped High-Capacity VS$_4$ Nanoparticles as Anode for Sodium-Ion Batteries. *Adv. Funct. Mater.* **2018**, *28*, 1801806. [CrossRef]
148. Sun, R.; Wei, Q.; Li, Q.; Luo, W.; An, Q.; Sheng, J.; Wang, D.; Chen, W.; Mai, L. Vanadium Sulfide on Reduced Graphene Oxide Layer as a Promising Anode for Sodium Ion Battery. *ACS Appl. Mater. Interfaces* **2015**, *7*, 20902–20908. [CrossRef]
149. Zhang, Y.; Wang, N.; Xue, P.; Liu, Y.; Tang, B.; Bai, Z.; Dou, S. Co$_9$S$_8$@carbon nanospheres as high-performance anodes for sodium ion battery. *Chem. Eng. J.* **2018**, *343*, 512–519. [CrossRef]
150. Pan, Y.; Cheng, X.; Huang, Y.; Gong, L.; Zhang, H. CoS2 Nanoparticles Wrapping on Flexible Freestanding Multichannel Carbon Nanofibers with High Performance for Na-Ion Batteries. *ACS Appl. Mater. Interfaces* **2017**, *9*, 35820–35828. [CrossRef]
151. Freitas, F.S.; Gonçalves, A.S.; De Morais, A.; Benedetti, J.E.; Nogueira, A.F. Graphene-like MoS$_2$ as a low-cost counter electrode material for dye-sensitized solar cells. *NanoGe J. Energy Sustain.* **2012**, 11002–11003.
152. Yao, S.; Cui, J.; Lu, Z.; Xu, Z.L.; Qin, L.; Huang, J.; Sadighi, Z.; Ciucci, F.; Kim, J.K. Unveiling the Unique Phase Transformation Behavior and Sodiation Kinetics of 1D van der Waals Sb$_2$S$_3$ Anodes for Sodium Ion Batteries. *Adv. Energy Mater.* **2017**, *7*, 1602149. [CrossRef]
153. Xiong, X.; Wang, G.; Lin, Y.; Wang, Y.; Ou, X.; Zheng, F.; Yang, C.; Wang, J.H.; Liu, M. Enhancing Sodium Ion Battery Performance by Strongly Binding Nanostructured Sb$_2$S$_3$ on Sulfur-Doped Graphene Sheets. *ACS Nano* **2016**, *10*, 10953–10959. [CrossRef] [PubMed]
154. Dong, S.; Li, C.; Ge, X.; Li, Z.; Miao, X.; Yin, L. ZnS-Sb2S3@C Core-Double Shell Polyhedron Structure Derived from Metal-Organic Framework as Anodes for High Performance Sodium Ion Batteries. *ACS Nano* **2017**, *11*, 6474–6482. [CrossRef]
155. Ge, P.; Cao, X.; Hou, H.; Li, S.; Ji, X. Rodlike Sb2Se3 Wrapped with Carbon: The Exploring of Electrochemical Properties in Sodium-Ion Batteries. *ACS Appl. Mater. Interfaces* **2017**, *9*, 34979–34989. [CrossRef] [PubMed]

156. Luo, W.; Calas, A.; Tang, C.; Li, F.; Zhou, L.; Mai, L. Ultralong Sb$_2$Se$_3$ Nanowire-Based Free-Standing Membrane Anode for Lithium/Sodium Ion Batteries. *ACS Appl. Mater. Interfaces* **2016**, *8*, 35219–35226. [CrossRef]

157. Xiong, X.; Yang, C.; Wang, G.; Lin, Y.; Ou, X.; Wang, J.H.; Zhao, B.; Liu, M.; Lin, Z.; Huang, K. SnS nanoparticles electrostatically anchored on three-dimensional N-doped graphene as an active and durable anode for sodium-ion batteries. *Energy Environ. Sci.* **2017**, *10*, 1757–1763. [CrossRef]

158. Lin, Y.; Qiu, Z.; Li, D.; Ullah, S.; Hai, Y.; Xin, H.; Liao, W.; Yang, B.; Fan, H.; Xu, J.; et al. NiS$_2$@CoS$_2$ nanocrystals encapsulated in N-doped carbon nanocubes for high performance lithium/sodium ion batteries. *Energy Storage Mater.* **2018**, *11*, 67–74. [CrossRef]

159. Jiang, Y.; Wei, M.; Feng, J.; Ma, Y.; Xiong, S. Enhancing the cycling stability of Na-ion batteries by bonding SnS$_2$ ultrafine nanocrystals on amino-functionalized graphene hybrid nanosheets. *Energy Environ. Sci.* **2016**, *9*, 1430–1438. [CrossRef]

160. Gao, S.; Chen, G.; Dall'Agnese, Y.; Wei, Y.; Gao, Z.; Gao, Y. Flexible MnS–Carbon Fiber Hybrids for Lithium-Ion and Sodium-Ion Energy Storage. *Chem.-A Eur. J.* **2018**, *24*, 13535–13539. [CrossRef]

161. Wu, T.H.; Lin, Y.C.; Hou, B.W.; Liang, W.Y. Nanostructured β−NiS catalyst for enhanced and stable electro−oxidation of urea. *Catalysts* **2020**, *10*, 1280. [CrossRef]

162. Liu, M.; Jiao, Y.; Zhan, S.; Wang, H. Ni$_3$S$_2$ nanowires supported on Ni foam as efficient bifunctional electrocatalyst for urea-assisted electrolytic hydrogen production. *Catal. Today* **2020**, *355*, 596–601. [CrossRef]

163. Hao, P.; Zhu, W.; Li, L.; Tian, J.; Xie, J.; Lei, F.; Cui, G.; Zhang, Y.; Tang, B. Nickel incorporated Co$_9$S$_8$ nanosheet arrays on carbon cloth boosting overall urea electrolysis. *Electrochim. Acta* **2020**, *338*, 135883. [CrossRef]

164. Khalafallah, D.; Zou, Q.; Zhi, M.; Hong, Z. Tailoring hierarchical yolk-shelled nickel cobalt sulfide hollow cages with carbon tuning for asymmetric supercapacitors and efficient urea electrocatalysis. *Electrochim. Acta* **2020**, *350*, 136399. [CrossRef]

165. Yang, M.; Ding, C.; Liu, Y.; Bai, Q. Enhanced electro-oxidation of urea using Ni-NiS debris via confinement in carbon derived from glucose. *Colloids Surf. A Physicochem. Eng. Asp.* **2021**, *618*, 126425. [CrossRef]

166. He, M.; Hu, S.; Feng, C.; Wu, H.; Liu, H.; Mei, H. Interlaced rosette-like MoS$_2$/Ni$_3$S$_2$/NiFe-LDH grown on nickel foam: A bifunctional electrocatalyst for hydrogen production by urea-assisted electrolysis. *Int. J. Hydrogen Energy* **2020**, *45*, 23–35. [CrossRef]

167. Xiong, P.; Ao, X.; Chen, J.; Li, J.G.; Lv, L.; Li, Z.; Zondode, M.; Xue, X.; Lan, Y.; Wang, C. Nickel diselenide nanoflakes give superior urea electrocatalytic conversion. *Electrochim. Acta* **2019**, *297*, 833–841. [CrossRef]

168. Liu, X.; Liu, Y.; Fan, L.Z. MOF-derived CoSe$_2$ microspheres with hollow interiors as high-performance electrocatalysts for the enhanced oxygen evolution reaction. *J. Mater. Chem. A* **2017**, *5*, 15310–15314. [CrossRef]

169. Liu, T.; Sun, X.; Asiri, A.M.; He, Y. One-step electrodeposition of Ni-Co-S nanosheets film as a bifunctional electrocatalyst for efficient water splitting. *Int. J. Hydrogen Energy* **2016**, *41*, 7264–7269. [CrossRef]

170. Zhao, X.; Li, X.; Yan, Y.; Xing, Y.; Lu, S.; Zhao, L.; Zhou, S.; Peng, Z.; Zeng, J. Electrical and structural engineering of cobalt selenide nanosheets by Mn modulation for efficient oxygen evolution. *Appl. Catal. B Environ.* **2018**, *236*, 569–575. [CrossRef]

171. Yu, J.; Tian, Y.; Zhou, F.; Zhang, M.; Chen, R.; Liu, Q.; Liu, J.; Xu, C.Y.; Wang, J. Metallic and superhydrophilic nickel cobalt diselenide nanosheets electrodeposited on carbon cloth as a bifunctional electrocatalyst. *J. Mater. Chem. A* **2018**, *6*, 17353–17360. [CrossRef]

172. Chi, J.Q.; Yan, K.L.; Xiao, Z.; Dong, B.; Shang, X.; Gao, W.K.; Li, X.; Chai, Y.M.; Liu, C.G. Trimetallic Ni–Fe–Co selenides nanoparticles supported on carbon fiber cloth as efficient electrocatalyst for oxygen evolution reaction. *Int. J. Hydrogen Energy* **2017**, *42*, 20599–20607. [CrossRef]

173. Yao, M.; Hu, H.; Sun, B.; Wang, N.; Hu, W.; Komarneni, S. Self-Supportive Mesoporous Ni/Co/Fe Phosphosulfide Nanorods Derived from Novel Hydrothermal Electrodeposition as a Highly Efficient Electrocatalyst for Overall Water Splitting. *Small* **2019**, *15*, 1905201. [CrossRef] [PubMed]

174. Jiang, Y.F.; Yuan, C.Z.; Zhou, X.; Liu, Y.N.; Zhao, Z.W.; Zhao, S.J.; Xu, A.W. Selenium phosphorus co-doped cobalt oxide nanosheets anchored on Co foil: A self-supported and stable bifunctional electrode for efficient electrochemical water splitting. *Electrochim. Acta* **2018**, *292*, 247–255. [CrossRef]

175. Li, J.G.; Xie, K.; Sun, H.; Li, Z.; Ao, X.; Chen, Z.; Ostrikov, K.K.; Wang, C.; Zhang, W. Template-Directed Bifunctional Dodecahedral CoP/CN@MoS2 Electrocatalyst for High Efficient Water Splitting. *ACS Appl. Mater. Interfaces* **2019**, *11*, 36649–36657. [CrossRef] [PubMed]

176. Deng, S.; Shen, S.; Zhong, Y.; Zhang, K.; Wu, J.; Wang, X.; Xia, X.; Tu, J. Assembling Co$_9$S$_8$ nanoflakes on Co3O4 nanowires as advanced core/shell electrocatalysts for oxygen evolution reaction. *J. Energy Chem.* **2017**, *26*, 1203–1209. [CrossRef]

177. Muthurasu, A.; Maruthapandian, V.; Kim, H.Y. Metal-organic framework derived Co$_3$O$_4$/MoS$_2$ heterostructure for efficient bifunctional electrocatalysts for oxygen evolution reaction and hydrogen evolution reaction. *Appl. Catal. B Environ.* **2019**, *248*, 202–210. [CrossRef]

178. Wang, S.; Xu, L.; Lu, W. Synergistic effect: Hierarchical Ni$_3$S$_2$ @Co(OH)$_2$ heterostructure as efficient bifunctional electrocatalyst for overall water splitting. *Appl. Surf. Sci.* **2018**, *457*, 156–163. [CrossRef]

179. Yan, J.; Chen, L.; Liang, X. Co$_9$S$_8$ nanowires@NiCo LDH nanosheets arrays on nickel foams towards efficient overall water splitting. *Sci. Bull.* **2019**, *64*, 158–165. [CrossRef]

180. Zhan, C.; Liu, Z.; Zhou, Y.; Guo, M.; Zhang, X.; Tu, J.; Ding, L.; Cao, Y. Triple hierarchy and double synergies of NiFe/Co$_9$S$_8$/carbon cloth: A new and efficient electrocatalyst for the oxygen evolution reaction. *Nanoscale* **2019**, *11*, 3193–3199. [CrossRef]

181. Que, R.; Ji, G.; Liu, D.; Li, M.; Wang, X.; Jiang, S.P. Nickel Foam-Supported CoCO 3 @CoSe Nanowires with a Heterostructure Interface for Overall Water Splitting with Low Overpotential and High Efficiency. *Energy Technol.* **2019**, *7*, 1800741. [CrossRef]

182. Li, K.; Zhang, J.; Wu, R.; Yu, Y.; Zhang, B. Anchoring CoO domains on $CoSe_2$ nanobelts as bifunctional electrocatalysts for overall water splitting in neutral media. *Adv. Sci.* **2015**, *3*, 1500426. [CrossRef] [PubMed]

183. Yang, Y.; Yao, H.; Yu, Z.; Islam, S.M.; He, H.; Yuan, M.; Yue, Y.; Xu, K.; Hao, W.; Sun, G.; et al. Hierarchical Nanoassembly of $MoS_2/Co_9S_8/Ni_3S_2/Ni$ as a Highly Efficient Electrocatalyst for Overall Water Splitting in a Wide pH Range. *J. Am. Chem. Soc.* **2019**, *141*, 10417–10430. [CrossRef]

184. Zhang, C.; Bhoyate, S.; Kahol, P.K.; Siam, K.; Poudel, T.P.; Mishra, S.R.; Perez, F.; Gupta, A.; Gupta, G.; Gupta, R.K. Highly Efficient and Durable Electrocatalyst Based on Nanowires of Cobalt Sulfide for Overall Water Splitting. *ChemNanoMat* **2018**, *4*, 1240–1246. [CrossRef]

185. Gu, W.; Hu, L.; Zhu, X.; Shang, C.; Li, J.; Wang, E. Rapid synthesis of Co3O4 nanosheet arrays on Ni foam by in situ electrochemical oxidization of air-plasma engraved $Co(OH)_2$ for efficient oxygen evolution. *Chem. Commun.* **2018**, *54*, 12698–12701. [CrossRef] [PubMed]

186. Wu, Z.; Li, J.; Zou, Z.; Wang, X. Folded nanosheet-like Co0.85Se array for overall water splitting. *J. Solid State Electrochem.* **2018**, *22*, 1785–1794. [CrossRef]

187. Liu, S.; Jiang, Y.; Yang, M.; Zhang, M.; Guo, Q.; Shen, W.; He, R.; Li, M. Highly conductive and metallic cobalt-nickel selenide nanorods supported on Ni foam as an efficient electrocatalyst for alkaline water splitting. *Nanoscale* **2019**, *11*, 7959–7966. [CrossRef]

188. Yang, W.Q.; Hua, Y.X.; Zhang, Q.B.; Lei, H.; Xu, C.Y. Electrochemical fabrication of 3D quasi-amorphous pompon-like Co-O and Co-Se hybrid films from choline chloride/urea deep eutectic solvent for efficient overall water splitting. *Electrochim. Acta* **2018**, *273*, 71–79. [CrossRef]

189. Gao, Q.; Wang, X.; Shi, Z.; Ye, Z.; Wang, W.; Zhang, N.; Hong, Z.; Zhi, M. Synthesis of porous $NiCo_2S_4$ aerogel for supercapacitor electrode and oxygen evolution reaction electrocatalyst. *Chem. Eng. J.* **2018**, *331*, 185–193. [CrossRef]

190. Shi, Y.; Yang, B.; Guo, X.; Wu, X.; Pang, H. Copper sulfides and their composites for high-performance rechargeable batteries. *Mater. Today Chem.* **2022**, *23*, 100675. [CrossRef]

191. Li, Y.; Wu, F.; Qian, J.; Zhang, M.; Yuan, Y.; Bai, Y.; Wu, C. Metal Chalcogenides with Heterostructures for High-Performance Rechargeable Batteries. *Small Sci.* **2021**, *1*, 2100012. [CrossRef]

192. Fang, Y.; Luan, D.; Lou, X.W. Recent Advances on Mixed Metal Sulfides for Advanced Sodium-Ion Batteries. *Adv. Mater.* **2020**, *32*, 2002976. [CrossRef] [PubMed]

193. Xu, X.; Hui, K.S.; Hui, K.N.; Shen, J.; Zhou, G.; Liu, J.; Sun, Y. Engineering strategies for low-cost and high-power density aluminum-ion batteries. *Chem. Eng. J.* **2021**, *418*, 129385. [CrossRef]

194. Yu, J.; Tang, T.; Cheng, F.; Huang, D.; Martin, J.L.; Brewer, C.E.; Grimm, R.L.; Zhou, M.; Luo, H. Exploring spent biomass-derived adsorbents as anodes for lithium ion batteries. *Mater. Today Energy* **2021**, *19*, 100580. [CrossRef]

195. Li, Z.; Liu, H.; Huang, J.; Zhang, L. MOF-derived α-MnSe/C composites as anode materials for Li-ion batteries. *Ceram. Int.* **2019**, *45*, 23765–23771. [CrossRef]

196. Han, X.; Ai, F.; Wang, X.; Chen, B.; Wang, L.; Bi, Y. Thiacalixarene-supported Co_{24} nanocluster derived octahedral Co_9S_8 nanoparticles in N-doped carbon for superior Li-ion storage. *Polyhedron* **2019**, *171*, 279–284. [CrossRef]

197. Tran Huu, H.; Le, H.T.T.; Huong Nguyen, T.; Nguyen Thi, L.; Vo, V.; Bin Im, W. Facile synthesis of $SnS_2@g-C_3N_4$ composites as high performance anodes for lithium ion batteries. *Appl. Surf. Sci.* **2021**, *549*, 149312. [CrossRef]

198. Lee, S.; Kim, S.; Gim, J.; Alfaruqi, M.H.; Kim, S.; Mathew, V.; Sambandam, B.; Hwang, J.Y.; Kim, J. Ultra-small ZnS quantum dots embedded in N-doped carbon matrix for high-performance Li-ion battery anode. *Compos. Part B Eng.* **2022**, *231*, 109548. [CrossRef]

199. Zhou, Y.; Tian, R.; Duan, H.; Wang, K.; Guo, Y.; Li, H.; Liu, H. CoSe/Co nanoparticles wrapped by in situ grown N-doped graphitic carbon nanosheets as anode material for advanced lithium ion batteries. *J. Power Source* **2018**, *399*, 223–230. [CrossRef]

200. Wang, S.; Yang, X.; Lee, P.; Yu, D.Y.W. Mechanically and structurally stable Sb_2Se_3/carbon nanocomposite as anode for the lithium-ion batteries. *J. Alloys Compd.* **2021**, *874*, 159859. [CrossRef]

201. Chen, H.; Liu, R.; Wu, Y.; Cao, J.; Chen, J.; Hou, Y.; Guo, Y.; Khatoon, R.; Chen, L.; Zhang, Q.; et al. Interface coupling 2D/2D $SnSe_2$/graphene heterostructure as long-cycle anode for all-climate lithium-ion battery. *Chem. Eng. J.* **2021**, *407*, 126973. [CrossRef]

202. Huang, Y.; Lin, W.; Shi, C.; Li, L.; Fan, K.; Huang, X.; Wu, X.; Du, K. Misfit layer $SnTiS_3$: An assemble-free van der Waals heterostructure SnS/TiS_2 for lithium ion battery anode. *J. Power Source* **2021**, *494*, 229712. [CrossRef]

203. Xu, H.; Sun, L.; Li, W.; Gao, M.; Zhou, Q.; Li, P.; Yang, S.; Lin, J. Facile synthesis of hierarchical $g-C_3N_4@WS_2$ composite as Lithium-ion battery anode. *Chem. Eng. J.* **2022**, *435*, 135129. [CrossRef]

204. Zhu, Y.; Zhao, J.; Li, L.; Mao, J.; Xu, J.; Jin, J. One-step solvothermal synthesis of $BiSbTe_3$/N-doped reduced graphene oxide composite as lithium-ion batteries anode materials. *Chem. Eng. Sci.* **2020**, *225*, 115829. [CrossRef]

205. So, S.; Ko, J.; Ahn, Y.N.; Kim, I.T.; Hur, J. Unraveling improved electrochemical kinetics of In_2Te_3-based anodes embedded in hybrid matrix for Li-ion batteries. *Chem. Eng. J.* **2022**, *429*, 132395. [CrossRef]

206. Liang, Z.; Tu, H.; Zhang, K.; Kong, Z.; Huang, M.; Xu, D. Self-supporting $NiSe_2$ @ BCNNTs electrode for High-Performance sodium ion batteries. *Chem. Eng. J.* **2022**, *437*, 135421. [CrossRef]

207. Sun, Y.; Yang, Y.; Shi, X.L.; Suo, G.; Chen, H.; Noman, M.; Tao, X.; Chen, Z.G. Hierarchical SnS_2/carbon nanotube@reduced graphene oxide composite as an anode for ultra-stable sodium-ion batteries. *Chem. Eng. J. Adv.* **2020**, *4*, 100053. [CrossRef]

208. Zheng, F.; Zhong, W.; Deng, Q.; Pan, Q.; Ou, X.; Liu, Y.; Xiong, X.; Yang, C.; Chen, Y.; Liu, M. Three-dimensional (3D) flower-like MoSe$_2$/N-doped carbon composite as a long-life and high-rate anode material for sodium-ion batteries. *Chem. Eng. J.* **2019**, *357*, 226–236. [CrossRef]

209. Lu, Z.; Wang, W.; Zhou, J.; Bai, Z. FeS$_2$@TiO$_2$ nanorods as high-performance anode for sodium ion battery. *Chin. J. Chem. Eng.* **2020**, *28*, 2699–2706. [CrossRef]

210. Li, W.; Huang, J.; Li, R.; Cao, L.; Li, X.; Feng, L. (1 1 0)-Bridged nanoblocks self-assembled VS$_4$ hollow microspheres as sodium-ion battery anode with superior rate capability and long cycling life. *Chem. Eng. J.* **2020**, *384*, 123385. [CrossRef]

211. Luo, Y.; Zhang, P.; Xiong, X.; Fu, H. Self-assembled MoS$_2$/C nanoflowers with expanded interlayer spacing as a high-performance anode for sodium ion batteries. *Chin. J. Chem. Eng.* **2021**, *39*, 240–246. [CrossRef]

212. Ye, L.; Wang, W.; Zhang, B.; Li, D.; Xiao, H.; Xiao, Z.; Ming, L.; Ou, X. Regeneration of well-performed anode material for sodium ion battery from waste lithium cobalt oxide via a facile sulfuration process. *Mater. Today Energy* **2022**, *25*, 100957. [CrossRef]

213. Shao, L.; Wang, S.; Qi, J.; Sun, Z.; Shi, X.; Shi, Y.; Lu, X. Highly infiltrative micro-sized Cu$_2$Se as advanced material with excellent rate performance and ultralong cycle-life for sodium ion half/full batteries. *Mater. Today Phys.* **2021**, *19*, 100422. [CrossRef]

214. Young Jeong, S.; Ghosh, S.; Kim, J.K.; Kang, D.W.; Mun Jeong, S.; Chan Kang, Y.; Cho, J.S. Multi-channel-contained few-layered MoSe$_2$ nanosheet/N-doped carbon hybrid nanofibers prepared using diethylenetriamine as anodes for high-performance sodium-ion batteries. *J. Ind. Eng. Chem.* **2019**, *75*, 100–107. [CrossRef]

215. He, X.; Liu, J.; Kang, B.; Li, X.; Zeng, L.; Liu, Y.; Qiu, J.; Qian, Q.; Wei, M.; Chen, Q. Preparation of SnS$_2$/enteromorpha prolifera derived carbon composite and its performance of sodium-ion batteries. *J. Phys. Chem. Solids* **2021**, *152*, 109976. [CrossRef]

216. Wang, L.; Lin, C.; Liang, T.; Wang, N.; Feng, J.; Yan, W. NiSe2 nanoparticles encapsulated in CNTs covered and N-doped TiN/carbon nanofibers as a binder-free anode for advanced sodium-ion batteries. *Mater. Today Chem.* **2022**, *24*, 100849. [CrossRef]

217. Shao, L.; Hong, J.; Wang, S.; Wu, F.; Yang, F.; Shi, X.; Sun, Z. Urchin-like FeS$_2$ hierarchitectures wrapped with N-doped multi-wall carbon nanotubes @ rGO as high-rate anode for sodium ion batteries. *J. Power Source* **2021**, *491*, 229627. [CrossRef]

218. Wang, J.; Wu, N.; Han, L.; Liao, C.; Mu, X.; Kan, Y.; Hu, Y. Polyacrylonitrile @ metal organic frameworks composite-derived heteroatoms doped carbon @ encapsulated cobalt sulfide as superb sodium ion batteries anode. *J. Colloid Interface Sci.* **2021**, *581*, 552–565. [CrossRef]

219. Chen, H.; Tian, P.; Fu, L.; Wan, S.; Liu, Q. Hollow spheres of solid solution Fe$_7$Ni$_3$S$_{11}$/CN as advanced anode materials for sodium ion batteries. *Chem. Eng. J.* **2022**, *430*, 132688. [CrossRef]

220. Zhang, X.; Liu, K.; Zhang, S.; Miao, F.; Xiao, W.; Shen, Y.; Zhang, P.; Wang, Z.; Shao, G. Enabling remarkable cycling performance of high-loading MoS$_2$@Graphene anode for sodium ion batteries with tunable cut-off voltage. *J. Power Source* **2020**, *458*, 228040. [CrossRef]

221. Duan, M.; Meng, Y.; Xiao, M.; Ahmed, W.H.Z.; Wang, X.; Gao, H.; Zhang, Y.; Zhu, F. Facile synthesis of WS$_2$/Ni$_3$S$_2$ encapsulated in N-doped carbon hybrid electrode with high rate performance as anode for sodium-ion batteries. *J. Electroanal. Chem.* **2021**, *899*, 115681. [CrossRef]

222. Park, G.D.; Park, J.; Kim, J.K.; Kang, Y.C. Metal sulfoselenide solid solution embedded in porous hollow carbon nanospheres as effective anode material for potassium-ion batteries with long cycle life and enhanced rate performance. *Chem. Eng. J.* **2022**, *428*, 131051. [CrossRef]

223. Li, J.; Rui, B.; Wei, W.; Nie, P.; Chang, L.; Le, Z. Nanosheets assembled layered MoS$_2$/MXene as high performance anode materials for potassium ion batteries. *J. Power Source* **2020**, *449*, 227481. [CrossRef]

224. Ho Na, J.; Chan Kang, Y.; Park, S.K. Electrospun MOF-based ZnSe nanocrystals confined in N-doped mesoporous carbon fibers as anode materials for potassium ion batteries with long-term cycling stability. *Chem. Eng. J.* **2021**, *425*, 131651. [CrossRef]

225. Liu, Y.; Yang, C.; Li, Y.Y.; Zheng, F.; Li, Y.Y.; Deng, Q.; Zhong, W.; Wang, G.; Liu, T. FeSe2/nitrogen-doped carbon as anode material for Potassium-ion batteries. *Chem. Eng. J.* **2020**, *393*, 124590. [CrossRef]

226. Ma, G.; Li, C.; Liu, F.; Majeed, M.K.; Feng, Z. Metal-organic framework-derived Co$_{0.85}$Se nanoparticles in N-doped carbon as a high-rate and long-lifespan anode material for potassium ion batteries. *Mater. Today Energy* **2018**, *10*, 241–248. [CrossRef]

227. He, Y.; Wang, L.; Dong, C.; Li, C.; Ding, X.; Qian, Y.; Xu, L. In-situ rooting ZnSe/N-doped hollow carbon architectures as high-rate and long-life anode materials for half/full sodium-ion and potassium-ion batteries. *Energy Storage Mater.* **2019**, *23*, 35–45. [CrossRef]

228. Kang, B.; Chen, X.; Zeng, L.; Luo, F.; Li, X.; Xu, L.; Yang, M.Q.; Chen, Q.; Wei, M.; Qian, Q. In situ fabrication of ultrathin few-layered WSe$_2$ anchored on N, P dual-doped carbon by bioreactor for half/full sodium/potassium-ion batteries with ultralong cycling lifespan. *J. Colloid Interface Sci.* **2020**, *574*, 217–228. [CrossRef]

229. Jiang, Q.; Wang, L.; Wang, Y.; Qin, M.; Wu, R.; Huang, Z.; Yang, H.J.; Li, Y.; Zhou, T.; Hu, J. Rational design of MoSe$_2$ nanosheet-coated MOF-derived N-doped porous carbon polyhedron for potassium storage. *J. Colloid Interface Sci.* **2021**, *600*, 430–439. [CrossRef]

230. Lei, Z.; Li, X.; Liu, Y.; Wu, J.; Wang, Y.; Luo, Y.; Chen, Q.; Wei, M.; Zeng, L.; Qian, Q. Two-dimentional MoSe$_2$/chitosan-derived nitrogen-doped carbon composite enabling stable sodium/potassium storage. *J. Phys. Chem. Solids* **2022**, *163*, 110573. [CrossRef]

231. Li, D.; Zhang, J.; Suo, G.; Yu, Q.; Wang, W.; Feng, L.; Hou, X.; Ye, X.; Zhang, L.; Yang, Y. Hollow Co$_{0.85}$Se cubes encapsulated in graphene for enhanced potassium storage. *J. Electroanal. Chem.* **2020**, *864*, 114100. [CrossRef]

232. Suo, G.; Zhang, J.; Li, D.; Yu, Q.; Wang, W.; He, M.; Feng, L.; Hou, X.; Yang, Y.; Ye, X.; et al. N-doped carbon/ultrathin 2D metallic cobalt selenide core/sheath flexible framework bridged by chemical bonds for high-performance potassium storage. *Chem. Eng. J.* **2020**, *388*, 124396. [CrossRef]

233. Xing, W.; Du, D.; Cai, T.; Li, X.; Zhou, J.; Chai, Y.; Xue, Q.; Yan, Z. Carbon-encapsulated CoSe nanoparticles derived from metal-organic frameworks as advanced cathode material for Al-ion battery. *J. Power Source* **2018**, *401*, 6–12. [CrossRef]

234. Li, J.; Liu, W.; Yu, Z.; Deng, J.; Zhong, S.; Xiao, Q.; Chen, F.; Yan, D. N-doped C@ZnSe as a low cost positive electrode for aluminum-ion batteries: Better electrochemical performance with high voltage platform of ~1.8 V and new reaction mechanism. *Electrochim. Acta* **2021**, *370*, 137790. [CrossRef]

235. Yang, W.; Lu, H.; Cao, Y.; Jing, P. Single-/few-layered ultrasmall WS_2 nanoplates embedded in nitrogen-doped carbon nanofibers as a cathode for rechargeable aluminum batteries. *J. Power Source* **2019**, *441*, 227173. [CrossRef]

236. Zhou, Q.; Wang, D.; Lian, Y.; Hou, S.; Ban, C.; Wang, Z.; Zhao, J.; Zhang, H. Rechargeable aluminum-ion battery with sheet-like $MoSe_2$@C nanocomposites cathode. *Electrochim. Acta* **2020**, *354*, 136677. [CrossRef]

237. Zheng, J.; Ju, S.; Yao, L.; Xia, G.; Yu, X. Construction of solid solution sulfide embedded in MXene@N-doped carbon dual protection matrix for advanced aluminum ion batteries. *J. Power Source* **2021**, *511*, 230450. [CrossRef]

238. Xing, L.; Asare, K.; Liu, X.; Meng, J.; Wang, K.; An, Q.; Mai, L. Nano Energy Insights into the storage mechanism of vs. 4 nanowire clusters in aluminum-ion battery. *Nano Energy* **2021**, *79*, 105384. [CrossRef]

239. Zhang, H.; Liu, Y.; Yang, L.; Zhao, L.; Dong, X.; Wang, H.; Li, Y.; Sun, T.; Li, Q.; Li, H. Evidence for dual anions co-insertion in a transition metal chalcogenide cathode material $NiSe_2$ for high-performance rechargeable aluminum-ion batteries. *Energy Storage Mater.* **2022**, *47*, 336–344. [CrossRef]

240. Du, Y.; Zhang, B.; Zhang, W.; Jin, H.; Qin, J.; Wan, J.; Zhang, J.; Chen, G. Interfacial engineering of Bi_2Te_3/Sb_2Te_3 heterojunction enables high–energy cathode for aluminum batteries. *Energy Storage Mater.* **2021**, *38*, 231–240. [CrossRef]

241. Lu, H.; Li, Y.; Zheng, Y.; Dong, C.; Li, Y.; Meng, F.; Wang, Y.; Teng, C.; Wang, X.; Zhou, D.; et al. Layered double hydroxide-derived Fe-doped NiSe cathode toward stable and high-energy aluminum storage. *Mater. Today Energy* **2022**, *24*, 100940. [CrossRef]

242. Gao, Y.; Zhai, Z.; Dong, Y.; Pang, Y.; Chen, J.; Li, G. 1 T-VSe_2 Nanoparticles cooperated with reduced graphene oxide as a superior cathode material for rechargeable Mg-ion batteries. *Appl. Surf. Sci.* **2022**, *592*, 153141. [CrossRef]

243. Tong, Y.; Gao, A.; Zhang, Q.; Gao, T.; Yue, J.; Meng, F.; Gong, Y.; Xi, S.; Lin, Z.; Mao, M.; et al. Cation-synergy stabilizing anion redox of Chevrel phase Mo6S8 in aluminum ion battery. *Energy Storage Mater.* **2021**, *37*, 87–93. [CrossRef]

244. Tang, B.; Tian, N.; Jiang, J.; Li, Y.; Yang, J.; Zhu, Q. Investigation of zinc storage capacity of WS_2 nanosheets for rechargeable aqueous Zn-ion batteries. *J. Alloys Compd.* **2022**, *894*, 162391. [CrossRef]

245. Wang, L.; Jiang, M.; Liu, F.; Huang, Q.; Liu, L.; Fu, L.; Wu, Y. Layered TiS_2 as a Promising Host Material for Aqueous Rechargeable Zn Ion Battery. *Batter. Energy Storage* **2020**, *34*, 11590–11596. [CrossRef]

246. Wang, W.; Yang, Y.; Nuli, Y.; Zhou, J.; Yang, J.; Wang, J. Metal Organic Framework (MOF)-Derived carbon-encapsulated cuprous sulfide cathode based on displacement reaction for Hybrid $Mg_2þ$/Liþ batteries. *J. Power Source* **2020**, *445*, 227325. [CrossRef]

247. de la Parra-Arciniega, S.M.; González-Juárez, E.; Hernández-Carrillo, R.A.; Briones-Martínez, R.; Jiménez-Barrera, R.M.; Garcia-Gómez, N.A.; Sánchez, E.M. A Mg^{2+}/Li^+ hybrid-ion battery based on MoS2 prepared by solvothermal synthesis with ionic liquid assistance. *J. Mater. Sci. Mater. Electron.* **2020**, *31*, 14702–14713. [CrossRef]

248. Wang, Y.; Wang, C.; Yi, X.; Hu, Y.; Wang, L.; Ma, L.; Zhu, G.; Chen, T.; Jin, Z. Hybrid Mg/Li-ion batteries enabled by Mg^{2+}/Li^+ co-intercalation in VS4 nanodendrites. *Energy Storage Mater.* **2019**, *23*, 741–748. [CrossRef]

249. Chen, X.; Wang, S.; Wang, H. High performance hybrid Mg-Li ion batteries with conversion cathodes for low cost energy storage. *Electrochim. Acta* **2018**, *265*, 175–183. [CrossRef]

250. Truong, Q.D.; Kempaiah Devaraju, M.; Nakayasu, Y.; Tamura, N.; Sasaki, Y.; Tomai, T.; Honma, I. Exfoliated MoS_2 and $MoSe_2$ Nanosheets by a Supercritical Fluid Process for a Hybrid Mg-Li-Ion Battery. *ACS Omega* **2017**, *2*, 2360–2367. [CrossRef]

251. Cai, X.; Yu, L.; Dong, J.; Cen, Y.; Zhu, T.; Yu, D.; Chen, C.; Zhang, D.; Liu, Y.; Pan, F. Revealing the electrochemical mechanism of the conversion-type Co_3S_4 in a novel high-capacity Mg-Li hybrid battery. *Electrochim. Acta* **2022**, *401*, 139403. [CrossRef]

252. Jing, P.; Lu, H.; Yang, W.; Cao, Y. Interlayer-expanded and binder-free VS_2 nanosheets assemblies for enhanced Mg^{2+} and Li^+/Mg^{2+} hybrid ion storage. *Electrochim. Acta* **2020**, *330*, 135263. [CrossRef]

253. Bian, X.; Gao, Y.; Fu, Q.; Indris, S.; Ju, Y.; Meng, Y.; Du, F.; Bramnik, N.; Ehrenberg, H.; Wei, Y. A long cycle-life and high safety Na^+/Mg^{2+} hybrid-ion battery built by using a TiS2 derived titanium sulfide cathode. *J. Mater. Chem. A* **2017**, *5*, 600–608. [CrossRef]

254. Shi, C.; Xia, Q.; Xue, X.; Liu, Q.; Liu, H.J. Synthesis of cobalt-based layered coordination polymer nanosheets and their application in lithium-ion batteries as anode materials. *RSC Adv.* **2016**, *6*, 4442–4447. [CrossRef]

255. Fan, Y.; Chen, X.; Legut, D.; Zhang, Q. Modeling and theoretical design of next-generation lithium metal batteries. *Energy Storage Mater.* **2019**, *16*, 169–193. [CrossRef]

256. Xu, M.; Liang, T.; Shi, M.; Chen, H. Graphene-like two-dimensional materials. *Chem. Rev.* **2013**, *113*, 3766–3798. [CrossRef]

257. Chen, L.J. Nanoscale Copper and Copper Compounds for Advanced Device Applications. *Metall. Mater. Trans. A Phys. Metall. Mater. Sci.* **2016**, *47*, 5845–5851. [CrossRef]

258. Chen, Q.; Ren, M.; Xu, H.; Liu, W.; Hei, J.; Su, L.; Wang, L. Cu_2S@ N, S Dual-Doped Carbon Matrix Hybrid as Superior Anode Materials for Lithium/Sodium ion Batteries. *ChemElectroChem* **2018**, *5*, 2135–2141. [CrossRef]

259. Wu, N.; Miao, D.; Zhou, X.; Zhang, L.; Liu, G.; Guo, D. V$_3$S$_4$ Nanosheets Anchored on N, S Co-Doped Graphene with Pseudocapacitive Effect for Fast and Durable Lithium Storage. *Nanomaterials* **2019**, *9*, 1638. [CrossRef]

260. Wang, L.; Ni, Y.; Hou, X.; Chen, L.; Li, F.; Chen, J. A Two-Dimensional Metal–Organic Polymer Enabled by Robust Nickel–Nitrogen and Hydrogen Bonds for Exceptional Sodium-Ion Storage. *Angew. Chem.-Int. Ed.* **2020**, *59*, 22126–22131. [CrossRef]

261. Xiao, Y.; Su, D.; Wang, X.; Wu, S.; Zhou, L.; Shi, Y.; Fang, S.; Cheng, H.M.; Li, F. CuS Microspheres with Tunable Interlayer Space and Micropore as a High-Rate and Long-Life Anode for Sodium-Ion Batteries. *Adv. Energy Mater.* **2018**, *8*, 1800930. [CrossRef]

262. Zhang, Y.; Wang, P.; Yin, Y.; Zhang, X.; Fan, L.; Zhang, N.; Sun, K. Heterostructured SnS-ZnS@C hollow nanoboxes embedded in graphene for high performance lithium and sodium ion batteries. *Chem. Eng. J.* **2019**, *356*, 1042–1051. [CrossRef]

263. Peng, Q.; Hu, X.; Zeng, T.; Shang, B.; Mao, M.; Jiao, X.; Xi, G. FeSb$_2$S$_4$ anchored on amine-modified graphene towards high-performance anode material for sodium ion batteries. *Chem. Eng. J.* **2020**, *385*, 123857. [CrossRef]

264. Chang, X.; Ma, Y.; Yang, M.; Xing, T.; Tang, L.; Chen, T.; Guo, Q.; Zhu, X.; Liu, J.; Xia, H. In-situ solid-state growth of N, S codoped carbon nanotubes encapsulating metal sulfides for high-efficient-stable sodium ion storage. *Energy Storage Mater.* **2019**, *23*, 358–366. [CrossRef]

265. Cui, Y.; Feng, W.; Wang, D.; Wang, Y.; Liu, W.; Wang, H.; Jin, Y.; Yan, Y.; Hu, H.; Wu, M.; et al. Water-Soluble Salt Template-Assisted Anchor of Hollow FeS$_2$ Nanoparticle Inside 3D Carbon Skeleton to Achieve Fast Potassium-Ion Storage. *Adv. Energy Mater.* **2021**, *11*, 2101343. [CrossRef]

266. Liu, Q.; Ye, J.; Chen, Z.; Hao, Q.; Xu, C.; Hou, J. Double conductivity-improved porous Sn/Sn$_4$P$_3$@carbon nanocomposite as high performance anode in Lithium-ion batteries. *J. Colloid Interface Sci.* **2019**, *537*, 588–596. [CrossRef]

267. Fang, G.; Wu, Z.; Zhou, J.; Zhu, C.; Cao, X.; Lin, T.; Chen, Y.; Wang, C.; Pan, A.; Liang, S. Observation of Pseudocapacitive Effect and Fast Ion Diffusion in Bimetallic Sulfides as an Advanced Sodium-Ion Battery Anode. *Adv. Energy Mater.* **2018**, *8*, 1703155. [CrossRef]

268. Liu, Q.; Hou, J.; Hao, Q.; Huang, P.; Xu, C.; Zhou, Q.; Zhou, J.; Liu, H. Nitrogen-doped carbon encapsulated hollow ZnSe/CoSe$_2$ nanospheres as high performance anodes for lithium-ion batteries. *Nanoscale* **2020**, *12*, 22778–22786. [CrossRef]

269. Chen, Y.; Liu, H.; Guo, X.; Zhu, S.; Zhao, Y.; Iikubo, S. Bimetallic Sulfide SnS$_2$/FeS$_2$ Nanosheets as High-Performance Anode Materials for Sodium-Ion Batteries. *ACS Appl. Mater. Interfaces* **2021**, *13*, 39248–39256. [CrossRef]

270. Goin, D.E.; Pearson, R.M.; Craske, M.G.; Stein, A.; Pettifor, A.; Sheri, A.; Kahn, K.; Neilands, T.B.; Hamilton, E.L.; Selin, A.; et al. Cell-like-carbon-micro-spheres for robust potassium anode. *Natl. Sci. Rev.* **2019**, *8*, 94720.

271. Park, G.D.; Kim, J.H.; Park, S.K.; Kang, Y.C. MoSe$_2$ Embedded CNT-Reduced Graphene Oxide Composite Microsphere with Superior Sodium Ion Storage and Electrocatalytic Hydrogen Evolution Performances. *ACS Appl. Mater. Interfaces* **2017**, *9*, 10673–10683. [CrossRef]

272. Yang, S.; Park, G.D.; Kang, Y.C. Conversion reaction mechanism of cobalt telluride-carbon composite microspheres synthesized by spray pyrolysis process for K-ion storage. *Appl. Surf. Sci.* **2020**, *529*, 147140. [CrossRef]

273. Wu, Y.; Nie, P.; Wu, L.; Dou, H.; Zhang, X. 2D MXene/SnS$_2$ composites as high-performance anodes for sodium ion batteries. *Chem. Eng. J.* **2018**, *334*, 932–938. [CrossRef]

274. Yang, Z.; Li, W.; Zhang, G.; Wang, J.; Zuo, J.; Xu, Q.; Shan, H.; He, X.; Lv, M.; Hu, J.; et al. Constructing Sb[sbnd]O[sbnd]C bond to improve the alloying reaction reversibility of free-standing Sb$_2$Se$_3$ nanorods for potassium-ion batteries. *Nano Energy* **2022**, *93*, 106764. [CrossRef]

275. Park, G.D.; Kang, Y.C. Conversion Reaction Mechanism for Yolk-Shell-Structured Iron Telluride-C Nanospheres and Exploration of Their Electrochemical Performance as an Anode Material for Potassium-Ion Batteries. *Small Methods* **2020**, *4*, 200055. [CrossRef]

276. Yang, R.; Yao, W.; Tang, B.; Zhang, F.; Lei, X.; Lee, C.; Tang, Y. Development and challenges of electrode materials for rechargeable Mg batteries. *Energy Storage Mater.* **2021**, *42*, 687–704. [CrossRef]

277. Zhang, Y.; Geng, H.; Wei, W.; Ma, J.; Chen, L.; Li, C.C. Challenges and recent progress in the design of advanced electrode materials for rechargeable Mg batteries. *Energy Storage Mater.* **2019**, *20*, 118–138. [CrossRef]

278. Michail, A.; Silván, B.; Tapia-Ruiz, N. Progress in high-voltage MgMn$_2$O$_4$ oxyspinel cathode materials for Mg batteries. *Curr. Opin. Electrochem.* **2022**, *31*, 100817. [CrossRef]

279. Luo, J.; He, S.; Liu, T.L. Tertiary Mg/MgCl$_2$/AlCl$_3$ Inorganic Mg^{2+} Electrolytes with Unprecedented Electrochemical Performance for Reversible Mg Deposition. *ACS Energy Lett.* **2017**, *2*, 1197–1202. [CrossRef]

280. Deivanayagam, R.; Ingram, B.J.; Shahbazian-Yassar, R. Progress in development of electrolytes for magnesium batteries. *Energy Storage Mater.* **2019**, *21*, 136–153. [CrossRef]

281. Li, Z.; Han, L.; Wang, Y.; Li, X.; Lu, J.; Hu, X. Microstructure Characteristics of Cathode Materials for Rechargeable Magnesium Batteries. *Small* **2019**, *15*, 1900105. [CrossRef]

282. Yang, J.; Wang, J.; Dong, X.; Zhu, L.; Hou, D.; Zeng, W.; Wang, J. The potential application of VS$_2$ as an electrode material for Mg ion battery: A DFT study. *Appl. Surf. Sci.* **2021**, *544*, 148775. [CrossRef]

283. Wang, Z.; Li, W.; Zheng, Y.; Yang, Z.; Zhang, J. How does the active site in the MoSe$_2$ surface affect its electrochemical performance as anode material for metal-ion batteries? *Appl. Surf. Sci.* **2020**, *526*, 146637. [CrossRef]

284. Zhao, Y.; Wang, D.; Yang, D.; Wei, L.; Liu, B.; Wang, X.; Chen, G.; Wei, Y. Superior Mg^{2+} storage properties of VS2 nanosheets by using an APC-PP14Cl/THF electrolyte. *Energy Storage Mater.* **2019**, *23*, 749–756. [CrossRef]

285. Faegh, E.; Ng, B.; Hayman, D.; Mustain, W.E. Practical assessment of the performance of aluminium battery technologies. *Nat. Energy* **2021**, *6*, 450. [CrossRef]

286. Yao, L.; Ju, S.; Xu, T.; Yu, X. Spatial Isolation-Inspired Ultrafine $CoSe_2$ for High-Energy Aluminum Batteries with Improved Rate Cyclability. *ACS Nano* **2021**, *15*, 13662–13673. [CrossRef] [PubMed]

287. Xu, W.; Sun, C.; Zhao, K.; Cheng, X.; Rawal, S.; Xu, Y.; Wang, Y. Defect engineering activating (Boosting) zinc storage capacity of MoS_2. *Energy Storage Mater.* **2019**, *16*, 527–534. [CrossRef]

288. Wu, T.H.; Zhang, Y.; Althouse, Z.D.; Liu, N. Nanoscale design of zinc anodes for high-energy aqueous rechargeable batteries. *Mater. Today Nano* **2019**, *6*, 100032. [CrossRef]

289. Xiong, F.; Fan, Y.; Tan, S.; Zhou, L.; Xu, Y.; Pei, C.; An, Q.; Mai, L. Magnesium storage performance and mechanism of CuS cathode. *Nano Energy* **2018**, *47*, 210–216. [CrossRef]

290. Zhang, Y.; Li, Y.; Wang, Y.; Guo, R.; Liu, W.; Pei, H.; Yin, G.; Ye, D.; Yu, S.; Xie, J. A flexible copper sulfide @ multi-walled carbon nanotubes cathode for advanced magnesium-lithium-ion batteries. *J. Colloid Interface Sci.* **2019**, *553*, 239–246. [CrossRef]

291. Yuan, H.; Wang, N.; NuLi, Y.; Yang, J.; Wang, J. Hybrid Mg^{2+}/Li^+ batteries with Cu_2Se cathode based on displacement reaction. *Electrochim. Acta* **2018**, *261*, 503–512. [CrossRef]

292. Raguzin, I.; Choudhury, S.; Simon, F.; Stamm, M.; Ionov, L. Effect of Current Collector on Performance of Li-S Batteries. *Adv. Mater. Interfaces* **2017**, *4*, 1600811. [CrossRef]

293. Chen, L.; Guo, X.; Lu, W.; Chen, M.; Li, Q.; Xue, H.; Pang, H. Manganese monoxide-based materials for advanced batteries. *Coord. Chem. Rev.* **2018**, *368*, 13–34. [CrossRef]

294. Li, F.; Liu, Q.; Hu, J.; Feng, Y.; He, P.; Ma, J. Recent advances in cathode materials for rechargeable lithium-sulfur batteries. *Nanoscale* **2019**, *11*, 15418–15439. [CrossRef] [PubMed]

295. He, J.; Manthiram, A. A review on the status and challenges of electrocatalysts in lithium-sulfur batteries. *Energy Storage Mater.* **2019**, *20*, 55–70. [CrossRef]

296. Li, P.; Ma, L.; Wu, T.; Ye, H.; Zhou, J.; Zhao, F.; Han, N.; Wang, Y.; Wu, Y.; Li, Y.; et al. Chemical Immobilization and Conversion of Active Polysulfides Directly by Copper Current Collector: A New Approach to Enabling Stable Room-Temperature Li-S and Na-S Batteries. *Adv. Energy Mater.* **2018**, *8*, 1800624. [CrossRef]

297. Guo, Q.; Zheng, Z. Rational Design of Binders for Stable Li-S and Na-S Batteries. *Adv. Funct. Mater.* **2020**, *30*, 1907931. [CrossRef]

298. Deng, X.; Li, J.; Ma, L.; Sha, J.; Zhao, N. Three-dimensional porous carbon materials and their composites as electrodes for electrochemical energy storage systems. *Mater. Chem. Front.* **2019**, *3*, 2221–2245. [CrossRef]

299. Chen, P.; Wu, Z.; Guo, T.; Zhou, Y.; Liu, M.; Xia, X.; Sun, J.; Lu, L.; Ouyang, X.; Wang, X.; et al. Strong Chemical Interaction between Lithium Polysulfides and Flame-Retardant Polyphosphazene for Lithium–Sulfur Batteries with Enhanced Safety and Electrochemical Performance. *Adv. Mater.* **2021**, *33*, 2007549. [CrossRef]

300. Jin, X.; Gao, S.; Wu, A.; Zhao, J.; Huang, H.; Cao, G. Dual-Constrained Sulfur in $FeS_2@C$ Nanostructured Lithium-Sulfide Batteries. *ACS Appl. Energy Mater.* **2020**, *3*, 10950–10960. [CrossRef]

301. Xu, W.; Wu, Q.; Che, Z.; Fan, B.; Zhao, D.; Wang, S.; Han, A.; Li, L. A Novel Synthesizing Strategy of 3D Cose2 Porous Hollow Flowers for High Performance Lithium–Sulfur Batteries. *Catalysts* **2021**, *11*, 273. [CrossRef]

302. Steudel, R.; Chivers, T. The role of polysulfide dianions and radical anions in the chemical, physical and biological sciences, including sulfur-based batteries. *Chem. Soc. Rev.* **2019**, *48*, 3279–3319. [CrossRef] [PubMed]

303. Chen, L.; Yang, W.; Li, X.; Han, L.; Wei, M. Co_9S_8 embedded into N/S doped carbon composites: In situ derivation from a sulfonate-based metal-organic framework and its electrochemical properties. *J. Mater. Chem. A* **2019**, *7*, 10331–10337. [CrossRef]

304. Ye, C.; Jiao, Y.; Chao, D.; Ling, T.; Shan, J.; Zhang, B.; Gu, Q.; Davey, K.; Wang, H.; Qiao, S.Z. Electron-State Confinement of Polysulfides for Highly Stable Sodium–Sulfur Batteries. *Adv. Mater.* **2020**, *32*, 1907557. [CrossRef] [PubMed]

305. Wu, J.; Tang, A.; Huang, S.; Li, J.; Zeng, L.; Wei, M. In Situ Confined Co5Ge3Alloy Nanoparticles in Nitrogen-Doped Carbon Nanotubes for Boosting Lithium Storage. *ACS Appl. Mater. Interfaces* **2020**, *12*, 46247–46253. [CrossRef] [PubMed]

306. Wang, N.; Wang, Y.; Bai, Z.; Fang, Z.; Zhang, X.; Xu, Z.; Ding, Y.; Xu, X.; Du, Y.; Dou, S.; et al. High-performance room-temperature sodium-sulfur battery enabled by electrocatalytic sodium polysulfides full conversion. *Energy Environ. Sci.* **2020**, *13*, 562–570. [CrossRef]

307. Yan, Z.; Xiao, J.; Lai, W.; Wang, L.; Gebert, F.; Wang, Y.; Gu, Q.; Liu, H.; Chou, S.L.; Liu, H.; et al. Nickel sulfide nanocrystals on nitrogen-doped porous carbon nanotubes with high-efficiency electrocatalysis for room-temperature sodium-sulfur batteries. *Nat. Commun.* **2019**, *10*, 4793. [CrossRef]

308. Zhang, B.W.; Sheng, T.; Wang, Y.X.; Chou, S.; Davey, K.; Dou, S.X.; Qiao, S.Z. Long-Life Room-Temperature Sodium–Sulfur Batteries by Virtue of Transition-Metal-Nanocluster–Sulfur Interactions. *Angew. Chem.-Int. Ed.* **2019**, *58*, 1484–1488. [CrossRef]

309. Xiao, F.; Wang, H.; Yao, T.; Zhao, X.; Yang, X.; Yu, D.Y.W.; Rogach, A.L. MOF-Derived CoS_2/N-Doped Carbon Composite to Induce Short-Chain Sulfur Molecule Generation for Enhanced Sodium−Sulfur Battery Performance. *ACS Appl. Mater. Interfaces* **2021**, *13*, 18010–18020. [CrossRef]

310. Wu, D.; Ren, W.; Nuli, Y.; Yang, J.; Wang, J. Recent progress on selenium-based cathode materials for rechargeable magnesium batteries: A mini review. *J. Mater. Sci. Technol.* **2021**, *91*, 168–177. [CrossRef]

311. Yoo, H.D.; Shterenberg, I.; Gofer, Y.; Gershinsky, G.; Pour, N.; Aurbach, D. Mg rechargeable batteries: An on-going challenge. *Energy Environ. Sci.* **2013**, *6*, 2265–2279. [CrossRef]

312. Gao, T.; Noked, M.; Pearse, A.J.; Gillette, E.; Fan, X.; Zhu, Y.; Luo, C.; Suo, L.; Schroeder, M.A.; Xu, K.; et al. Enhancing the Reversibility of Mg/S Battery Chemistry through Li+ Mediation. *J. Am. Chem. Soc.* **2015**, *137*, 12388–12393. [CrossRef] [PubMed]

313. Sun, X.; Bonnick, P.; Nazar, L.F. Layered TiS_2 Positive Electrode for Mg Batteries. *ACS Energy Lett.* **2016**, *1*, 297–301. [CrossRef]

314. Zhao, Q.; Wang, R.; Zhang, Y.; Huang, G.; Jiang, B.; Xu, C.; Pan, F. The design of Co$_3$S$_4$@MXene heterostructure as sulfur host to promote the electrochemical kinetics for reversible magnesium-sulfur batteries. *J. Magnes. Alloys* **2021**, *9*, 78–89. [CrossRef]

315. Yoon, K.R.; Lee, G.Y.; Jung, J.W.; Kim, N.H.; Kim, S.O.; Kim, I.D. One-Dimensional RuO$_2$/Mn$_2$O$_3$ Hollow Architectures as Efficient Bifunctional Catalysts for Lithium-Oxygen Batteries. *Nano Lett.* **2016**, *16*, 2076–2083. [CrossRef] [PubMed]

316. Hu, A.; Long, J.; Shu, C.; Liang, R.; Li, J. Three-Dimensional Interconnected Network Architecture with Homogeneously Dispersed Carbon Nanotubes and Layered MoS$_2$ as a Highly Efficient Cathode Catalyst for Lithium-Oxygen Battery. *ACS Appl. Mater. Interfaces* **2018**, *10*, 34077–34086. [CrossRef]

317. Gao, J.; Cai, X.; Wang, J.; Hou, M.; Lai, L.; Zhang, L. Recent progress in hierarchically structured O$_2$-cathodes for Li-O$_2$ batteries. *Chem. Eng. J.* **2018**, *352*, 972–995. [CrossRef]

318. Liu, B.; Sun, Y.; Liu, L.; Xu, S.; Yan, X. Advances in Manganese-Based Oxides Cathodic Electrocatalysts for Li–Air Batteries. *Adv. Funct. Mater.* **2018**, *28*, 1704973. [CrossRef]

319. Jung, J.W.; Jang, J.S.; Yun, T.G.; Yoon, K.R.; Kim, I.D. Three-Dimensional Nanofibrous Air Electrode Assembled with Carbon Nanotubes-Bridged Hollow Fe$_2$O$_3$ Nanoparticles for High-Performance Lithium-Oxygen Batteries. *ACS Appl. Mater. Interfaces* **2018**, *10*, 6531–6540. [CrossRef]

320. Huang, Z.; Qin, X.; Gu, X.; Li, G.; Mu, Y.; Wang, N.; Ithisuphalap, K.; Wang, H.; Guo, Z.; Shi, Z.; et al. Mn$_3$O$_4$ Quantum Dots Supported on Nitrogen-Doped Partially Exfoliated Multiwall Carbon Nanotubes as Oxygen Reduction Electrocatalysts for High-Performance Zn-Air Batteries. *ACS Appl. Mater. Interfaces* **2018**, *10*, 23900–23909. [CrossRef]

321. Cai, P.; Huang, J.; Chen, J.; Wen, Z. Oxygen-Containing Amorphous Cobalt Sulfide Porous Nanocubes as High-Activity Electrocatalysts for the Oxygen Evolution Reaction in an Alkaline/Neutral Medium. *Angew. Chem.-Int. Ed.* **2017**, *56*, 4858–4861. [CrossRef]

322. Zhu, Q.C.; Xu, S.M.; Harris, M.M.; Ma, C.; Liu, Y.S.; Wei, X.; Xu, H.S.; Zhou, Y.X.; Cao, Y.C.; Wang, K.X.; et al. A Composite of Carbon-Wrapped Mo$_2$C Nanoparticle and Carbon Nanotube Formed Directly on Ni Foam as a High-Performance Binder-Free Cathode for Li-O2 Batteries. *Adv. Funct. Mater.* **2016**, *26*, 8514–8520. [CrossRef]

323. Guo, Z.; Wang, F.; Li, Z.; Yang, Y.; Tamirat, A.G.; Qi, H.; Han, J.; Li, W.; Wang, L.; Feng, S. Lithiophilic Co/Co$_4$N nanoparticles embedded in hollow N-doped carbon nanocubes stabilizing lithium metal anodes for Li-air batteries. *J. Mater. Chem. A* **2018**, *6*, 22096–22105. [CrossRef]

324. Dai, L.; Sun, Q.; Guo, J.; Cheng, J.; Xu, X.; Guo, H.; Li, D.; Chen, L.; Si, P.; Lou, J.; et al. Mesoporous Mn$_2$O$_3$ rods as a highly efficient catalyst for Li-O2 battery. *J. Power Source* **2019**, *435*, 226833. [CrossRef]

325. Lin, X.; Zhang, T.; Chu, C.; Li, Z.; Liu, R.; Li, P.; Li, Y.; Huang, Z. Synthesis of ZIF-Derived CoS2 Nanocages Interconnected by CNTs for Rechargeable Li−O$_2$ Batteries. *ACS Sustain. Chem. Eng.* **2020**, *8*, 7581–7587. [CrossRef]

326. Li, M.; Shu, C.; Hu, A.; Li, J.; Liang, R.; Long, J. Invigorating the Catalytic Activity of Cobalt Selenide via Structural Phase Transition Engineering for Lithium−Oxygen Batteries. *ACS Sustain. Chem. Eng.* **2020**, *8*, 5018–5027. [CrossRef]

327. Li, Y.; Fu, J.; Zhong, C.; Wu, T.; Chen, Z.; Hu, W.; Amine, K.; Lu, J. Recent Advances in Flexible Zinc-Based Rechargeable Batteries. *Adv. Energy Mater.* **2019**, *9*, 1802605. [CrossRef]

328. Li, H.; Ma, L.; Han, C.; Wang, Z.; Liu, Z.; Tang, Z.; Zhi, C. Advanced rechargeable zinc-based batteries: Recent progress and future perspectives. *Nano Energy* **2019**, *62*, 550–587. [CrossRef]

329. Li, Y.; Wang, C.; Cui, M.; Xiong, J.; Mi, L.; Chen, S. Heterostructured MoO$_2$@MoS$_2$@Co$_9$S$_8$ nanorods as high efficiency bifunctional electrocatalyst for overall water splitting. *Appl. Surf. Sci.* **2021**, *543*, 148804. [CrossRef]

330. Song, J.; Qiu, S.; Hu, F.; Ding, Y.; Han, S.; Li, L.; Chen, H.Y.; Han, X.; Sun, C.; Peng, S. Sub-2 nm Thiophosphate Nanosheets with Heteroatom Doping for Enhanced Oxygen Electrocatalysis. *Adv. Funct. Mater.* **2021**, *31*, 2100618. [CrossRef]

331. Kaneti, Y.V.; Guo, Y.; Septiani, N.L.W.; Iqbal, M.; Jiang, X.; Takei, T.; Yuliarto, B.; Alothman, Z.A.; Golberg, D.; Yamauchi, Y. Self-templated fabrication of hierarchical hollow manganese-cobalt phosphide yolk-shell spheres for enhanced oxygen evolution reaction. *Chem. Eng. J.* **2021**, *405*, 126580. [CrossRef]

332. Xu, W.; Zhu, S.; Liang, Y.; Cui, Z.; Yang, X.; Inoue, A.; Wang, H. A highly efficient electrocatalyst based on amorphous Pd-Cu-S material for hydrogen evolution reaction. *J. Mater. Chem. A* **2017**, *5*, 18793–18800. [CrossRef]

333. Zhang, Y.; Fu, J.; Zhao, H.; Jiang, R.; Tian, F.; Zhang, R. Tremella-like Ni3S2/MnS with ultrathin nanosheets and abundant oxygen vacancies directly used for high speed overall water splitting. *Appl. Catal. B Environ.* **2019**, *257*, 117899. [CrossRef]

334. Wang, J.Y.; Liu, W.T.; Li, X.P.; Ouyang, T.; Liu, Z.Q. Strong hydrophilicity NiS$_2$/Fe$_7$S$_8$ heterojunctions encapsulated in N-doped carbon nanotubes for enhanced oxygen evolution reaction. *Chem. Commun.* **2020**, *56*, 1489–1492. [CrossRef] [PubMed]

335. Liu, X.; Yin, Z.; Cui, M.; Gao, L.; Liu, A.; Su, W.N.; Chen, S.; Ma, T.; Li, Y. Double shelled hollow CoS$_2$@MoS$_2$@NiS$_2$ polyhedron as advanced trifunctional electrocatalyst for zinc-air battery and self-powered overall water splitting. *J. Colloid Interface Sci.* **2022**, *610*, 653–662. [CrossRef] [PubMed]

336. Chen, L.; Wang, Z.; He, X.; Zhang, W.; Asefa, T. Co$_8$FeS$_8$/N,S-Doped Carbons Derived from Fe-Co/S-Bridged Polyphthalocyanine: Efficient Dual-Function Air-Electrode Catalysts for Rechargeable Zn-Air Batteries. *ACS Sustain. Chem. Eng.* **2020**, *8*, 13147–13158. [CrossRef]

337. Wang, K.; Wang, Z.; Liu, Y.; Liu, J.; Cui, Z.; Zhang, X.; Ciucci, F.; Tang, Z. Tailoring the interfacial active center of MnSxO$_{2-x}$/MnCo$_2$S$_4$ heterostructure to boost the performance for oxygen evolution reaction and Zn-Air batteries in neutral electrolyte. *Chem. Eng. J.* **2022**, *427*, 131966. [CrossRef]

338. Li, J.; Wan, T.; Li, J.; Zhang, Z.; Wang, Y.; Liu, G. Three-dimensionally ordered mesoporous trimetal sulfide as efficient electrocatalyst for rechargeable zinc-air batteries. *Appl. Surf. Sci.* **2022**, *575*, 151728. [CrossRef]

339. Cao, L.; Tao, P.; Li, M.; Lyu, F.; Wang, Z.; Wu, S.; Wang, W.; Huo, Y.; Huang, L.; Lu, Z. Synergistic Effects of C/α-MoC and Ag for Efficient Oxygen Reduction Reaction. *J. Phys. Chem. Lett.* **2018**, *9*, 779–784. [CrossRef]

340. Lee, D.U.; Xu, P.; Cano, Z.P.; Kashkooli, A.G.; Park, M.G.; Chen, Z. Recent progress and perspectives on bi-functional oxygen electrocatalysts for advanced rechargeable metal-air batteries. *J. Mater. Chem. A* **2016**, *4*, 7107–7134. [CrossRef]

341. Cao, Y.; Lu, H.; Xu, B.; Yang, W.; Hong, Q. Nitrogen/sulfur dual-doped porous carbon nanofibers with Co_9S_8 nanoparticles encapsulated by graphitic shells: A highly active stable free- standing air electrode for rechargeable non-aqueous $Li-O_2$ batteries and primary alkaline Al-air batteries. *Chem. Eng. J.* **2019**, *378*, 122247. [CrossRef]

342. Lee, Y.; Kim, B.; Hong, J.; Choi, H.; Jang, H.; Hou, B.; Pak, S.; Lee, J.; Lee, S.; Morris, S.M.; et al. Hierarchically assembled tubular shell-core-shell heterostructure of hybrid transition metal chalcogenides for high-performance supercapacitors with ultrahigh cyclability. *Nano Energy* **2017**, *37*, 15–23. [CrossRef]

343. Nagaraju, G.; Sekhar, S.C.; Ramulu, B.; Yu, J.S. High-performance hybrid supercapacitors based on MOF-derived hollow ternary chalcogenides. *Energy Storage Mater.* **2021**, *35*, 750–760. [CrossRef]

344. Kumbhar, V.S.; Lokhande, A.C.; Gaikwad, N.S.; Lokhande, C.D. One-step chemical synthesis of samarium telluride thin films and their supercapacitive properties. *Chem. Phys. Lett.* **2016**, *645*, 112–117. [CrossRef]

345. Liu, M.; Wang, Z.; Liu, J.; Wei, G.; Du, J.; Li, Y.; An, C.; Zhang, J. Synthesis of Few-layer 1T'-$MoTe_2$ Ultrathin Nanosheets for High-performance Pseudocapacitor. *J. Mater. Chem. A* **2017**, *5*, 1035–1042. [CrossRef]

346. Xiao, M.; Su, Y.; Zhao, M.; Du, B. Synthesis of CoTe nanowires: A new electrode material for supercapacitor with high-stability and high-performance. *Nanotechnology* **2019**, *31*, 055706. [CrossRef]

347. Bhat, K.S.; Shenoy, S.; Nagaraja, H.S.; Sridharan, K. Porous cobalt chalcogenide nanostructures as high performance pseudo-capacitor electrodes. *Electrochim. Acta* **2017**, *248*, 188–196. [CrossRef]

348. Shivasharma, T.K.; Bommineedi, L.K.; Sankapal, B.R. Pseudocapacitive nanostructured silver selenide thin film through room temperature chemical route: First approach towards supercapacitive application. *Inorg. Chem. Commun.* **2022**, *135*, 109083. [CrossRef]

349. Hou, L.; Shi, Y.; Wu, C.; Zhang, Y.; Ma, Y.; Sun, X.; Sun, J.; Zhang, X.; Yuan, C. Monodisperse Metallic $NiCoSe_2$ Hollow Sub-Microspheres: Formation Process, Intrinsic Charge-Storage Mechanism, and Appealing Pseudocapacitance as Highly Conductive Electrode for Electrochemical Supercapacitors. *Adv. Funct. Mater.* **2018**, *28*, 1705921. [CrossRef]

350. Banerjee, A.; Bhatnagar, S.; Upadhyay, K.K.; Yadav, P.; Ogale, S. Hollow Co0.85Se nanowire array on carbon fiber paper for high rate pseudocapacitor. *ACS Appl. Mater. Interfaces* **2014**, *6*, 18844–18852. [CrossRef]

351. Song, Y.; Li, H.; Yang, L.; Bai, D.; Zhang, F.; Xu, S. Solid-Solution Sulfides Derived from Tunable Layered Double Hydroxide Precursors/Graphene Aerogel for Pseudocapacitors and Sodium-Ion Batteries. *ACS Appl. Mater. Interfaces* **2017**, *9*, 42742–42750. [CrossRef]

352. Shaikh, S.; Rabinal, M.K. Facile one-step growth of nickel sulfide nano-architecture as binder less electrodes for efficient supercapacitor applications. *Mater. Sci. Semicond. Process.* **2022**, *142*, 106524. [CrossRef]

353. Hong, W.; Wang, J.; Li, Z.; Yang, S. Fabrication of Co_3O_4@Co-Ni sulfides core/shell nanowire arrays as binder-free electrode for electrochemical energy storage. *Energy* **2015**, *93*, 435–441. [CrossRef]

354. Li, S.; He, W.; Liu, B.; Cui, J.; Wang, X.; Peng, D.; Liu, B.; Qu, B. One-step construction of three-dimensional nickel sulfide-embedded carbon matrix for sodium-ion batteries and hybrid capacitors. *Energy Storage Mater.* **2020**, *25*, 636–643. [CrossRef]

355. Edison, T.N.J.I.; Atchudan, R.; Karthik, N.; Ganesh, K.; Xiong, D.; Lee, Y.R. A novel binder-free electro-synthesis of hierarchical nickel sulfide nanostructures on nickel foam as a battery-type electrode for hybrid-capacitors. *Fuel* **2020**, *276*, 118077. [CrossRef]

356. Kaliaraj, G.S.; Ramadoss, A. Nickel-zinc sulfide nanocomposite thin film as an efficient cathode material for high-performance hybrid supercapacitors. *Mater. Sci. Semicond. Process.* **2020**, *105*, 104709. [CrossRef]

357. Meyer, E.; Bede, A.; Mutukwa, D.; Taziwa, R.; Zingwe, N. Optimization, and analysis of carbon supported VS_2 nanocomposites as potential electrodes in supercapacitors. *J. Energy Storage* **2020**, *27*, 101074. [CrossRef]

358. Fayed, M.G.; Attia, S.Y.; Barakat, Y.F.; El-shereafy, E.E.; Rashad, M.M.; Mohamed, S.G. Carbon and nitrogen co-doped MoS_2 nanoflakes as an electrode material for lithium-ion batteries and supercapacitors. *Sustain. Mater. Technol.* **2021**, *29*, e00306. [CrossRef]

359. Liu, B.; Ma, Y.; Wang, J.; Kang, X.; He, L.; Lei, L.; Ran, F. Fabrication of nickel cobalt bimetallic sulfide doped graphite carbon nanohybrids as electrode materials for supercapacitors. *Diam. Relat. Mater.* **2022**, *124*, 108955. [CrossRef]

360. Chen, W.; Xia, C.; Alshareef, H.N. One-step electrodeposited nickel cobalt sulfide nanosheet arrays for high-performance asymmetric supercapacitors. *ACS Nano* **2014**, *8*, 9531–9541. [CrossRef]

361. Chebrolu, V.T.; Balakrishnan, B.; Chinnadurai, D.; Kim, H.J. Selective Growth of Zn–Co–Se Nanostructures on Various Conductive Substrates for Asymmetric Flexible Hybrid Supercapacitor with Enhanced Performance. *Adv. Mater. Technol.* **2020**, *5*, 1900873. [CrossRef]

362. Li, S.; Wang, S.; Wang, J. Optimal surface/diffusion-controlled kinetics of bimetallic selenide nanotubes for hybrid supercapacitors. *J. Colloid Interface Sci.* **2022**, *617*, 304–314. [CrossRef] [PubMed]

363. Yu, D.; Li, Z.; Zhao, G.; Zhang, H.; Aslan, H.; Li, J.; Sun, F.; Zhu, L.; Du, B.; Yang, B.; et al. Porous Ultrathin NiSe Nanosheet Networks on Nickel Foam for High-Performance Hybrid Supercapacitors. *ChemSusChem* **2020**, *13*, 260–266. [CrossRef]

364. Qu, Z.; Li, J.; Guo, M.; Zhao, L.; Duan, L.; Ding, S. Design tremella-like Ni-Co selenide with wonderful electrochemical performances as supercapacitor cathode material. *Electrochim. Acta* **2021**, *393*, 139049. [CrossRef]

365. Bhol, P.; Swain, S.; Jena, S.; Bhatte, K.; Rout, C.S.; Saxena, M.; Jadhav, A.H.; Samal, A.K. Co-Decorated Tellurium Nanotubes for Energy Storage Applications. *ACS Appl. Nano Mater.* **2021**, *9*, 9008–9021. [CrossRef]

366. Manikandan, M.; Subramani, K.; Dhanuskodi, S.; Sathish, M. One-Pot Hydrothermal Synthesis of Nickel Cobalt Telluride Nanorods for Hybrid Energy Storage Systems. *ACS Energy Fuels* **2021**, *35*, 12527–12537. [CrossRef]

367. Li, Y.; Gong, J.; Xing, X.; Du, J.; Xu, P.; Cheng, K.; Ye, K.; Zhu, K.; Yan, J.; Cao, D.; et al. High-performance all-solid-state supercapacitor with binder-free binary transition metal sulfide array as cathode. *Int. J. Energy Res.* **2021**, *45*, 5517–5526. [CrossRef]

368. Mu, C.; Sun, X.; Chang, Y.; Wen, F.; Nie, A.; Wang, B.; Xiang, J.; Zhai, K.; Xue, T.; Liu, Z. High-performance flexible all-solid-state micro-supercapacitors based on two-dimensional InSe nanosheets. *J. Power Source* **2021**, *482*, 228987. [CrossRef]

369. Hu, X.; Shao, W.; Hang, X.; Xiaodong, Z.; Zhu, W.; Xie, Y. Superior Electrical Conductivity in Hydrogenated Layered Ternary Chalcogenide Nanosheets for Flexible All-Solid-State Supercapacitors. *Angew. Chem.* **2016**, *128*, 5827–5832. [CrossRef]

370. Yan, S.X.; Luo, S.H.; Wang, Q.; Zhang, Y.H.; Liu, X. Rational design of hierarchically sulfide and MXene-reinforced porous carbon nanofibers as advanced electrode for high energy density flexible supercapacitors. *Compos. Part B Eng.* **2021**, *224*, 109246. [CrossRef]

371. Harish, K.; Balamurugan, J.; Nguyen, T.T.; Kim, N.H.; Lee, J.H. Advanced interfacial engineering of oxygen-enriched $FexSn_{1−x}OSe$ nanostructures for efficient overall water splitting and flexible zinc-air batteries. *Appl. Catal. B Environ.* **2022**, *305*, 120924. [CrossRef]

372. Wang, J.; Zheng, X.; Cao, Y.; Li, L.; Zhong, C.; Deng, Y.; Han, X.; Hu, W. Developing Indium-based Ternary Spinel Selenides for Efficient Solid Flexible Zn-Air Batteries and Water Splitting. *ACS Appl. Mater. Interfaces* **2020**, *12*, 8115–8123. [CrossRef] [PubMed]

373. Yan, S.; Luo, C.; Zhang, H.; Yang, L.; Huang, N.; Zhang, M.; Yu, H.; Sun, P.; Wang, L.; Lv, X.; et al. In-Situ derived $Co_{1-x}S$@nitrogen-doped carbon nanoneedle array as a bifunctional electrocatalyst for flexible Zinc-air battery. *J. Electroanal. Chem.* **2021**, *900*, 115711. [CrossRef]

374. Feng, T.; Zhao, T.; Zhu, S.; Zhang, N.; Wei, Z.; Wang, K.; Li, L.; Wu, F.; Chen, R. Anion-Doped Cobalt Selenide with Porous Architecture for High-Rate and Flexible Lithium-Sulfur Batteries. *Small Methods* **2021**, *5*, 2100649. [CrossRef] [PubMed]

375. Yin, M.; Miao, H.; Chen, B.; Hu, R.; Xia, L.; Zhang, C.; Wang, F.; Zhang, H.; Yuan, J. Self-supported metal sulfide electrode for flexible quasi-solid-state zinc-air batteries. *J. Alloys Compd.* **2021**, *878*, 160434. [CrossRef]

376. Xie, M.; Zhou, Y.; Wang, Z.; Wang, H.; Yan, D.; Han, B.; Zhang, S.; Deng, C. Heterostructured hollow fibers stitched together from nickel sulfides capped S,N-codoped carbon nanotubes as a trifunctional electrode for flexible hybrid Zn batteries. *Chem. Eng. J.* **2022**, *431*, 133920. [CrossRef]